Bridging the Gap Between Global and Full Fluid Models

A Rapid Semi-Analytical Model for Spatially Resolved Descriptions of Electronegative Plasmas

Richard Andrew Douglas Hurlbatt

Doctor of Philosophy

University of York
Physics

February 2016

Abstract

Scientific investigation of plasma phenomena can be undertaken through either experiments, or numerical and analytical modelling, for which there are a number of well-established options. Global models are quick to implement and have low computation cost, but approximate bulk values. Fluid models can take days to solve, but provide spatial profiles.

This work details a different type of model, analytically similar to fluid models, but computationally closer to a global model, and able to give spatially resolved solutions for the challenging environment of electronegative plasmas. Equations are derived to describe the time averaged spatial profiles of densities, fluxes, and temperatures. Through extended analytical work and normalisations, the resulting differential equations can be solved with an initial value type integration scheme. This is found to be hundreds of times faster than boundary value type methods.

Results and trends are analysed for a symmetrical capacitively coupled oxygen plasma, and relationships between properties are found to conform to the existing knowledge. The behaviour of the system is found to change depending on whether or not the self-interaction of charged species is significant compared to the interaction with the neutrals.

Results from the semi-analytical model agree well with a significantly more detailed and computationally intensive fluid model. In addition to the bulk spatial profiles agreeing both qualitatively and quantitatively, the values of other measured plasma properties agree over a range of system pressures and powers. This comparison is demonstrated to be favourable when contrasted with the results of a global model.

The dynamics of the neutral gas are found to be an important consideration for plasma densities greater than around one part per million. In this model the frictional forces from fast moving ions and thermal energy transfer from hot electrons are the leading cause of disturbance to the neutral properties.

Contents

List of Figures

List of Tables

Acknowledgements

My first thanks go to my supervisors, Timo Gans and Deborah O'Connell, for providing me with the opportunity to work as their student. The guidance and support they have given has been invaluable throughout the whole experience, not just in an academic capacity, but also in my development as a researcher and a member of the plasma physics community. It would have been exceptionally difficult to complete this project without their supervision and discussions.

I would also like to thank my colleagues here at York for many useful conversations over coffee or similar, in particular Kari Niemi, Arthur Greb, and Andrew Gibson. In the same vein I also give thanks to the researchers of Ecole Polytechnique, notably but not exclusively Trevor Lafleur, for discussions and inspiration about this project and other aspects of plasma physics.

My time at York would have been considerably less entertaining if not for the companionship of all of my fellow PhD students and the PDRAs here. My thanks go in particular to Andy West and Martin Blake for always being able to put a smile on my face, even when I was in the depths of Writing Up.

Even though our paths have since diverged, I would like to thank Sophie for her encouragement throughout this project. She has showed me perspectives on life that I would otherwise be ignorant to, and has helped to make me who I am today.

I finally thank Mum and Dad for their constant support, even from afar. Despite the struggles I have faced, they have always believed in me.

Declaration

The work contained in this thesis is original and that no part of it has been submitted for any other degree at this or any other institution. All sources are acknowledged as references.

The development, implementation, and work to obtain results from all versions of the semi-analytical model and the global model was undertaken solely by the author, with guidance from Prof. Timo Gans and Dr. Deborah O'Connell. The full fluid model used as a comparison was developed by Arthur Greb, formerly of the University of York, and used with his kind permission. Details of this model can be found in the works cited, Appendix A, and the thesis entitled "Dynamics of the Plasma-Surface Interface in Capacitively Coupled Radio-Frequency Oxygen Plasmas: Coupling Numerical Simulations with Optical Diagnostics" by Arthur Greb at the University of York, 2013.

Some of the content from Chapters 3 to 7 has been or will be submitted to appear in journals at a later date, and some has been presented at conferences. Recently published is *Bridging the gap between global models and full fluid models: a fast 1D semi-analytical fluid model for electronegative plasmas* by A. Hurlbatt, T. Gans, and D. O'Connell, in Plasma Sources Science and Technology 25, 2016. Work was also presented in *A Fast Four Fluid Model of Electronegative Plasmas Including Non-Isothermal Neutrals and Electrons* at 67th GEC, Raleigh, NC, USA, 2014, and in *Bridging the Gap between Global Models and Full Fluid Models in Electronegative Plasmas* at 68th GEC, Honolulu, HI, USA, 2015.

Chapter 1

Introduction

1.1 Motivation

It would not be an overstatement to say that the use of plasmas in industrial processes such as manufacturing and surface modification is prolific. The ability of low temperature plasmas to provide activation energy for chemical reactions, without the associated heat, and in a manner that allows selectivity and anisotropy, has enabled otherwise impossible technological advances. Uses of plasma range from nanomanufacturing, to spacecraft propulsion, to treatment of chronic wounds, to conversion of industrial waste into carbon based fuels. Despite their widespread use, there is still much about their behaviour that is not understood. The interaction of charged and neutral species over many different length and time scales leads to complex emergent behaviours, the details of which are incredibly difficult to accurately describe.

In order to aid with investigations of such phenomena, plasma scientists often turn to theoretical or numerical representations of plasmas, which are able to describe some aspects of plasma science, through the use of certain assumptions about the way the constituent particles interact. Detailed models are able to capture a large range of phenomena, and can provide information on quantities not accessible through experiment [1]. However, even though the capabilities of computer hardware and software have increased dramatically over the last few decades, creating and running a highly detailed model still poses a substantial challenge. Thus the community has developed models that use a variety of approximations, allowing one to reduce the computational complexity of modelling at the expense of some level of accuracy in the results achieved.

A common approach is to average the ensemble of particles over their thermal motion, resulting in fluid-like equations for the density, flux, temperature etc. of each

species, which can then be solved numerically. Detailed fluid models generally allow for variation in time as well as at least one spatial dimension [1–4]. Typically the equations are solved using a form of finite element analysis, which allows for simple boundary conditions and solutions to capture local effects. Results obtained from these models typically show good agreement with experiment for the limit of medium to high collisionality [1, 4]. However, the computation time required to obtain these results can range from hours to days, depending on the system and the techniques employed.

In order to combat this long time to reach solutions, global models have been developed [5–9], which allow for the solution of bulk properties through a collection of approximations and empirical relations, including the neglection of all spatial derivatives. This allows either rapid convergence to an equilibrium [5] or a description of time evolution of bulk properties [6]. Despite the large number of assumptions made, these models can provide reasonable estimations of bulk values and system trends within a certain parameter space [10]. They are commonly used for systems containing complex chemistries, as their rapid solution allows the inclusion of many different species and reactions, which would be computationally infeasible with full fluid models [11, 12].

Unfortunately, due to the large number of assumptions made, and despite their widespread use, global models are technically only valid for a small subset of discharges. They struggle to provide good results for systems with high degrees of spatial non-uniformity, or atypical discharges where the important empirical relations break down. Their lack of spatial resolution means that they cannot accurately describe systems where a large fraction of the plasma bulk is not uniform, a common occurrence as spatial gradients often exist long before the development of a sheath. The empirical relations used to link bulk values with sheath edge properties fail to account for the different non-linear couplings that can occur for example between non-uniform densities and power deposition profiles.

The work presented here aims to improve the options available to researchers by bridging the gap that exists between global models and full fluid models. Computational complexity is exchanged for analytical intricacy, and differential fluid equations are derived that can be solved in one spatial dimension through an initial value type scheme, thus avoiding the high computation times associated with finite element methods. Example results are given, and compared with a full fluid model [13]. In order to quantify the improvement over a global model, one is also created, and the three models are compared together to show their agreements and limitations.

In addition to this novel semi-analytical depiction of plasmas, equations are developed and included that describe the behaviour of the density and temperature of the neutral gas from which the plasma is created. It has been shown that the effect of a high density plasma on the background gas is non-trivial [14–18], and so not including a full description of neutral properties would be negligent.

1.2 Outline

Chapter 2 provides necessary background knowledge of plasma physics, and derives the fundamental system of equations used in the development of the semi-analytical model. Also detailed are two examples of simple plasma models, to show the processes and difficulties faced by the most basic of descriptions.

Chapter 3 details a semi-analytical model of an isothermal electronegative plasma. Starting at the derivation of the basic equations, the process of normalisation is then described. Once boundary conditions and external parameters are defined, the required numerical techniques are given. Results from the model are analysed, and found to be lacking when compared with a more detailed model.

Chapter 4 extends the analytical framework created in the previous chapter to include electron energy transport. Additional derivation and normalisations are described. Results are compared to the isothermal model, and again to that with more detail. The benefits of including non-uniform electron temperature, and the remaining causes of error are discussed.

Chapter 5 shows the development of a simple global model, and the analytic and numerical methods required. Behaviour and trends are analysed, and compared to the semi-analytical model. Benefits and limitations of the global model are discussed.

Chapter 6 describes the analytical work needed to obtain expressions for the neutral gas properties, and shows the additional numerical schemes required to find solutions to the extended model. Effects of including neutral dynamics are examined, and the leading causes considered.

Chapter 7 compares the semi-analytical, global, and detailed fluid models together. Results from each model are contrasted, and conclusions are drawn as to the efficacy of each one.

Chapter 8 draws conclusions of this work, and details possible future objectives.

Appendix A is a description of the full fluid model used in comparisons across this work.

Chapter 2

Theoretical Background

In order to understand the reasoning, the processes involved, and the outcomes of the work presented in this document, one must first understand some basic concepts of plasmas, generalised theoretical descriptions, numerical techniques, and the steps that go into creating a simple model. This chapter covers the background knowledge required to understand the work presented in the following chapters, and gives the reader an understanding of the difficulties faced in modelling plasmas. For further information on the topics covered, the reader is directed to more comprehensive works aimed at those new to plasma physics, such as [19, 20].

2.1 Background Physics

Plasma, when denoting an ionised gas, is simply an extension of the three 'classical' states of matter. In a simplified view, the transition from solid to liquid and from liquid to gaseous is defined by the breaking of bonds between the constituent particles as more energy becomes available in the system. In the same manner, and again in a simplistic picture, increasing the energy of particles in a gas will eventually lead to the breaking of molecular bonds, if present, and the ionisation of atoms through the escape of electrons. The resulting mixture of charged particles differs in a number of important ways from the gas phase. Mainly, the presence of free charge carriers introduces long range interactions between particles through electromagnetic forces, and thus collective effects appear, such as very high electrical conductivity, coupling of sound waves with magnetic fields, and filamentation.

Unlike collections of charged particles from high voltage devices such as the familiar cathode ray tube, plasmas produce roughly equal numbers of positive and negative

charges. The combination of this and low electron inertia leads to the rapid motion of electrons to neutralise any electric fields that may occur. This results in the concept of 'quasineutrality', whereby the densities of positive and negative charges are roughly equal if one measures above a certain scale length. This length scale, called the Debye length, can be derived through a thought experiment of introducing a positive charge and analysing the motion of the electrons in the electric potential that arises, and is given in (2.1) [21].

$$\lambda_{De} = \left(\frac{\varepsilon_0 k_B T_e}{n_e e^2} \right)^{\frac{1}{2}} \tag{2.1}$$

In (2.1), ε_0 is the permittivity of free space, k_B is the Boltzmann constant, T_e is the electron temperature in degrees Kelvin, n_e is the volumetric density of electrons, and e is the elementary charge. At distances above this length scale, the plasma is able to effectively shield itself from the effect of point charges and external electric fields. The wording of formal definitions of a plasma vary, but their essence is that if a partially ionised gas is larger than the Debye length, and there exist sufficient charged particles within a sphere of radius λ_{De} (the Debye sphere), then collective behaviour of charged particles is significant, and the system is deemed to be in a plasma state [22]. A plasma does not necessarily contain only charged particles, it is possible to have systems where the conditions for a plasma are met even if only fractions of a percent of the gas atoms/molecules are ionised.

The behaviour of shielding charges also leads to a phenomenon known as a 'sheath'. If the plasma is in contact with a body biased to a certain potential, then charged species will move such that the main body of plasma is protected from the intruding potential, and a 'skin' region of non-quasineutrality will exist between the plasma and the body. Even if the body in contact with the plasma is not biased, as is the case with confining walls, then a sheath is created between the plasma and the wall. The electron thermal velocity will be many times that of the ions, due to their small mass, even if the electrons and ions have the same temperature. Thus in a situation where a fully quasineutral plasma is confined by a wall, electrons will be very rapidly lost to the wall. A thin region with net positive charge will be created, a sheath, until the potential across it is sufficient to confine the majority of electrons, and the time averaged current lost to the wall is zero. The potential drop across the sheath will serve to accelerate the comparatively sluggish ions toward the wall, but confine the electrons to the main body of plasma, often termed the 'bulk'.

The potential drop that is required across the sheath in order to confine the majority

of electrons depends on the electron energy distribution function (EEDF), a measure of the probability of a random electron having a particular thermal energy. In a system in thermal equilibrium, this distribution for all species, not just electrons, can be described well by a Maxwell-Boltzmann distribution (commonly termed a 'Maxwellian'), given in (2.2) [19], where m and v are the mass and velocity, respectively, of particles that make up the species.

$$f(v) = n\left(\frac{m}{2\pi k_B T}\right)^{\frac{3}{2}} \exp\left(-\frac{mv^2}{2k_B T}\right) \tag{2.2}$$

If one were to pick a particle at random from a population that had a Maxwellian energy distribution, one would expect it to have a speed of $\langle v\rangle = (8k_B T/\pi m)^{1/2}$, where $\langle v\rangle$ denotes the expectation value of particle speed. The inclusion of the population's temperature, T, in the expression hints at the formal definition of temperature, which is a measure of the mean kinetic energy of particles that can be associated with their thermal motion (as opposed to directed motion; see Section 2.4.3 for more details) [23]. This definition means that the temperature is not necessarily sufficient to fully describe the energy distribution function of a particular species; one must also have information about the shape of this distribution function. Species may have energy distribution functions that cannot be described by a Maxwellian, or indeed by any analytical function, in which case the temperature provides an idea of how energetic the species is, but cannot give the whole picture.

The concept of temperature is one that, in everyday life, is applied as a single number to a substance. However there is no reason why a plasma, with its separate constituents, cannot have different temperatures for each species. Indeed, this is exactly the property that is exploited in so-called 'low temperature' plasmas. These are plasmas in which the heavy particles typically have a temperature close to that of room temperature ($\approx 300\,\mathrm{K}$), and not usually higher than 1000 K. In contrast the electrons may have temperatures of 50 000 K or more, often expressed not in Kelvin but instead as the mean electron energy measured in electron volts (eV), with $1\,\mathrm{eV} \approx 11\,604.5\,\mathrm{K}$ for a Maxwellian.

This state of non-thermal equilibrium is maintained by giving energy mainly to the electrons, and by ionising only a small fraction of the constituent particles. Due in part to their small mass, the energy transfer from the electrons to other particles is relatively inefficient. Any energy that is given to ions is efficiently transferred to

the comparatively dense neutral gas, where it is quickly dissipated as heat. This large disparity in temperatures allows one to create a complex chemical environment through electron impact reactions, without the need for aggressive chemicals or solvents. This has meant that they have found use in many branches of science, from the manufacture of nanoscale devices, to altering the wettability of fabrics, to the treatment of chronic wounds.

In order to sustain such a plasma, it stands to reason that there must be a net energy deposition into the electrons in order to maintain their high temperature. This is provided in the form of externally applied electrical fields, and the fast moving electrons interact with these fields in a number of ways. One important mechanism is that of ohmic heating, whereby electrons accelerated by an electric field collide with other particles, thereby randomising their velocity and so converting energy from the electric field into thermal energy. The term 'ohmic' arises due to this mechanism being intrinsically linked to the resistivity of the plasma.

A common approach is to excite the plasma with a sinusoidal electric field, often at radio frequencies (RF) in the kHz or MHz range. At the higher frequencies, the electric field is able to be followed only by the low inertia electrons, and has very little effect on the heavy ionic species. Depending on the precise mechanism of electrical power deposition, the oscillating electric field can cause a modulation of the sheath width. In capacitative discharges, the plasma can be visualised as held between two conducting plates, one held at ground, and to the other an RF voltage is applied. In this scenario, depicted in figure 1, electrons will oscillate between the two electrodes, and sheaths will form on both sides, that grow and shrink with the RF cycle. The boundary between the bulk of the plasma and the sheath, or sheath edge, is described by a sudden drop in electrical potential. As the electrons have a velocity distribution, as discussed above, some may move in such a way as to impinge upon the potential barrier of the oscillating sheath edge. This will cause the electron to gain energy if the sheath is expanding, or lose it if the sheath is contracting. However the effect averaged over a whole RF cycle is a net energy gain [19]. The concept of electron heating from the oscillating sheaths is known as 'stochastic' or 'collisionless' heating, and although the description given above is logical, the precise mechanism of energy deposition and transfer is still an active topic of research [24–27].

When a sheath exists between the plasma and a surface, either stationary or oscillatory, then positive ions are accelerated by the potential gradient that exists there.

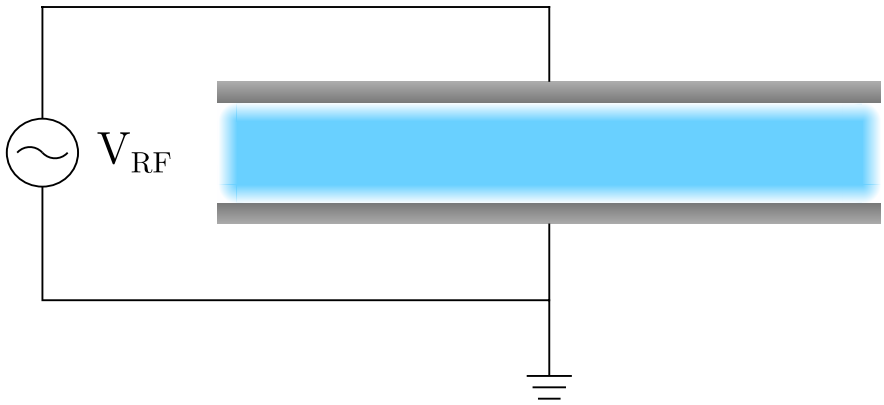

Figure 1: Simplified schematic of a radio frequency driven capacitively coupled plasma.

These ions can impact on the surface with a kinetic energy equivalent to a significant fraction of the RF driving voltage. The energy that the ion brings to the surface can be transmitted to an electron, which may then escape from the surface. This is known as secondary electron emission. The released electron is then accelerated away from the surface by the sheath voltage, and so gains a large amount of energy, helping to heat the plasma. It is possible in certain systems for this emission of secondary electrons to be the dominant mechanism in sustaining the plasma, which is referred to as γ-mode.

One is able to obtain information about the transition between the bulk and the sheath through the use of a variety of assumptions to derive some simple analytical relations. One of those commonly used is the Bohm criterion, which gives a minimum positive ion velocity required to sustain a sheath (2.3).

$$u_B = \left(\frac{k_B T_e}{m_i} \right)^{\frac{1}{2}} \tag{2.3}$$

This is derived by using the assumptions of Maxwellian electrons, cold ions (so that $T_i = 0\,\mathrm{K}$), and no electron drifts for a collisionless DC sheath. Despite these assumptions in the original derivation, this condition has been shown to be valid for similar assumptions in an RF plasma [28]. Corresponding relationships have been derived for other systems, such as those containing negative ions [29], whose presence impacts on the equations for plasma potential used to derive (2.3). The appearance of negative ions in plasmas has other major effects; see Section 2.6.2 for further discussion.

When early experimenters were investigating the behaviour of DC discharges formed between two parallel electrodes, it was found that there was an unusual link between the gas pressure, the inter-electrode distance, and the voltage required to create a

plasma. As one varied either the pressure or the gap size, one found there was a value of each that gave a minimum breakdown voltage. Values too high or too low caused the required voltage to rise. Through observations, it was discovered that the critical parameter for determining the breakdown voltage was the product of the gas pressure and inter-electrode distance [30]. Through changing the pressure and gap size simultaneously, it was found that maintaining their product constant also kept the breakdown voltage roughly the same over a large pressure range from around 13 kPa to 100 kPa. With a modern understanding of sheath physics, ionisation processes, and secondary electron emission, it is possible to derive an expression that demonstrates this, given in (2.4).

$$V_b = \frac{Bpl}{\ln Apl - \ln\left[\ln\left(1 + 1/\gamma_{se}\right)\right]} \tag{2.4}$$

Here, the breakdown voltage V_b is calculated from the pressure-length product pl, the secondary electron emission coefficient γ_{se} which is dependent mainly on the electrode material, and the parameters A and B are determined experimentally, and found to be roughly constant for any given gas [19]. This expression is often referred to as the Paschen law, after the discoverer of the precursory empirical relationship. The pressure-length product has been found to be applicable not just to DC discharges, but also as a similarity parameter for RF excited discharges [31–33]. Plasmas that are markedly different in their pressure or gap size will exhibit comparable behaviours if they share the same pressure-length product, and it can also be seen in the requirement for atmospheric pressure plasmas to be many times smaller than those operated at low pressure.

2.2 Types of Plasma Model

Experimental plasma physics has made enormous progresses over the last few decades, and researchers are able to measure an extraordinary variety of plasma properties, however the complete diagnostic characterisation of low temperature plasmas is still a far away aspiration. Until such a time, researchers will turn to models of plasmas in an attempt to fill the gaps in their knowledge of a particular phenomena. When looking to models of a plasma, researchers face a number of choices. Principle among these is how much information about the plasma is required, how accurate it needs to be, and how much computing power they have available. Typically if one requires only general trends of a simplified system, then an analytic model can be used, which uses broad

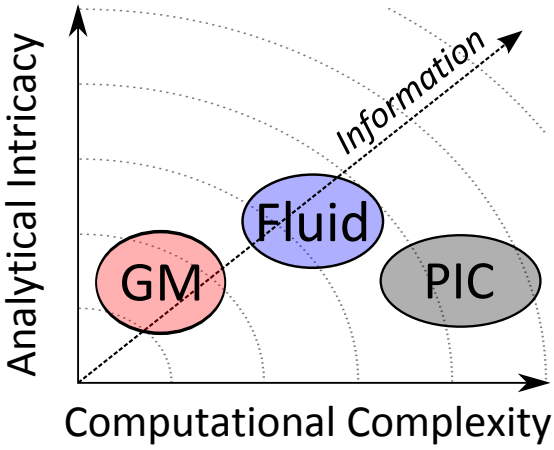

Figure 2: Conceptual comparison of the three main types of plasma model.

assumptions to build a system of analytical expressions that describe some aspects of a plasma. This type of model is usually difficult to develop, but simple to use and can provide useful information on system trends and links between phenomena.

If, however, one requires more than a simple description of plasma properties or dynamics, then one must turn to numerical models. These use numerical methods to describe systems that cannot be described by analytically solvable equations. Ideally one would create a system that could apply first principles to each particle found within the plasma, and thus completely detail all aspects of the plasma. Despite the capabilities of computer hardware and software increasing dramatically since the advent of scientific computing, creating and running such a model is still a technical impossibility. Thus the community have developed models that use a variety of approximations, that allow one to reduce the computational complexity of modelling at the expense of some level of accuracy in the results achieved. This has resulted in models that can be broadly grouped into three distinct categories, depending on the assumptions made and solution methods employed. These three categories, detailed below, can be described by their analytical and computational difficulty, and contrasted by the amount and quality of information they provide, as shown in figure 2.

One simple approximation to make is that particles within the system can be collected into so-called 'macro' or 'super' particles, each one representing 10^5 to 10^9 physical particles [34–37]. This way the memory requirements of the model are reduced to feasible amounts, but the computational complexity is still extreme. Calculating the interactions between each element of an ensemble of $\approx 10^5$ macroparticles is still a huge computational load, and would require an impractical amount of time to calculate anything useful. Thus models have been developed where the system domain is divided

into units called 'cells', each containing a few hundred macroparticles. When calculating the influence of the ensemble on a single macroparticle, one applies the usual formulae for interaction partners within the same cell, but the effect of macroparticles found elsewhere is averaged to their nearest cell boundary. Thus the effective number of interaction partners, and so the computational load, is greatly reduced.

This type of model, called a particle-in-cell (PIC) model, is typically able to provide a great deal of information about the plasma, but still requires a large amount of computing power. As these models treat particles and solve Maxwell's equations directly, they need not make any assumptions about energy distribution functions, and can thus provide such information as an output. However due to the direct treatment of particles, the model naturally becomes more computationally expensive for systems that introduce more particles, be this through geometry, system pressure, or otherwise. Thus these models are typically limited to one or two dimensional descriptions of lower pressure systems, where the number of particles is low, as is the frequency of collisions. For systems where these conditions are met, PIC models tend to show very good agreement with experiment, indeed it has been claimed that the results of PIC models are "at least as accurate as those produced by any other technique" [38]. Unfortunately, model time steps need to be low to capture all effects, and so these models can take many days of real time to find solutions.

If the system to be modelled is comprised of species that can be approximated by a particular energy distribution, then one can average the ensemble of particles over their thermal motion resulting in fluid-like equations for the density, flux, temperature etc. of each species, which can then be solved numerically. This process of thermal averaging will be discussed in Section 2.4. Detailed fluid models generally allow for variation in time as well as at least one spatial dimension [1–4]. Usually the equations are solved using a form of finite element analysis, which allows for simple boundary conditions and solutions to capture local effects. Results obtained from these models typically show good agreement with experiment for the limit of medium to high collisionality [1, 4]. However, the relaxation time of these solutions can range from hours to days, depending on the system and the techniques employed.

In order to combat this long time to reach solutions, global models have been developed [5–9], which allow for the solution of bulk properties through a collection of approximations and empirical relations, including the neglection of all spatial derivatives. This allows either rapid convergence to an equilibrium [5] or a description of time

evolution of bulk properties [6]. Despite the high number of assumptions made, these models can provide reasonable estimations of bulk values and system trends within a certain parameter space [10]. They are commonly used for systems containing complex chemistries, as their rapid solution time allows the inclusion of incredibly large numbers of species and reaction pathways, which would be computationally infeasible with full fluid models [11].

Unfortunately, due to the large number of assumptions made, and despite their widespread use, global models are technically only valid for a small subset of discharges. They struggle to provide good results for systems with high degrees of spatial non-uniformity, or atypical discharges where the important empirical relations break down. Their lack of spatial resolution means that they cannot accurately describe systems where a large fraction of the plasma bulk is not uniform, a common occurrence as spatial gradients often exist long before the development of a sheath. The empirical relations used to link bulk values with sheath edge properties fail to account for the different non-linear couplings that can occur for example between non-uniform densities and power deposition profiles.

The three types of model detailed above are just the most common categories into which plasma models are grouped. Models exist that combine aspects from the different categories, or take a different approach entirely. A common form of 'hybrid' model is one that combines a kinetic treatment of electrons with a fluid description of the heavy particle dynamics. This can take into account the often large deviations from a Maxwellian energy distribution function that occurs in electrons, while allowing the quicker solution of the heavy species which can remain approximately Maxwellian.

This work details the development of a different type of hybrid model, one that builds on the analytical basis of fluid models, but extends it as far as possible analytically before resorting to numerical methods. This new type of semi-analytical modelling allows the use of much faster numerical schemes than full fluid models as they are described above, through the casting of the equations as an initial value problem. However unlike global models, they can retain a level of spatial resolution, as well as including most effects self consistently. This leads to a model of accuracy that approaches that of a full fluid model, but has the computational characteristics of a global model. Like fluid models, it is based on averaging species of particles over their thermal motion, through what is known as the Boltzmann equation, the derivation and use of which is treated in Section 2.4.

2.3 Particle interactions

A plasma, as discussed, can be considered as a multicomponent gas of interacting particles. The plasma properties then depend heavily on the interactions of these particles with fields, be these external or internal to the plasma. Interactions with short range fields from other particles are usually referred to as collisions, despite the concept of physical contact losing meaning at atomic scales.

2.3.1 Collision concepts

Collisions fall into two distinct categories. In elastic processes there is a conservation of mass, momentum, and kinetic energy such that there are no changes to the internal states of particles, and there is also no creation or destruction occurring. Should any internal states be changed, or particles be created or destroyed, then the collision is inelastic, as there is a transfer between kinetic and other forms of energy. This includes processes such as excitation, ionisation, or dissociation of molecular species.

It is also important to distinguish interactions between charged particles, as these involve the Coulomb force, and therefore take place at length scales much larger than the atomic scale. This means that charged particles are able to interact simultaneously with many others, whereas the fields from neutral species are strong only within the electronic shell, and so collisions with neutrals are usually binary, or rarely three-body, depending on the particle density. Despite this, the long range Coulomb interactions can be approximated as multiple small binary collisions, and weakly ionised plasmas are well described by this.

For the short range collisions, one can turn to the kinetic theory of gases, in which particle motion is divided into collisions and the intervals between these collisions. As the length and time scales of these collisions are much smaller than of other processes, external fields can be neglected during collisional processes, and particle interactions neglected between collisions. When determining the overall behaviour of particles, the actual trajectories during a short range collision process do not need to be resolved, and it is sufficient to know only the effect of each collision.

As collisional processes in plasmas involve the interaction of atomic and sub-atomic species, theoretical considerations and predictions should be made using quantum mechanics. However the outcomes of a classical treatment are valid to a good approximation, and the procedures and concepts developed are still useful.

In order to build an understanding of the concepts involved with collisional processes

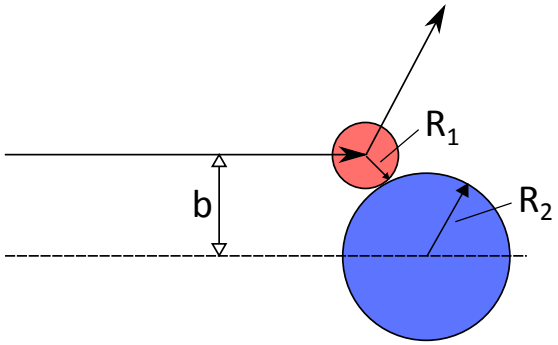

Figure 3: Schematic of a binary collision between two hard spheres.

in a plasma, it is useful to begin with consideration of a simple elastic collision between two hard spheres, with a lighter 'projectile' of radius R_1 moving in the rest frame of a heavier 'target' of radius R_2. A collision only occurs if the two spheres come into contact, which can be determined by measuring the distance between their centres; if this distance is equal to the sum of their radii, $R_T = R_1 + R_2$, then a collision occurs. In order for this to happen, the initial trajectory of the projectile must be such that the distance between the trajectory and a parallel line drawn through the centre of the target, the impact parameter b, is less than R_T, as shown in figure 3. As this process is happening in three dimensional space, the requirement on the impact parameter becomes such that for a collision to occur, the projectile must be 'aimed' at a circle of diameter R_T centred on the target. The area of this circle, $\sigma = \pi R_T^2$, is known as the cross section of the interaction, and is a measure of the likelihood of collision.

Although the picture of single particle interactions is useful, in reality reactions occur between ensembles of particles, and more statistical description is required. This is done by considering now a uniform 'beam' of the previous projectile particles with flux Γ incident on a slab of targets, with a target density of n_g, thickness $\mathrm{d}x$ and surface area A. The fraction of projectiles lost from the beam can be found from the total number of target particles $n_g A \mathrm{d}x$ and how large their cross section is relative to the beam area, as given in (2.5).

$$\begin{aligned} \frac{\mathrm{d}\Gamma}{\Gamma} &= -n_g A \mathrm{d}x \frac{\sigma}{A} \\ \frac{\mathrm{d}\Gamma}{\mathrm{d}x} &= -\Gamma n_g \sigma \end{aligned} \tag{2.5}$$

This expression is simple to integrate in space, yielding an exponential decay, with a characteristic length scale of $\lambda = (n_g \sigma)^{-1}$, which is the mean free path, and a measure of the average distance a projectile will travel before colliding with a target. From the

mean free path and the velocity of the projectile beam v, one can also obtain a mean time between collisions as $\tau = \lambda/v$. Concepts that will be used heavily in this work are the inverse of this time scale, the collision frequency $\nu = n_g \sigma v$ and subsequently the collision rate coefficient, being the collision frequency per unit density of the target particles $K = \nu/n_g = \sigma v$.

2.3.2 Real collisions

Each of the concepts detailed above is simple to understand in the case of hard sphere interactions, however the situation becomes significantly more complicated when one turns to collisions between real atomic or subatomic particles. The description of classical mechanics is no longer valid, and one must turn to quantum descriptions of phenomena, which are beyond the scope of this work. The most important outcome of the quantum description is that the cross sections for interactions becomes dependent on the impact velocity, and thus energy, of the associated particles. For example, in noble gases the elastic scattering of electrons from neutral, ground state, atoms is non-monotonic with the energy of the impacting electron. It was found that the mean free path of an electron in Argon has a maximum when the incident electrons have an energy of roughly 0.3 eV [39]. As classical mechanics dictates that the cross section for an elastic collision is independent of energy, this feature was not explained until the advent of quantum mechanics, and can be predicted through wave-like treatment of an electron incident on a potential well.

Due to the unintuitive behaviour of collision parameters and their energy dependence, obtaining values that can be used in numerical models is not trivial. Quantum mechanical calculations can and have been performed for simple systems such as Helium [40] or Lithium [41], however they pose a significant challenge for more complex systems. As such researchers have to rely on experimental measurements for values of cross sections, collision frequencies, and the subsequent transport parameters and rate coefficients.

Unfortunately the number of reactions that need to be considered, even for a comparatively simple gas mixture, can be large. For example, recent work on a fluid model of a helium-oxygen gas mixture considered 16 species and 116 reactions [2]. The addition of realistic amounts of humid air to this system increased this to 59 species and 1048 reactions [9], which required the use of a global model, and was still not a comprehensive set of all possible reactions. A similar model of an argon/humid air

plasma included 85 species and 1928 reactions [42]. Thus the amount of experimental work that needs to go into measuring properties of various gases and gas mixtures is immense, and so has been spread over a large number of research groups and many decades of work. This creates issues in traceability, and it can often be difficult to find primary sources for measurements. Thus values obtained from the literature are often of unknown validity or accuracy. It is also sometimes unclear if given values are measurements, calculations, or simply estimates. Results from models, simulations, and occasionally experiments, are being legitimately called into question, as their outcomes depend intricately on the values used for reaction rate coefficients (RRCs), and so an unknown uncertainty on these values creates an unknown uncertainty in the results. Although awareness of the issues surrounding plasma chemistry models is increasing, and work is being done to address some of them [43], it is still difficult to say with certainty that reaction rate coefficients being used are accurate. Despite this, the focus of this work is on the modelling technique itself, and not the precise quantitative results for comparison with experiment. Thus cross sections and rate coefficients from the literature are used.

2.3.3 Obtaining reaction rate coefficients

To obtain the most accurate values possible for reaction rate coefficients, it is necessary to account for the energy dependence of cross sections, as discussed above. Values for reaction rate coefficients are obtained through the multiplication and subsequent integration over all energies of the energy dependent cross section, the species energy distribution function, and the species velocity. Therefore it is necessary to know these quantities over a large range of energies. As mentioned above, cross sections can be obtained to reasonable accuracy through either quantum calculations or well designed experiments. However the energy distribution function is not always known.

One possible route is to assume that all species have a Maxwellian energy distribution function with a characteristic temperature. This way an analytical form is known for the distribution function, and the integration is trivial. However the assumption of a Maxwellian is often not valid, particularly for the electrons in a low pressure system [44–46], and so calculations of reaction rate coefficients may be over or underestimated by many orders of magnitude (see figure 4 for example). Therefore it is desirable to have an estimate of the EEDF, and calculations of reaction rate coefficients from it.

It is possible to obtain a much more rigorous approximation of the EEDF for a given set of conditions from a set of energy dependent cross sections. This is achieved through the numerical solution of a simplified version of the electron Boltzmann equation,given in (2.16), as implemented in the widely used tool BOLSIG+ [47]. An assumption is made that in the absence of a magnetic field, the electric field and all collision probabilities are uniform over the spatial scale of the electron mean free path. This then allows one to express the Boltzmann equation in spherical coordinates, and to then simplify the angular dependence through the expansion into spherical harmonics. It has been found that using more than the first two terms in this expansion gives a negligible improvement in solutions, apart from under extreme conditions [46]. It is also the case that approximations used in fluid models break down within the same region of parameter space, so the use of more detailed expansions for fluid models is moot. Further to the use of spherical harmonics, BOLSIG+ also simplifies the Boltzmann equation by assuming a steady state electric field and an EEDF that is constant in both space and time. Instead a spatial and time dependent electron density is used to account for these changes, through an exponential growth model.

The effects of collisions are carefully considered, and separate terms are used to account for the elastic, (de)excitation, ionisation, attachment, and electron-electron collision processes. From these considerations, a differential equation can be constructed to describe the EEDF as a function of electron energy. BOLSIG+ solves this equation numerically through a finite element method and discretising in energy space. It is able to provide an EEDF from a given value of the normalised electric field strength, but from this EEDF a mean electron energy (T_e) can be found. The tabulated values of interaction cross section with electron energy are then used to find reaction rate coefficients for the given EEDF. It is then a simple matter of running the solver multiple times for different conditions to provide a table of reaction rate coefficients as a function of T_e.

As an example of the occasionally striking differences between possible reaction rate coefficients, figure 4 shows values obtained via BOLSIG+ compared with relations taken from the literature [9, 48–51] for the electron impact ionisation of O_2 into O_2^+. While the data from BOLSIG+ calculates the EEDF, the formulae used by the references given are found by assuming a Maxwellian EEDF and combining this with measured cross sections. Clearly the difference between these two approaches is significant, but even among the Maxwellian assumptions there are differences approaching one order

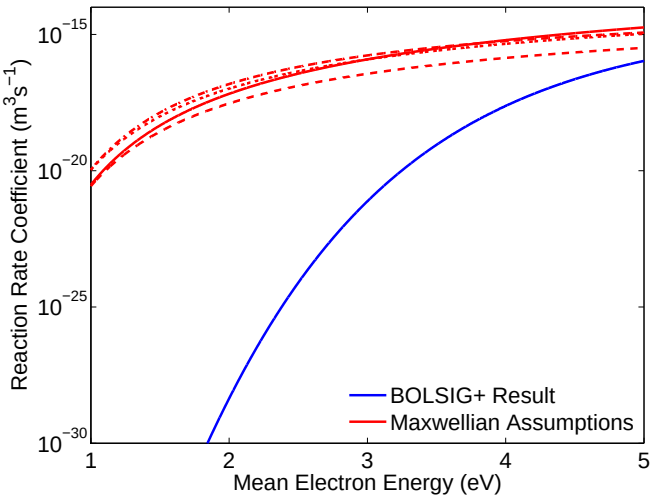

Figure 4: Comparison of different estimates of the reaction rate coefficient for ionisation of molecular oxygen through electron impact, as a function of mean electron energy.

of magnitude. This demonstrates the aforementioned difficulties that researchers face when choosing chemistries and the associated reaction rate coefficients.

2.4 The Boltzmann Equation and its Moments

As with many systems that consist of a large number of particles, a statistical description is well suited to plasmas. This makes use of a distribution function: a mathematical construction that describes the position and velocity of every particle in the system at a given point in time. Through averaging this distribution function, one can extract macroscopic values, such as density and temperature, that represent observations of the ensemble of particles.

In order to describe a particle's position and velocity, one first needs a system to do so. A particle in Cartesian coordinates can be described as having a position $\boldsymbol{r} = \hat{\imath}x + \hat{\jmath}y + \hat{k}z$, where $\hat{\imath}, \hat{\jmath}, \hat{k}$ refer to unit vectors of the principle axes of the coordinate system. A similar orthogonal coordinate system can be imagined for the particle velocity, so that $\boldsymbol{v} = \hat{\imath}v_x + \hat{\jmath}v_y + \hat{k}v_z$. These two coordinate systems, referred to as configuration space and velocity space respectively, can be combined into a single six-dimensional phase space. Each particle is then represented by a single point in this space, and as particles move or accelerate, their representative points describe a trajectory through the phase space. Thus a complicated system of a large number, N, of particles, can be fully described at a given time by N points in phase space.

From the placement of points within phase space, one can create a distribution

function $f_\alpha(\boldsymbol{r}, \boldsymbol{v}, t)$ that describes the density of points at every position in space that represent particles of type α. This scalar function is positive and finite, as well as continuous, and must also tend toward zero for large values of $\boldsymbol{v}$. As this distribution function contains a full description, one can obtain macroscopic values and properties of the system through its manipulation. For example, if $f_\alpha(\boldsymbol{r}, \boldsymbol{v}, t)$ is independent of $\boldsymbol{r}$ and t, isotropic in (does not depend on the direction of) $\boldsymbol{v}$, then the particles of type α are in thermal equilibrium.

For numerical properties, one must take various averages of the distribution function, as mentioned above. For example, to find particle density as a function of space, one takes the velocity average of the distribution function through integration, as given in (2.6).

$$n_\alpha(\boldsymbol{r}, t) = \int_{\boldsymbol{v}} f_\alpha(\boldsymbol{r}, \boldsymbol{v}, t)\ d^3\boldsymbol{v} \tag{2.6}$$

Similarly, to find the average particle velocity, which would represent an organised flow of particles, one must multiply the distribution function by particle velocity, integrate over all velocities, then divide by the number of particles in the volume of integration. This results in (2.7).

$$\boldsymbol{u}_\alpha(\boldsymbol{r}, t) = n_\alpha^{-1}(\boldsymbol{r}, t) \int_{\boldsymbol{v}} \boldsymbol{v} f_\alpha(\boldsymbol{r}, \boldsymbol{v}, t)\ d^3\boldsymbol{v} \tag{2.7}$$

This demonstrates how one can use the distribution function to find macroscopic properties, but one must also be able to find the distribution function itself. Its behaviour in time and phase space is described by the Boltzmann Equation, and following is a brief derivation [23, 52].

2.4.1 The Boltzmann Equation

Consider that each particle described by $f_\alpha(\boldsymbol{r}, \boldsymbol{v}, t)$ is acted on by an external force $\boldsymbol{F}$. A particle at position $(\boldsymbol{r}, \boldsymbol{v})$ at a time t will find itself at a new location $(\boldsymbol{r}', \boldsymbol{v}')$ at a time $t + dt$. It then follows that the new position can be described by a pair of Newtonian equations, (2.8) and (2.9), where $\boldsymbol{a} = \boldsymbol{F}/m_\alpha$ is the acceleration of each particle due to the external force.

$$\boldsymbol{r}'(t + dt) = \boldsymbol{r}(t) + \boldsymbol{v}\, dt \tag{2.8}$$

$$\boldsymbol{v}'(t + dt) = \boldsymbol{v}(t) + \boldsymbol{a}\, dt \tag{2.9}$$

Neglecting collisions for the moment, all particles in the initial volume element $d^3r\ d^3v$ will be in a new volume element, $d^3r'\ d^3v'$ after time dt. This is described by (2.10).

$$f_\alpha(\boldsymbol{r}', \boldsymbol{v}', t + dt)\ d^3\boldsymbol{r}'\ d^3\boldsymbol{v}' = f_\alpha(\boldsymbol{r}, \boldsymbol{v}, t)\ d^3\boldsymbol{r}\, d^3\boldsymbol{v} \tag{2.10}$$

The volume element itself may change due to particle motion; the relationship between the old and new volumes is described by the Jacobian of the transformation. For (2.8) and (2.9) the Jacobian can be shown to be unity [23] so that $d^3\boldsymbol{r}'\, d^3\boldsymbol{v}' = d^3\boldsymbol{r}\, d^3\boldsymbol{v}$. This then allows (2.10) to become (2.11).

$$\left[f_\alpha(\boldsymbol{r}', \boldsymbol{v}', t + dt) - f_\alpha(\boldsymbol{r}, \boldsymbol{v}, t)\right]\ d^3\boldsymbol{r}\, d^3\boldsymbol{v} = 0 \tag{2.11}$$

As the time interval dt is considered small, one can Taylor expand the new distribution function about the old, neglecting terms of order dt^2 and higher, as shown in (2.12).

$$\begin{aligned} f_\alpha(\boldsymbol{r} + \boldsymbol{v}\ dt, \boldsymbol{v} + \boldsymbol{a}\ dt, t + dt) &= f_\alpha(\boldsymbol{r}, \boldsymbol{v}, t) \\ &+ \left[\frac{\partial f_\alpha}{\partial t} + \left(v_x\frac{\partial f_\alpha}{\partial x} + v_y\frac{\partial f_\alpha}{\partial y} + v_z\frac{\partial f_\alpha}{\partial z}\right)\right. \\ &\left. + \left(a_x\frac{\partial f_\alpha}{\partial v_x} + a_y\frac{\partial f_\alpha}{\partial v_y} + a_z\frac{\partial f_\alpha}{\partial v_z}\right)\right]\ dt + \mathcal{O}(dt^2) \end{aligned} \tag{2.12}$$

Using the common differential operators for both configuration and velocity space (2.13) and (2.14), and inserting the result of (2.12) into (2.11), one arrives at (2.15), known as the Boltzmann Equation.

$$\boldsymbol{\nabla} = \hat{i}\frac{\partial}{\partial x} + \hat{j}\frac{\partial}{\partial y} + \hat{k}\frac{\partial}{\partial z} \tag{2.13}$$

$$\boldsymbol{\nabla}_{\boldsymbol{v}} = \hat{i}\frac{\partial}{\partial v_x} + \hat{j}\frac{\partial}{\partial v_y} + \hat{k}\frac{\partial}{\partial v_z} \tag{2.14}$$

$$\frac{\partial f_\alpha}{\partial t} + \boldsymbol{v}\cdot\boldsymbol{\nabla} f_\alpha + \boldsymbol{a}\cdot\boldsymbol{\nabla}_{\boldsymbol{v}} f_\alpha = 0 \tag{2.15}$$

Note that (2.15) is a conservative equation, and, as stated above, neglects collisions and particle interactions. The effect of collisions on the system is to add or remove particles from the volume element being considered between the times t and $t + dt$. This consideration actually results in a simple modification to (2.15), with the effect of collisions on the distribution function replacing the conservative zero, as shown on

the right hand side (RHS) of (2.16).

$$\frac{\partial f_\alpha}{\partial t} + \boldsymbol{v} \cdot \boldsymbol{\nabla} f_\alpha + \boldsymbol{a} \cdot \boldsymbol{\nabla}_{\boldsymbol{v}} f_\alpha = \left.\frac{\delta f_\alpha}{\delta t}\right|_c \tag{2.16}$$

The precise form for $(\delta f_\alpha / \delta t)|_c$ is not trivial, and depends on the system being analysed and the assumptions being made. More details of this collision term will be discussed in Section 2.4.4.

2.4.2 The General Transport Equation

Similarly to how macroscopic values can be obtained through multiplication then integration of the distribution function, the equations describing the temporal and spatial variation of the macroscopic quantities can also be found from applying a similar process to (2.16) [23]. Let $\chi(\boldsymbol{v})$ represent some function of particle velocity that gives one of the macroscopic quantities. By multiplying (2.16) by $\chi(\boldsymbol{v})$ and integrating over all $\boldsymbol{v}$, one obtains a transport equation for the macroscopic quantity described by χ. The multiplication by $\chi(\boldsymbol{v})$ and inclusion of the velocity integrals results in (2.17), which will be solved over the next few equations.

$$\int_{\boldsymbol{v}} \chi \frac{\partial f_\alpha}{\partial t}\, d^3\boldsymbol{v} + \int_{\boldsymbol{v}} \chi \boldsymbol{v} \cdot \boldsymbol{\nabla} f_\alpha \, d^3\boldsymbol{v} + \int_{\boldsymbol{v}} \chi \boldsymbol{a} \cdot \boldsymbol{\nabla}_{\boldsymbol{v}} f_\alpha \, d^3\boldsymbol{v} = \int_{\boldsymbol{v}} \chi \left.\frac{\delta f_\alpha}{\delta t}\right|_c d^3\boldsymbol{v} \tag{2.17}$$

For the first term in (2.17):

$$\begin{aligned} \int_{\boldsymbol{v}} \chi \frac{\partial f_\alpha}{\partial t}\, d^3\boldsymbol{v} &= \frac{\partial}{\partial t} \int_{\boldsymbol{v}} \chi f_\alpha \, d^3\boldsymbol{v} - \int_{\boldsymbol{v}} f_\alpha \frac{\partial \chi}{\partial t}\, d^3\boldsymbol{v} \\ &= \frac{\partial}{\partial t} \left(n_\alpha \langle \chi \rangle \right) \end{aligned} \tag{2.18}$$

$$\langle \chi(\boldsymbol{r}, t) \rangle = \frac{1}{n_\alpha(\boldsymbol{r}, t)} \int_{\boldsymbol{v}} \chi(\boldsymbol{r}, \boldsymbol{v}, t) f_\alpha(\boldsymbol{r}, \boldsymbol{v}, t) \, d^3\boldsymbol{v} \tag{2.19}$$

In (2.18), the independence of the velocity integration on time is used to separate the terms, and the second term on the RHS vanishes due to the dependence of χ on only $\boldsymbol{v}$. In (2.18) and following expressions in this section, $\langle \chi \rangle$ denotes the average value of χ with respect to velocity space, as defined by (2.19). Comparable logic can be used on the second term in (2.17), since configuration space, velocity space, and

time coordinates are independent. This results in a second average term.

$$\begin{aligned}\int_{\boldsymbol{v}} \chi \boldsymbol{v} \cdot \boldsymbol{\nabla} f_\alpha \; d^3\boldsymbol{v} &= \boldsymbol{\nabla} \cdot \int_{\boldsymbol{v}} \boldsymbol{v} \chi f_\alpha \; d^3\boldsymbol{v} - \int_{\boldsymbol{v}} f_\alpha \boldsymbol{v} \cdot \boldsymbol{\nabla} \chi \; d^3\boldsymbol{v} \\ &\quad - \int_{\boldsymbol{v}} f_\alpha \chi \boldsymbol{\nabla} \cdot \boldsymbol{v} \; d^3\boldsymbol{v} \qquad (2.20) \\ &= \boldsymbol{\nabla} \cdot (n_\alpha \langle \chi \boldsymbol{v} \rangle) \qquad (2.21)\end{aligned}$$

The third term of (2.17) can be expanded similarly, but the resulting integrals are slightly more technical.

$$\begin{aligned}\int_{\boldsymbol{v}} \chi \boldsymbol{a} \cdot \boldsymbol{\nabla}_{\boldsymbol{v}} f_\alpha \; d^3\boldsymbol{v} &= \int_{\boldsymbol{v}} \boldsymbol{\nabla}_{\boldsymbol{v}} \cdot (\boldsymbol{a} \chi f_\alpha) \; d^3\boldsymbol{v} - \int_{\boldsymbol{v}} f_\alpha \boldsymbol{a} \cdot \boldsymbol{\nabla}_{\boldsymbol{v}} \chi \; d^3\boldsymbol{v} \\ &\quad - \int_{\boldsymbol{v}} f_\alpha \chi \boldsymbol{\nabla}_{\boldsymbol{v}} \cdot \boldsymbol{a} \; d^3\boldsymbol{v} \qquad (2.22)\end{aligned}$$

For the first term on the RHS of (2.22), the integral can be expressed as the sum of three triple integrals, each of the form (2.23). As detailed previously, the distribution function must vanish as the velocity approaches infinity, as no physical system exists where particles have infinite velocity. Thus the three parts are each zero, and so the first term of (2.22) is also zero.

$$\iiint \frac{\partial}{\partial v_x} (a_x \chi f_\alpha) \; dv_x \, dv_y \, dv_z = \iint \left(\boldsymbol{a} \chi f_\alpha \Big|_{-\infty}^{+\infty} \right) \; dv_y \, dv_z \qquad (2.23)$$

The last term of (2.22) also vanishes if one can assume that the components of the external force applied are independent of the corresponding velocity components. Therefore one is left with only the central term, which can be formulated as the integral found in (2.19). Thus the third term of (2.17) becomes a third average term, as given in (2.24).

$$\int_{\boldsymbol{v}} \chi \boldsymbol{a} \cdot \boldsymbol{\nabla}_{\boldsymbol{v}} f_\alpha \; d^3\boldsymbol{v} = -n_\alpha \langle \boldsymbol{a} \cdot \boldsymbol{\nabla}_{\boldsymbol{v}} \chi \rangle \qquad (2.24)$$

Collecting the results of (2.18), (2.21) and (2.24), one obtains the general transport equation, (2.25), where the term on the RHS represents the change in χ due to collisions.

$$\frac{\partial}{\partial t} (n_\alpha \langle \chi \rangle) + \boldsymbol{\nabla} \cdot (n_\alpha \langle \chi \boldsymbol{v} \rangle) - n_\alpha \langle \boldsymbol{a} \cdot \boldsymbol{\nabla}_{\boldsymbol{v}} \chi \rangle = \frac{\delta}{\delta t} (n_\alpha \langle \chi \rangle) \Big|_c \qquad (2.25)$$

2.4.3 Moments of the Boltzmann Equation

Using the general transport equation (2.25), one can replace χ with various functions to find expressions that describe the transport of macroscopic properties of the plasma.

These are known as moments of the Boltzmann Equation, and the order of the moment is determined by the power of $\boldsymbol{v}$ found in χ. The result is a set of equations that describe the behaviour of the plasma approximated as a fluid that has the macroscopic properties of density, velocity, pressure and so forth, determined by the averages over the particle distribution function. In this section, the subscript denoting that terms can be applied to any particle has been omitted for brevity.

To find the zeroth moment, one uses $\chi = 1$ and substitutes into (2.25) the following terms, arriving at (2.26). The result for the second term uses the expansion of $\boldsymbol{v} = \boldsymbol{u} + \boldsymbol{w}$, where $\boldsymbol{u}$ and $\boldsymbol{w}$ represent the directional (flow) and random (thermal) components of particle velocity, respectively.

$$\begin{aligned} \langle \chi \rangle &= 1 & \langle \chi \boldsymbol{v} \rangle &= \boldsymbol{u} \\ \boldsymbol{\nabla}_{\boldsymbol{v}} \chi &= 0 & \frac{\delta}{\delta t} \left(n \langle \chi \rangle \right) &= \frac{\delta n}{\delta t} \end{aligned}$$

$$\frac{\partial n}{\partial t} + \boldsymbol{\nabla} \cdot (n \boldsymbol{u}) = \frac{\delta n}{\delta t} \tag{2.26}$$

Equation (2.26) describes the conservation (or continuity) of particles, relating the change in time to the difference between the flux gradient and the creation and destruction of particles through collisions, these being chiefly chemical reactions.

For a description of the conservation of momentum, one uses the first moment, obtained by equating $\chi = m\boldsymbol{v}$. However, the derivation is easier if one first uses $\chi = mv_x$, as shown in the following equations. This derivation uses the definition of the pressure tensor $\boldsymbol{p}$ [52], as given in (2.27).

$$p_{ij} = nm \langle w_i w_j \rangle \tag{2.27}$$

This is commonly separated into a scalar pressure $p = \frac{1}{3} nm \langle w^2 \rangle = n k_B T$ and a stress tensor $\boldsymbol{\pi}$, as shown in (2.28), where $\boldsymbol{I}$ is the identity matrix, and δ_{kl} is the Dirac delta function.

$$\boldsymbol{p} = p\boldsymbol{I} + \boldsymbol{\pi} \tag{2.28}$$

$$\pi_{kl} = nm \left\langle w_k w_l - \tfrac{1}{3} w^2 \delta_{kl} \right\rangle \tag{2.29}$$

For the first term in (2.25), $\langle \chi \rangle = mu_x$. By substituting in (2.26), one arrives at

the expression below:

$$\begin{aligned}\frac{\partial}{\partial t}\left(mnu_x\right) &= mn\frac{\partial u_x}{\partial t} + mu_x\frac{\partial n}{\partial t} \\ &= mn\frac{\partial u_x}{\partial t} - mu_x\sum_i \frac{\partial}{\partial r_i}\left(nu_i\right) + mu_x\frac{\delta n}{\delta t}\end{aligned}$$

For the second term of (2.25), $\langle\chi\boldsymbol{v}\rangle = m\langle v_x\boldsymbol{v}\rangle$ can be expressed using the pressure tensor as given in (2.27) and (2.28). By again splitting $\boldsymbol{v}$ into directional components:

$$\begin{aligned}\langle mv_xv_i\rangle &= m\left\langle\left(u_x+w_x\right)\left(u_i+w_i\right)\right\rangle \\ &= mu_xu_i + m\left\langle w_xw_i\right\rangle + mu_x\left\langle w_i\right\rangle + m\left\langle w_x\right\rangle u_i \\ &= mu_xu_i + m\left\langle w_xw_i\right\rangle \\ &= mu_xu_i + \frac{p_{xi}}{n}\end{aligned}$$

By summing equations for each dimension i, one obtains an expression for the second term of (2.25), where the pressure tensor has been split through the use of (2.28).

$$\boldsymbol{\nabla}\cdot\left(n\left\langle\chi\boldsymbol{v}\right\rangle\right) = m\sum_i\frac{\partial}{\partial r_i}\left(nu_xu_i\right) + \frac{\partial p}{\partial r_x} + \sum_i\frac{\partial\pi_{x,i}}{\partial r_x} \tag{2.30}$$

For the third term of (2.25), $\boldsymbol{\nabla}_{\boldsymbol{v}}\chi = m\hat{x}$, so that the acceleration term becomes simply $mn\left\langle a_x\right\rangle$. The collision term is also reasonably simple at this stage, with the result for the first term being used to give the expression below:

$$\frac{\delta}{\delta t}\left(n\left\langle\chi\right\rangle\right) = m\frac{\delta}{\delta t}\left(nu_x\right)$$

Through collection of terms, one arrives at an expression for one of the coordinates of momentum.

$$mn\frac{\partial u_x}{\partial t} + mn\sum_i u_i\frac{\partial u_x}{\partial r_i} + \frac{\partial p}{\partial r_x} + \sum_i\frac{\partial\pi_{xi}}{\partial r_x} + mn\left\langle a_x\right\rangle = m\frac{\delta\left(nu_x\right)}{\delta t} - mu_x\frac{\delta n}{\delta t} \tag{2.31}$$

The coordinate x can be replaced with either of the other Cartesian components to obtain a set of three equations that can be combined into a single vector expression, given in (2.32), where $m\boldsymbol{a}$ has been replaced with the Lorentz force, and Ze is the charge on each particle.

$$mn\left[\frac{\partial\boldsymbol{u}}{\partial t} + \left(\boldsymbol{u}\cdot\boldsymbol{\nabla}\right)\boldsymbol{u}\right] + \boldsymbol{\nabla}p + \boldsymbol{\nabla}\boldsymbol{\pi} - nZe\left[\boldsymbol{E}+\boldsymbol{v}\times\boldsymbol{B}\right] = m\frac{\delta\left(n\boldsymbol{u}\right)}{\delta t} - m\boldsymbol{u}\frac{\delta n}{\delta t} \tag{2.32}$$

An expression that describes the conservation of energy can be found by using $\chi = mv^2/2$ to obtain the second moment of the Boltzmann Equation. Naturally, due to the addition of another power of $\boldsymbol{v}$, the derivation is more complicated than that of the first moment. The following definitions are used in the derivation [52], where $\langle K \rangle$ is the expectation value of total kinetic energy for particles, comprised of the directional kinetic energy K_f and that from thermal motion K_T. $\boldsymbol{Q}$ is the total energy flux carried by all particles, encompassing the heat flux density $\boldsymbol{q}$ due to random motion, and considerations for energy transport due to directed motion.

$$\begin{aligned}
\langle K \rangle &= \left\langle \frac{mv^2}{2} \right\rangle \\
&= \frac{mu^2}{2} + \left\langle \frac{mw^2}{2} \right\rangle \\
&= K_f + K_T
\end{aligned}$$

$$\begin{aligned}
\boldsymbol{Q} &= \tfrac{1}{2} nm \left\langle \boldsymbol{v} v^2 \right\rangle \\
&= \boldsymbol{q} + nK_f \boldsymbol{u} + nK_T \boldsymbol{u} + \boldsymbol{p}\boldsymbol{u}
\end{aligned}$$

$$\boldsymbol{q} = \frac{nm}{2} \left\langle \boldsymbol{w} w^2 \right\rangle$$

For the terms of the general transport equation:

$$\begin{aligned}
\langle \chi \rangle &= \left\langle \frac{mv^2}{2} \right\rangle \\
&= \langle K \rangle
\end{aligned}$$

$$\begin{aligned}
\langle \chi \boldsymbol{v} \rangle &= \left\langle \frac{\boldsymbol{v} m v^2}{2} \right\rangle \\
&= \frac{\boldsymbol{Q}}{n}
\end{aligned}$$

$$\begin{aligned}
\boldsymbol{\nabla}_{\boldsymbol{v}} \chi &= \boldsymbol{\nabla}_{\boldsymbol{v}} \left(\frac{mv^2}{2} \right) \\
&= m\boldsymbol{v}
\end{aligned}$$

$$\therefore \langle \boldsymbol{a} \cdot \boldsymbol{\nabla}_{\boldsymbol{v}} \chi \rangle = \langle \boldsymbol{F} \cdot \boldsymbol{v} \rangle$$

Substituting these into (2.25) and again using the Lorentz Force, one arrives at

(2.33), where the magnetic field term vanishes due to the vector identity $(\boldsymbol{a} \times \boldsymbol{b}) \cdot \boldsymbol{a} = 0$.

$$\frac{\partial}{\partial t}\left(n\left\langle K\right\rangle\right) + \boldsymbol{\nabla} \cdot \boldsymbol{Q} - nZe\boldsymbol{u} \cdot \boldsymbol{E} = \frac{\delta}{\delta t}\left(n\left\langle K\right\rangle\right) \tag{2.33}$$

The first two terms of (2.33) will be expanded below, using the definitions given above, and (2.26) and (2.32) for the expansion of $\partial n/\partial t$ and $\partial \boldsymbol{u}/\partial t$ respectively.

$$\frac{\partial\left(n\left\langle K\right\rangle\right)}{\partial t} = mn\boldsymbol{u}\frac{\partial \boldsymbol{u}}{\partial t} + \frac{3}{2}k_B n\frac{\partial T}{\partial t} + \left(\frac{1}{2}mu^2 + \frac{3}{2}k_B T\right)\frac{\partial n}{\partial t} \tag{2.34a}$$

$$\begin{aligned} mn\boldsymbol{u}\frac{\partial \boldsymbol{u}}{\partial t} &= nZe\boldsymbol{u} \cdot \boldsymbol{E} - \boldsymbol{u} \cdot \boldsymbol{\nabla} p - \boldsymbol{u} \cdot \boldsymbol{\nabla}\boldsymbol{\pi} - mnu^2\boldsymbol{\nabla} \cdot \boldsymbol{u} \\ &\quad + m\boldsymbol{u} \cdot \frac{\delta\left(n\boldsymbol{u}\right)}{\delta t} - mu^2\frac{\delta n}{\delta t} \end{aligned} \tag{2.34b}$$

$$\begin{aligned} \left(\frac{1}{2}mu^2 + \frac{3}{2}k_B T\right)\frac{\partial n}{\partial t} &= -\tfrac{1}{2}mu^2 n\boldsymbol{\nabla} \cdot \boldsymbol{u} - \tfrac{1}{2}mu^2\boldsymbol{u} \cdot \boldsymbol{\nabla} n - \tfrac{3}{2}k_B T n\boldsymbol{\nabla} \cdot \boldsymbol{u} \\ &\quad - \tfrac{3}{2}k_B T\boldsymbol{u} \cdot \boldsymbol{\nabla} n + \left(\frac{1}{2}mu^2 + \frac{3}{2}k_B T\right)\frac{\delta n}{\delta t} \end{aligned} \tag{2.34c}$$

$$\begin{aligned} \boldsymbol{\nabla} \cdot \boldsymbol{Q} &= \boldsymbol{\nabla} \cdot \boldsymbol{q} + \boldsymbol{\nabla}\left(n\boldsymbol{u}\tfrac{1}{2}mu^2\right) + \boldsymbol{\nabla}\left(n\boldsymbol{u}\tfrac{3}{2}k_B T\right) \\ &\quad + \boldsymbol{\nabla}\left(p\boldsymbol{u}\right) + \boldsymbol{\nabla}\left(\boldsymbol{\pi}\boldsymbol{u}\right) \end{aligned} \tag{2.35a}$$

$$\boldsymbol{\nabla}\left(n\boldsymbol{u}\tfrac{1}{2}mu^2\right) = mnu^2\boldsymbol{\nabla} \cdot \boldsymbol{u} + \tfrac{1}{2}mnu^2\boldsymbol{\nabla} \cdot \boldsymbol{u} + \tfrac{1}{2}mu^2\boldsymbol{u} \cdot \boldsymbol{\nabla} n \tag{2.35b}$$

$$\boldsymbol{\nabla}\left(n\boldsymbol{u}\tfrac{3}{2}k_B T\right) = \tfrac{3}{2}k_B n\boldsymbol{u} \cdot \boldsymbol{\nabla} T + \tfrac{3}{2}k_B nT\boldsymbol{\nabla} \cdot \boldsymbol{u} + \tfrac{3}{2}k_B T\boldsymbol{u} \cdot \boldsymbol{\nabla} n \tag{2.35c}$$

$$\boldsymbol{\nabla}\left(p\boldsymbol{u}\right) = p\boldsymbol{\nabla} \cdot \boldsymbol{u} + \boldsymbol{u} \cdot \boldsymbol{\nabla} p \tag{2.35d}$$

$$\boldsymbol{\nabla}\left(\boldsymbol{\pi}\boldsymbol{u}\right) = \boldsymbol{\pi}\boldsymbol{\nabla} \cdot \boldsymbol{u} + \boldsymbol{u} \cdot \boldsymbol{\nabla}\boldsymbol{\pi} \tag{2.35e}$$

Fortunately, a large number of terms within (2.34) and (2.35) either cancel or combine, so that upon substitution one is left with only eight terms in the general second moment, as given in (2.36). This equation describes the transport of energy in the system, treating the directional and thermal motion separately, and accounting for anisotropies in the distribution function over random velocities through the viscous stress tensor, $\boldsymbol{\pi}$.

$$\begin{aligned} &\tfrac{3}{2}k_B n\frac{\partial T}{\partial t} + \tfrac{3}{2}k_B n\boldsymbol{u} \cdot \boldsymbol{\nabla} T + p\boldsymbol{\nabla} \cdot \boldsymbol{u} + \boldsymbol{\pi}\boldsymbol{\nabla} \cdot \boldsymbol{u} + \boldsymbol{\nabla} \cdot \boldsymbol{q} \\ &\quad = \frac{\delta\left(n\left\langle K\right\rangle\right)}{\delta t} - m\boldsymbol{u} \cdot \frac{\delta\left(n\boldsymbol{u}\right)}{\delta t} + \left(\tfrac{1}{2}mu^2 - \tfrac{3}{2}k_B T\right)\frac{\delta n}{\delta t} \end{aligned} \tag{2.36}$$

2.4.4 Collisional Terms

In order to complete the picture of the transport equations, one must consider what happens to the particle density, momentum, and energy upon collisions. One needs to account for changes due to both elastic and inelastic collisions, where appropriate. Interpretations of the effects of collisions can differ and, unlike the moments of the Boltzmann equation given above, there is no single definitive route for their derivation. Thus different authors may use slightly different expressions for the collision operators. The collision terms presented in this work are collated from a number of texts [19, 20, 23, 52] in an attempt to provide a comprehensive description of the effect of elastic collisions on both momentum and energy transfer between species. There are some caveats with the approach presented here, notably in the neglection of charge exchange and super-elastic collisions. The former are neglected as they have no net effect in a 1D system, and the latter as they are not expected to be of significance within the parameter range being investigated. The effect of inelastic collisions are also not included in momentum or energy transfer descriptions below, as the energy transfers that result are considered separately, and their effect on momentum transfer is assumed to be small when compared to the more frequent elastic collisions.

The change in particle density, $\delta n/\delta t$, is the simplest term to derive, as only chemical reactions and electronic excitations/de-excitations can change the number of particles of a particular species. Thus the change in particle density due to collisions can be expressed as given in (2.37), where G_{R_α} denotes whether a particle of type α is created $(+1)$ or destroyed (-1) by the reaction R_α, which has the rate coefficient K_R and collision partners n_{R_1} and n_{R_2}.

$$\frac{\delta n_\alpha}{\delta t} = \sum_{R_\alpha} G_{R_\alpha} n_{R_1} n_{R_2} K_R \tag{2.37}$$

For momentum changes, one must take primarily elastic collisions, also referred to as momentum transfer collisions, into consideration. By considering binary hard sphere collisions between particles of different types, one can derive an expression that gives the change in momentum of a species α due to collisions with a second species β as proportional to the relative drift velocity of the two species. The proportionality constant for this interaction is the collision frequency for the two species, often defined as $\nu_{\alpha\beta} = n_\beta K_{\alpha\beta}$, where $K_{\alpha\beta}$ is the collision rate coefficient [19, 23].

One effect that is often overlooked is that of temperature gradients on energy de-

pendent collision frequencies. For species that have strong thermal gradients (namely electrons), the collision frequency can change considerably on the scale of the average distance between collisions. This results in an anisotropy in the average number of collisions experienced by particles, and so a net change in momentum. The magnitude of this effect can be estimated by considering the change in collision frequency over the mean free path of the particles, resulting in the final term in (2.38), where $T_{\alpha\beta} = (m_\alpha T_\beta + m_\beta T_\alpha) / (m_\alpha + m_\beta)$ [52].

$$\begin{aligned} m_\alpha \frac{\delta (n_\alpha \boldsymbol{u}_\alpha)}{\delta t} = &- \sum_\beta \frac{m_\alpha m_\beta}{m_\alpha + m_\beta} n_\alpha n_\beta K_{\alpha\beta} (\boldsymbol{u}_\alpha - \boldsymbol{u}_\beta) \\ &+ n_\alpha k_B \sum_\beta \frac{T_{\alpha\beta}}{\nu_{\alpha\beta}} \frac{\mathrm{d}\nu_{\alpha\beta}}{\mathrm{d}T_{\alpha\beta}} \boldsymbol{\nabla} T_{\alpha\beta} \end{aligned} \tag{2.38}$$

A similar hard sphere model can be used to find the change in kinetic energy upon collisions [52], given in (2.39).

$$\begin{aligned} \frac{\delta (n \langle K \rangle)}{\delta t} = &- \sum_\beta 3 \frac{m_\alpha m_\beta}{(m_\alpha + m_\beta)^2} n_\alpha n_\beta K_{\alpha\beta} k_B (T_\alpha - T_\beta) \\ &- \sum_\beta \frac{m_\alpha m_\beta}{(m_\alpha + m_\beta)^2} n_\alpha n_\beta K_{\alpha\beta} \left[m_\alpha u_\alpha^2 - m_\beta u_\beta^2 \right. \\ &\left. + (m_\beta - m_\alpha) \boldsymbol{u}_\alpha \boldsymbol{u}_\beta \right] \end{aligned} \tag{2.39}$$

With these collision terms, the first three moments of the Boltzmann Equation can be fully constructed. With the zeroth (2.40) and first moments (2.41), a simple substitution suffices, but for the group of collision terms in the second moment (2.42), some collection and cancellation of terms occurs.

$$\frac{\partial n_\alpha}{\partial t} + \boldsymbol{\nabla} \cdot (n_\alpha \boldsymbol{u}_\alpha) = \sum_{R_\alpha} G_{R_\alpha} n_{R_1} n_{R_2} K_R \tag{2.40}$$

$$\begin{aligned} &m_\alpha n_\alpha \left[\frac{\partial \boldsymbol{u}_\alpha}{\partial t} + (\boldsymbol{u}_\alpha \cdot \boldsymbol{\nabla}) \boldsymbol{u}_\alpha \right] + \boldsymbol{\nabla} p_\alpha + \boldsymbol{\nabla} \boldsymbol{\pi}_\alpha - n_\alpha Z_\alpha e [\boldsymbol{E} + \boldsymbol{v}_\alpha \times \boldsymbol{B}] \\ &= - \sum_\beta \frac{m_\alpha m_\beta}{m_\alpha + m_\beta} n_\alpha n_\beta K_{\alpha\beta} (\boldsymbol{u}_\alpha - \boldsymbol{u}_\beta) + n_\alpha k_B \sum_\beta \frac{T_{\alpha\beta}}{\nu_{\alpha\beta}} \frac{\mathrm{d}\nu_{\alpha\beta}}{\mathrm{d}T_{\alpha\beta}} \boldsymbol{\nabla} T_{\alpha\beta} \\ &\quad - m_\alpha \boldsymbol{u}_\alpha \sum_{R_\alpha} G_{R_\alpha} n_{R_1} n_{R_2} K_R \end{aligned} \tag{2.41}$$

$$\begin{aligned}
&\tfrac{3}{2}k_B n_\alpha \frac{\partial T_\alpha}{\partial t} + \tfrac{3}{2}k_B n_\alpha \boldsymbol{u}_\alpha \cdot \boldsymbol{\nabla} T_\alpha + p_\alpha \boldsymbol{\nabla}\cdot\boldsymbol{u}_\alpha + \boldsymbol{\pi}_\alpha \boldsymbol{\nabla}\cdot\boldsymbol{u}_\alpha + \boldsymbol{\nabla}\cdot\boldsymbol{q}_\alpha \\
&\quad = -\sum_\beta 3\frac{m_\alpha m_\beta}{(m_\alpha+m_\beta)^2} n_\alpha n_\beta K_{\alpha\beta} k_B (T_\alpha - T_\beta) \\
&\qquad + \left(\tfrac{1}{2}m_\alpha u_\alpha^2 - \tfrac{3}{2}k_B T_\alpha\right) \sum_{R_\alpha} G_{R_\alpha} n_{R_1} n_{R_2} K_R \\
&\qquad + \sum_\beta \frac{m_\alpha m_\beta^2}{(m_\alpha+m_\beta)^2} n_\alpha n_\beta K_{\alpha\beta} (\boldsymbol{u}_\alpha - \boldsymbol{u}_\beta)^2 \\
&\qquad - n_\alpha \boldsymbol{u}_\alpha k_B \sum_\beta \frac{T_{\alpha\beta}}{\nu_{\alpha\beta}} \frac{\mathrm{d}\nu_{\alpha\beta}}{\mathrm{d}T_{\alpha\beta}} \boldsymbol{\nabla} T_{\alpha\beta}
\end{aligned} \tag{2.42}$$

2.4.5 Closure Terms

The three equations (2.40) to (2.42) fully describe the transport of their respective properties. However in each expression is a reference to the next higher moment, meaning that one will always have more variables than equations, and thus an unsolvable system, unless one makes assumptions to close the equation set. For species that are largely isothermal, a common assumption is $\boldsymbol{\nabla} T_\alpha = 0$. This truncates the series of moments at the first, leaving just two equations. However if this is not suitable, then an expression must be found for the heat flux, $\boldsymbol{q}_\alpha$. If a species has a high enough density that one can assume that most collisions will be with itself, then Fourier's Law of thermal conductivity is applicable (2.43), where $h_\alpha = h_a T_\alpha + h_b$ is the thermal conductivity of the species. If, however, most collisions occur with another species, then a different formulation must be used, such as the weakly ionised approximation for electron heat flux (2.44) [52], where the species α is assumed to collide only with the species β.

$$\boldsymbol{q}_\alpha = -h_\alpha \boldsymbol{\nabla} T_\alpha \tag{2.43}$$

$$\boldsymbol{q}_\alpha = -\left(\frac{5}{2} - \frac{T_{\alpha\beta}}{\nu_{\alpha\beta}}\frac{\mathrm{d}\nu_{\alpha\beta}}{\mathrm{d}T_{\alpha\beta}}\right) k_B^2 \frac{n_\alpha T_\alpha}{m_\alpha \nu_{\alpha\beta}} \boldsymbol{\nabla} T_\alpha - n_\alpha k_B T_\alpha \boldsymbol{u}_\alpha \frac{T_{\alpha\beta}}{\nu_{\alpha\beta}} \frac{\mathrm{d}\nu_{\alpha\beta}}{\mathrm{d}T_{\alpha\beta}} \tag{2.44}$$

2.5 Numerical Solution Methods

The expressions that result from the Boltzmann equation and the moments are highly nonlinear and strongly coupled between species. This makes finding an analytical solution impractical, if not impossible. Thus one must resort to numerical methods for approximating solutions. As the equations are differential, it is numerical integration methods that are used to solve them. This section details some of the families of numerical integrators available and some of their benefits and weaknesses.

In general, systems of differential equations can have an infinite number of solutions. Particular solutions are obtained by specifying values of variables so as to constrain the possible solutions. For a simple differential equation such as $y' = f(x, y)$, where f is an arbitrary function of the dependent variable y and the independent variable x, one can specify a condition on either y or y' at any value of x. Systems of differential equations and their constraints can be grouped into two types of 'problems'. Those with constraints at only one value of the independent variable are fully specified at that point, and are referred to as initial value problems (IVPs), as numerical integration starts at a single position with the specified initial values, and progresses from there. Boundary value problems (BVPs) are those with conditions at two or more positions, as the integration must take place between these values of x, known as the 'boundaries' of the integration.

Solution methods for IVPs compared with BVPs differ greatly in their construction, behaviour, capabilities and applications. IVP solution methods typically involve evaluating y' at a specific point, then using this gradient to estimate the value of y after a small step in x. In order to solve a BVP one typically breaks up, or *discretises*, the range of x between the boundary locations. Starting from an initial estimate, that value of y at each point is updated using estimations built from the surrounding points and an approximation of the derivatives. This process is continued until some condition is met, usually some sort of convergence tolerance, such as specifying that the change in y between each iteration must be below a certain value. This sort of solution method is well suited to 'large' problems; those with a variety of different physics phenomena or a complicated region of space and time over which the integration is to be performed. However the computation time required to perform all of the iterations necessary is significant, and often calls for the use of large scale computers. Due to one of the motivations for this work being the quick solution time and accessibility of the model, the methods for solving BVPs are unsuitable, and so the focus will be on creating and solving an IVP.

Similar to the discretisation used for BVPs, a numerical integration of an IVP is typically computed at distinct points. Starting from the initial condition at $x_0 = a$, successive points are defined by $x_{n+1} = x_n + h$, where h is a step length. For the following descriptions h is constant for all x, but in general this need not be the case. From the Taylor expansion of $y(x_{n+1}) = y(x_n + h)$ for small h about the point x_n, one can truncate terms to arrive at an approximation for $y(x_{n+1})$ in terms of the

differential expression $f(x, y)$.

$$y(x_n + h) = y(x_n) + hy'(x_n) + \tfrac{1}{2}h^2 y''(x_n) + \mathcal{O}(h^3) \tag{2.45}$$

$$y(x_n + h) \approx y(x_n) + hf(x_n, y_n) \tag{2.46}$$

The approximation in (2.46) is referred to as *Euler's Method*, and is the simplest numerical integration method in a family of schemes known as linear multistep methods. These methods are suitable for use in solving not just single differential equations, such as $y' = f(x, y)$, but also any system of differential equations that can be expressed in the form of (2.47), where $\boldsymbol{\eta}$ are the initial conditions at the point $x = a$ for each of the variables contained in the vector $\boldsymbol{y}$. Systems containing higher than first order differentials of $\boldsymbol{y}$ can be reduced to the form of (2.47) through the introduction of additional variables.

$$\boldsymbol{y}' = \boldsymbol{f}(x, \boldsymbol{y}), \quad \boldsymbol{y}(a) = \boldsymbol{\eta} \tag{2.47}$$

The solution to such a system is, as mentioned above, found for a series of discrete points $\boldsymbol{y}_n = \boldsymbol{y}(x_n)$. A linear multistep method is defined as having a linear relationship for determining the sequence $\{\boldsymbol{y}_n\}$ and can be given generally as (2.48) [53], where k is the step number of the method, and α_j, β_j are constants.

$$\sum_{j=0}^{k} \alpha_j y_{n+j} = h \sum_{j=0}^{k} \beta_j f_{n+j} \tag{2.48}$$

Methods for determining the coefficients α_j, β_j vary. They can be found through Taylor expansion and subsequent truncation as for (2.46), numerical integration, or interpolation. If the coefficient $\beta_k \neq 0$, then the expression for y_{n+k} is self dependent, and the method is denoted implicit, otherwise y_{n+k} is given directly and the method is explicit. Explicit methods are simpler to implement, but implicit methods can be made more accurate, and tend to be more numerically stable than explicit methods of the same step number [54]. However, through the self dependence, implicit methods require the iterative solution of a nonlinear equation at each point.

One can combine implicit and explicit methods into a single method by first computing the predictor $\hat{\boldsymbol{y}}_{n+k}$ using an explicit method. The function $\hat{\boldsymbol{f}}(x_{n+k}, \hat{\boldsymbol{y}}_{n+k})$ is then calculated and used in the application of an implicit method to 'correct' the first estimation. These are called predictor-corrector methods, and their most common implementation is Predict-Evaluate-Correct-Evaluate (PECE).

Through integration of a polynomial of degree k fitted to the previous k points, one obtains a linear expression for y_{n+k} in terms of y_{n+k-1} and $f_n, ..., f_{n+k-1}$, which is an explicit method. If one includes the point y_{n+k} in the polynomial and performs the same manipulation, then an implicit expression in terms of y_{n+k-1} and $f_n, ..., f_{n+k}$ is produced [53]. The family of numerical integration methods created through this process are called Adams methods, with the explicit and implicit forms known as Adams-Bashforth and Adams-Moulton respectively. The common procedure of using Adams methods for both the predictor and corrector in a PECE scheme creates what is referred to as an Adams-Bashforth-Moulton method [55].

2.6 Early 1-D Time Averaged Fluid Models

The concept of describing a plasma as a combination of interacting fluids is not a new one, and can be traced back to the earliest models of plasmas. Descriptions of the behaviour of charged species using ensemble values, as opposed to a particulate picture, were performed in the 1920's for collisional [56, 57] and collisionless [58] cases. The application of this concept to plasmas containing negative ions was performed reasonably soon afterward [59], with a note that the Schottky model fitted surprisingly well to diatomic gases. The work was revisited over the years, with attempts to describe the three component plasma using diffusion transport coefficients [60–62], However to develop these models, assumptions such as constant α must be made, which has since been found to be debatable.

Advances were also made in the investigation of electropositive plasmas, where it was shown to be possible to provide an analytic solution for the intermediate pressure regime [63]. It was also described how the assumptions of quasineutrality [64] or isothermal electrons [65] can be dropped in a two component plasma, through the use of other approximations and numerical integration.

2.6.1 Previous Electronegative Models

A model was created in 1980 that describes the radial profiles of charged species in a positive column created in an electronegative gas without simplifying to transport coefficients [66]. The momentum equation was developed for electrons, positive, and negative ions under the assumptions of axial uniformity, isothermality (and therefore constant reaction rates), and a Boltzmann equilibrium for the electrons. Along with Poisson's equation, the equations were integrated between a symmetry condition at the

centre to a boundary with a perfectly insulating wall [64]. With the consideration that negative ions are confined almost exclusively to the volume, an edge boundary condition was specified for the negative ions stating that the integrated volume production and loss rates must be equal, which can be alternatively stated as a requirement for the negative ion flux at the wall to be zero. This boundary condition was realised by adjusting the central value of the negative ion density until the condition on the flux was met to a given tolerance.

The authors provided a physical justification for the observed negative ion flux, in that the electric field required to equalise the electron and ion currents is of sufficient strength, due to the high temperature of the electrons, that the force on the cold negative ions is large enough to overcome their diffusion. It was further found that the central negative ion density is not directly controlled by the rates of electron attachment/detachment, but instead is always large enough to provide a negative flux near the origin. Along with this new insight into confinement of the negative ions, evidence was seen of a stratification of the discharge into an electronegative core with an electropositive edge, a feature now known to be characteristic of a wide variety of electronegative plasmas [67–69].

This work was used a few times, notably to show that in plasmas with high electronegativity the electron density profile becomes flat as the system moves toward an ion-ion plasma in the central region [70]. It was also used in an attempt to recreate the charged species density profiles using measurements of E/N in an SF_6 discharge [71].

The first significant extension of this work came about in 1988 through the assumption of quasineutrality and high pressure [72], which allowed the analytic investigation to be extended before resorting to numerical integration. These two assumptions allowed the edge boundary condition to be simplified to $n_e(L) = 0$ and provided an analytical expression for α_0 dependent on the ion mobilities and the rates of ionisation, electron detachment, and electron attachment, when these quantities are assumed to be spatially uniform. It was also determined that, when posed in a dimensionless form, the system of equations generated another eigenvalue, referred to in this and later work as λ, that related the reduced electric field (E/N) to the product of gas density and discharge size (NL). This is analogous to the well known relationship between electron temperature and pressure-length product that arises from a simplified treatment of an electropositive plasma. This parameter λ is also a function of the same parameters as α, but not an analytic one. The rates and mobilities can be collected into just two

dimensionless parameters, denoted as P and Q in this work and across the literature, which are measures of the electron attachment and detachment rates respectively.

The authors applied their model to oxygen, taking into consideration reactions involving $O_2\left(^1\Delta_g\right)$ and atomic O. Using experimentally determined densities of the excited and atomic species, and literature estimates of reaction rate coefficients, they calculated the resulting E/N as a function of NL. When compared with experimental data, the results give a favourable qualitative agreement, but overestimate E/N by approximately 50 % across the range investigated.

After this point in time, a much greater rate of investigation is seen, arguably lead by the work of one group [73–76]. Their work made significant analytical advances on the earlier models, and performed investigations across a broad range of parameter space. At the same time, parallel progress was being made in the understanding of electronegative plasmas through other means, such as kinetic (global) models [77], investigation of the sheath boundary [29], and the development of more detailed, computationally intensive fluid models [78].

Of the works submitted in those few years, the most relevant are the descriptions of the system at 'moderate' pressures, where ion inertia is not important, but neither are three body collisions [74, 76]. The two models developed in this regime differ in their dominant reaction mechanisms, and have markedly different behaviours. In the situation where $P, Q < 1$, meaning that the rates of electron attachment and detachment are similar, but ionisation is dominant over both of them, it was found, perhaps counterintuitively, that electronegativity is inversely relational to P. Furthermore, both species of ions are confined to a strongly electronegative 'core', while the electrons are largely unaffected by changes in P [74]. From a more practical standpoint, it was also found that the system was highly sensitive to initial conditions. The authors worked around this using their rigid boundary conditions and a restructuring of the equation system to perform their integration from the wall to the centre, but even then numerical root finding was required.

In the second collisional model, ion-ion and electron-ion recombination are included as additional destruction mechanisms. The resulting equations are greatly restricted in their possible parameter range, hinting perhaps at the potential for instabilities induced by the non-linearities of charged particle recombination. An investigation of strongly electronegative scenarios, with $\alpha \geq 10$, was performed. It was found that the plasma is necessarily structured as before, with an electronegative core, but that the

transition between the two regions is sudden, and its relative position in the discharge is directly controlled by P [76]. It is also postulated that systems containing negative ions cannot have electron-ion recombination without ion-ion recombination, although the model does not include electron detachment destruction of negative ions, so the effect of this additional destruction mechanism is unclear.

After this work was performed, the investigation of electronegative plasmas proceeded in largely different directions, as experimental techniques were developed [4, 79–81] and computational resources improved [82–84]. There was also an increase in the use of 'global' modelling to investigate systems with large numbers of reactions [85, 86], as their relatively simple numerics lend themselves well to the investigation of the complexities of molecular electronegative discharges.

There was still, however, some interest in increasing the analytical insight into electronegative plasmas, particularly in the low pressure environment [87–90]. This work culminated in a number of 'review' style publications [67–69, 91] that attempted to summarise the understanding gained by the community since the first influential fluid model in 1980. Although some analytical type work has been performed since then [92–94], the majority of modelling investigations have proceeded with relatively large, computationally intensive codes, that are admittedly highly accurate, or on global models for chemical kinetics.

Of the models that are similar in capabilities and methodologies to that developed in this work, a comparison of the key features is given in table 1.

2.6.2 Derivation of Simple 1-D Time averaged Models

If one is to fully understand the development of a new fluid model, it is useful to have a background knowledge of simple fluid models. The principles of equation development are similar, and so are some of the issues that arise.

Ambipolar Diffusion

One of the earliest fluid type models can be attributed to Schottky [56], who created a description now referred to as ambipolar diffusion. This theory considers the steady state of a one dimensional, two component plasma amongst a static background of neutral particles in a high pressure regime, where the mean free path of the ions is significantly less than the dimensions of the system. Thus the motion of ions (and electrons) across the plasma is dominated by collisions with the neutral species, and

Table 1: Comparison of previous models of electronegative plasmas of the semi-analytical type.

Concept	Hurlbatt	Edgerly & v. Engel [66]	Ferreria *et al* [72]	Daniels *et al* [74]	Franklin *et al* [76]	Lichtenberg *et al* [87]
Geometry	Planar	Cylindrical	Cylindrical	Cylindrical	Cylindrical	Planar
Driving voltage	RF	DC	DC	DC	DC	RF
Species	4	3	3	3	3	3
Reactions	10	3	5	3	4	3
Dominant Destruction	Detach/Recom	Detach	Detach	Detach	Recom	Recom
Electron Profiles	Self Consistent	Boltzmann	Self Consistent	Self Consistent	Self Consistent	Boltzmann
Negative Ion Profiles	Self Consistent	Self Consistent	Self Consistent	Self Consistent	Self Consistent	Boltzmann
Ion Temperatures	Uniform	Zero	Uniform	Uniform	Uniform	Uniform
Electron Temperatures	Self Consistent	Uniform	Uniform	Uniform	Uniform	Uniform
Reaction Rates	$f(T_e, T_g)$	Uniform	Uniform	Uniform	Uniform	Arrhenius
Elastic Collisions	Explicit	Explicit	Drift/Diffusion	Drift/Diffusion	Drift/Diffusion	Drift/Diffusion
Inelastic Collisions	8	No	No	No	No	1
Collisionality	Medium/High	Low/Medium	High	High	High	Medium/High
Central Boundary	Symmetry	Symmetry	Symmetry	Symmetry	Symmetry	Symmetry
Edge Boundary	Sheath	Insulating Wall	Sheath	Sheath	Sheath	Sheath
Electric Field	Quasineutrality	Poisson's Eq.	Quasineutrality	Quasineutrality	Quasineutrality	Quasineutrality
Neutrals	Self consistent	Background	Background	Background	Background	Background
Method[1]	SI + NR	TE + SI + NR	BVP	SI + NR or AA	SI + NR or AA	AA + I

[1] SI = Spatial Integration, NR = Numerical Root Finding, TE = Taylor Expansions, AA = Analytic Approximations, BVP = Boundary Value Solver, I = Other Iteration

other elastic collisions are neglected. Other approximations are that viscosity effects can be neglected, there is no magnetic field, and there is only one type of chemical reaction: ionisation. The equations are closed by assuming that both ions and electrons are isothermal, with $T_i = 300\,\mathrm{K}$ and T_e to be determined.

By applying the above assumptions to (2.40) and (2.41), and considering quasineutrality ($n_e \approx n_i = n$), an ideal gas equation of state ($p = nk_BT$) for both species, and a zero net current ($n_i\boldsymbol{u}_i = n_e\boldsymbol{u}_e = nu$), one arrives at a set of three equations describing three quantities. The particle continuity expressions for both species are identical, and given in (2.49), where K_I is the reaction rate coefficient for the ionisation process, and the momentum conservation of ion and electrons is described by (2.50) and (2.51) respectively [20].

$$(nu)' = nn_gK_I \tag{2.49}$$

$$k_BT_in' - neE = -m_inu\nu_{ig} \tag{2.50}$$

$$k_BT_en' + neE = -m_enu\nu_{eg} \tag{2.51}$$

In order to extract further insight from (2.50) and (2.51) before solution, they are often rearranged into the forms of (2.52) and (2.53), where two new quantities are introduced. The diffusion coefficient, $D_\alpha = k_BT_\alpha/m_\alpha\nu_{\alpha g}$ describes the motion from thermal diffusion alone, and the mobility $\mu_\alpha = e/m_\alpha\nu_{\alpha g}$ is a measure of the collision limited motion due to electric fields [19].

$$nu = n\mu_iE - D_in' \tag{2.52}$$

$$nu = -n\mu_eE - D_en' \tag{2.53}$$

Through the combination of (2.52) and (2.53), one obtains an expression for the necessary electric field that maintains quasineutrality despite the differing diffusion properties of the ions and electrons.

$$E = -\frac{D_e - D_i}{\mu_e + \mu_i}\frac{n'}{n} \tag{2.54}$$

Substitution of this ambipolar electric field into (2.52) or (2.53) allows the retrieval of a single diffusion parameter, the ambipolar diffusion coefficient, given below.

$$D_a = \frac{\mu_iD_e + \mu_eD_i}{\mu_i + \mu_e} \tag{2.55}$$

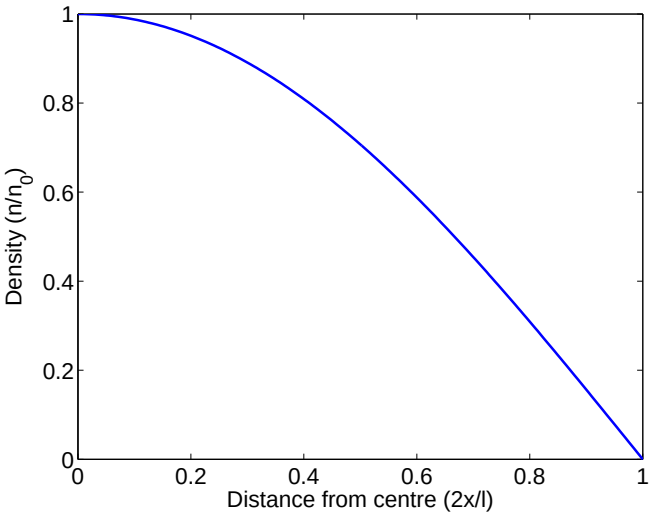

Figure 5: Normalised density profile of both electrons and positive ions in a simple two fluid ambipolar diffusion model.

Subsequently, (2.52) or (2.53) can be written as (2.56), which combined with (2.49), gives a simple linear second order differential equation for the plasma density, given in (2.57)

$$nu = -D_a n' \tag{2.56}$$

$$n'' = -\frac{n_g K_I}{D_a} n \tag{2.57}$$

For a plasma contained between two planar electrodes at $x = \pm l/2$, and by setting boundary conditions as $n(0) = n_0$ and $n(l/2) = 0$, a symmetric solution to (2.57) is obtained, given below.

$$n(x) = n_0 \cos\left[\left(\frac{n_g K_I}{D_a}\right)^{\frac{1}{2}} x\right] \tag{2.58}$$

The boundary conditions specify that $(n_g K_I / D_a)^{1/2} = \pi/l$, if the sheath region is neglected that would exist between the plasma at the wall. This means that (2.58) is not only an expression for the spatial profile of the plasma density that shows independence on all other plasma parameters, but one can also obtain the electron temperature through its control of K_I and D_a.

As the only remaining variable in (2.58) is the central density, it is a simple matter to normalise to the value at the centre, and thus plot a profile of how the plasma density varies from the centre to the edge of the discharge, as shown in figure 5.

As one might expect, the strict restrictions placed upon the ambipolar model mean

that its applicability and accuracy are limited. A zero plasma density at the edge of the system causes singularities in both the particle velocity and the ambipolar electric field, showing that the boundary conditions necessary to achieve an analytic solution are not self consistent. Furthermore, the single reaction considered is a gross oversimplification as even in the simplest of cases, such as a plasma in a mono-atomic gas like Helium or Argon, there are a myriad of processes that need to be considered in order to fully describe the system [95, 96]. However, if the assumptions made were to be relaxed, then attempts to obtain an analytic solution become increasingly more complicated, and quickly reach intractability [97–99], and so numerical treatments are required.

Introduction of negative ions

Plasmas have found a great deal of use in industrial applications due to their unique chemical environment, and in particular plasma etch processes underlie some of the largest international manufacturing industries. Many of the processes call for the use of substances with a certain degree of electron affinity, leading to the formation of significant numbers of negative ions, and the creation of 'electronegative' plasmas. Densities of negative ions can be expressed through a measure of the electronegativity, α, taken as the ratio of negative ion to electron densities. This value can range from less than one in low power discharges in weakly electronegative gases [9] up to $\approx 10^4$ under certain conditions [100]. The presence of these negative ions has a dramatic effect on the plasma by introducing strong non-linearities into describing equations, which manifest in physical systems as temporal instabilities, complex spatial structures involving non-monotonic electric potentials, and coupling of previously independent plasma parameters.

By making assumptions comparable to those used in the model previously described, it is possible to produce a set of equations similar to those used to create the ambipolar diffusion expressions. One major difference is that the quasineutrality conditions becomes $n_i = n_n + n_e$, and so the positive ion and electron densities are no longer interchangeable. Thus the momentum conservation expressions for the positive ions, negative ions, and electrons become (2.59) to (2.61) respectively.

$$n_i u_i = n_i \mu_i E - D_i {n_i}' \tag{2.59}$$

$$n_n u_n = -n_n \mu_n E - D_n n_n' \tag{2.60}$$

$$n_e u_e = -n_e \mu_e E - D_e n_e' \tag{2.61}$$

Again, using (2.59) to (2.61), quasineutrality, and a zero net current ($n_i \boldsymbol{u}_i = n_n \boldsymbol{u}_n + n_e \boldsymbol{u}_e$), one is able to create an equation for the positive ions that has the same form as (2.56), however the diffusion coefficient that arises is dependent on the densities of negative ions and electrons, so the equation cannot be solved independently as it was previously [101]. In order to approach an analytic solution for this three component plasma, which allows one to gain further insight to the interrelations of the different species and their properties, one must make further assumptions. A common assumption for the negative particles is that they are in thermal equilibrium with a confining electrostatic potential, ϕ, a so called 'Boltzmann equilibrium' (2.62) and (2.63).

$$n_e = n_{e0} \exp\left(\frac{e\phi}{k_B T_e}\right) \tag{2.62}$$

$$n_n = n_{n0} \exp\left(\frac{e\phi}{k_B T_n}\right) \tag{2.63}$$

This assumption implicitly also assumes that drifts are dominated by thermal motion and that the particle energy distribution function can be described by a Maxwellian (2.2). The drift condition may hold for electrons under certain conditions, but is highly questionable for the negative ions. For the assumption of a Maxwellian, this situation is reversed; the heavy negative ions are more likely to be well described by (2.2), whereas the electrons are often highly non-Maxwellian [102]. However, these assumptions allow one to describe the plasma using only three equations, given in (2.64) to (2.66) [20].

$$(n_i u_i)' = n_{e0} n_g K_I \exp\left(\frac{e\phi}{k_B T_e}\right) \tag{2.64}$$

$$-e\phi' = m_i \nu_{ig} u_i \tag{2.65}$$

$$n_i = n_{e0} \exp\left(\frac{e\phi}{k_B T_e}\right) + n_{n0} \exp\left(\frac{e\phi}{k_B T_n}\right) \tag{2.66}$$

Despite the reasonably simple appearance of these equations, they are not able to be integrated analytically, as the coupling between variables is too strong. Approximate analytical solutions to this simple three component plasma have been obtained by constraining the system to regions of parameter space in which some terms can be neglected or cancelled, for example [87], but numerical integration is required to obtain actual solutions to (2.64) to (2.66). Furthermore, solutions require a more rigorous specification of system parameters than in the ambipolar diffusion model presented previously. Solutions are specific to the physical parameters of the discharge chamber,

as well as the process gas in which the plasma is created.

Simple models such as those just described have their use in being able to highlight possible unintuitive behaviour and interplay between the different plasma properties. However, their ability to accurately predict the intricate dynamics and emergent properties of these systems is highly debatable, due to the occasionally very strict assumptions that need to be made in order to reach an actual description of the plasma. The ability to reduce the number of assumptions made while maintaining a system of equations that can be used to understand the links between variables would be valuable. However the likelihood of there existing such expressions that do not require numerical intervention to reach full solutions is low. Additionally, the systems described in the simple models above do not represent any known real plasma; as mentioned previously, even in a mono-atomic gas there are complex processes and multiple excited states that need to be considered to encompass all possible behaviour. The addition of molecular species into a plasma increases this complexity many times over.

In addition, analytical progression from the fluid equations is difficult and time consuming. It is more common to resort to finite element methods because they are much simpler to implement. However as discussed previously, these can take a great deal of computation time to obtain a solution. A system that is able to describe a complex plasma without resorting to a finite element solution would be highly valuable for the flexibility and greatly reduced computational cost that it would provide. The development of such a system is described over the next few chapters, culminating in a model that is able to describe an electronegative plasma with non-uniform electron temperatures including neutral dynamics.

Chapter 3

Modelling an Isothermal Electronegative Plasma

The development of the new semi-analytical model begins in this chapter with the description and demonstration of a model of a three component isothermal plasma. The equilibrium state of the three most important charged species is considered in a constant neutral background, and equations are created to describe the interactions of the three fluids with the neutrals and each other. It is found that numerical solution is not as simple as just performing the integration, and numerical methods are detailed that allow the solution of a wide variety of conditions.

3.1 Equation Development

In order to examine the capabilities of more detailed equations than those described in Section 2.6.2, a model will be constructed to find the equilibrium (or time averaged) state of a three component electronegative plasma existing in a constant neutral background. The species considered are one positive ion (i), one negative ion (n), and electrons (e). It is assumed for this model that the entire plasma bulk is quasineutral, all species are isothermal, and that the neutral density is constant. These assumptions are recognised not to be valid for all conditions, but are appropriate for a system in which the sheaths are small compared with the bulk width, and the ionisation fraction is low. Further assumptions are that viscosity and convective effects are negligible. These two approximations are valid if the thermal part of the velocity distribution is large compared with the directional part and there is no external magnetic field applied [52], both of which are met in the plasma to be modelled.

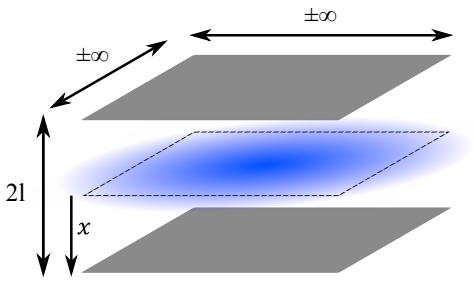

Figure 6: Schematic of the discharge being modelled. x denotes the dimension being analysed.

The physical system to be modelled is a capacitively coupled, RF excited plasma contained between two infinitely planar electrodes, as shown in figure 6. This arrangement simplifies matters by allowing the investigation to take place only along the inter-electrode dimension, while maintaining comparability to real symmetric discharges.

3.1.1 Approximation Application

By applying the isothermal, equilibrium and magnetic field approximations to the Boltzmann moments (2.40) to (2.42), one obtains a slightly simplified system of general equations (3.1) and (3.2), particularly because the energy conservation equation (2.42) is made unnecessary by the isothermal approximation.

$$\boldsymbol{\nabla} \cdot (n_\alpha \boldsymbol{u}_\alpha) = \sum_{R_\alpha} G_{R_\alpha} n_{R_1} n_{R_2} K_R \tag{3.1}$$

$$\begin{aligned} m_\alpha n_\alpha \overbrace{(\boldsymbol{u}_\alpha \cdot \boldsymbol{\nabla})\, \boldsymbol{u}_\alpha}^{\text{convection}} + \boldsymbol{\nabla} p_\alpha + \overbrace{\boldsymbol{\nabla} \boldsymbol{\pi}_\alpha}^{\text{viscosity}} - n_\alpha Z_\alpha e \boldsymbol{E} \\ = -\sum_\beta \frac{m_\alpha m_\beta}{m_\alpha + m_\beta} n_\alpha n_\beta K_{\alpha\beta} (\boldsymbol{u}_\alpha - \boldsymbol{u}_\beta) - m_\alpha \boldsymbol{u}_\alpha \sum_{R_\alpha} G_{R_\alpha} n_{R_1} n_{R_2} K_R \end{aligned} \tag{3.2}$$

Further simplifications are made to (3.2) through the removal of the terms describing the effects of convection and viscosity, as discussed above and indicated in the equation. The pressure gradient is also expanded, using the ideal gas equation of state $p = n k_B T$.

$$\boldsymbol{\nabla} \cdot (n_\alpha \boldsymbol{u}_\alpha) = \sum_{R_\alpha} G_{R_\alpha} n_{R_1} n_{R_2} K_R \tag{3.3}$$

$$\begin{aligned} k_B T_\alpha \boldsymbol{\nabla} n_\alpha = n_\alpha Z_\alpha e \boldsymbol{E} - \sum_\beta \frac{m_\alpha m_\beta}{m_\alpha + m_\beta} n_\alpha n_\beta K_{\alpha\beta} (\boldsymbol{u}_\alpha - \boldsymbol{u}_\beta) \\ - m_\alpha \boldsymbol{u}_\alpha \sum_{R_\alpha} G_{R_\alpha} n_{R_1} n_{R_2} K_R \end{aligned} \tag{3.4}$$

Application of these assumptions leads to (3.3) and (3.4), which describe density and flux gradients for all of the species in the system.

3.1.2 Normalisation Scheme

In order to increase insight, clarify relationships between plasma properties, and expedite the numerical solution of the equations, the system is normalised so as to remove all dimensions. The choice of normalisation scheme is highly influential on the functionality and interpretation of the resulting model. The scheme used, given below, builds on the work of Raimbault and Liard [103, 104] and applies it to an electronegative plasma. In this scheme: n_f is the gas fill density; m_i is the mass of the positive ion; $u_B = (k_B T_e/m_i)^{1/2}$ is the positive ion Bohm velocity; K_0 is a normalisation reaction rate coefficient; and T_e is the electron temperature. As the model is one dimensional, vectors are also converted to scalars in the normalisation.

$$
\begin{aligned}
n_\alpha &= n_f N_\alpha & \boldsymbol{u}_\alpha &= u_B V_\alpha \\
K_R &= K_0 \epsilon_R & m_\alpha &= m_i M_\alpha \\
T_\alpha &= \frac{T_e}{\gamma_\alpha} & x &= \frac{u_B}{n_f K_0} X \\
n_\alpha \boldsymbol{u}_\alpha &= n_f u_B \Gamma_\alpha & \frac{d[Y]}{dx} &= \frac{n_f K_0}{u_B} [Y]'
\end{aligned}
$$

It is interesting to note that the total system size is not included in the normalisation scheme. As an effect of this, there is a coupling of the pressure and system length, as is known to happen in physical systems, such that the pressure length product of the model can be extracted independently of the pressure, as shown in (3.5), where L is the normalised system length. This value is useful for comparison with physical systems, but is not required for the operation of the model.

$$
\begin{aligned}
pl &= n_f k_B T_g l \\
&= n_f k_B T_g \frac{u_B}{n_f K_0} L \\
pl &= \frac{k_B T_g u_B}{K_0} L \quad \text{Pa m}
\end{aligned}
\tag{3.5}
$$

In the following application of the normalisation scheme to (3.3) and (3.4), the form of the Bohm velocity and the inverse nature of the temperature normalisation are used to remove all unnecessary constants from the equations.

From (3.3):

$$\begin{aligned}
\boldsymbol{\nabla} \cdot (n_\alpha \boldsymbol{u}_\alpha) &= \sum_{R_\alpha} G_{R_\alpha} n_{R_1} n_{R_2} K_R \\
n_f u_B \frac{n_f K_0}{u_B} \Gamma'_\alpha &= n_f^2 K_0 \sum_{R_\alpha} G_{R_\alpha} N_{R_1} N_{R_2} \epsilon_R \\
\Gamma'_\alpha &= \sum_{R_\alpha} G_{R_\alpha} N_{R_1} N_{R_2} \epsilon_R
\end{aligned} \tag{3.6}$$

From (3.4):

$$\begin{aligned}
k_B T_\alpha \boldsymbol{\nabla} n_\alpha =& \, n_\alpha Z_\alpha e \boldsymbol{E} \\
& - \sum_\beta \frac{m_\alpha m_\beta}{m_\alpha + m_\beta} n_\alpha n_\beta K_{\alpha\beta} (\boldsymbol{u}_\alpha - \boldsymbol{u}_\beta) \\
& - m_\alpha \boldsymbol{u}_\alpha \sum_{R_\alpha} G_{R_\alpha} n_{R_1} n_{R_2} K_R \\
k_B n_f T_e \frac{n_f K_0}{u_B} \gamma_\alpha^{-1} N'_\alpha =& \, n_f e N_\alpha Z_\alpha \boldsymbol{E} \\
& - m_i n_f^2 K_0 u_B \sum_\beta \frac{M_\alpha M_\beta}{M_\alpha + M_\beta} N_\alpha N_\beta \epsilon_{\alpha\beta} (V_\alpha - V_\beta) \\
& - m_i u_B n_f^2 K_0 M_\alpha V_\alpha \sum_{R_\alpha} G_{R_\alpha} N_{R_1} N_{R_2} \epsilon_R \\
k_B T_e \gamma_\alpha^{-1} N'_\alpha =& \, \frac{u_B e}{n_f K_0} N_\alpha Z_\alpha \boldsymbol{E} \\
& - m_i u_B^2 \sum_\beta \frac{M_\alpha M_\beta}{M_\alpha + M_\beta} N_\alpha N_\beta \epsilon_{\alpha\beta} (V_\alpha - V_\beta) \\
& - m_i u_B^2 M_\alpha V_\alpha \sum_{R_\alpha} G_{R_\alpha} N_{R_1} N_{R_2} \epsilon_R \\
k_B T_e \gamma_\alpha^{-1} N'_\alpha =& \, \frac{u_B e}{n_f K_0} N_\alpha Z_\alpha \boldsymbol{E} \\
& - k_B T_e \sum_\beta \frac{M_\alpha M_\beta}{M_\alpha + M_\beta} N_\alpha N_\beta \epsilon_{\alpha\beta} (V_\alpha - V_\beta) \\
& - k_B T_e M_\alpha V_\alpha \sum_{R_\alpha} G_{R_\alpha} N_{R_1} N_{R_2} \epsilon_R \\
\gamma_\alpha^{-1} N'_\alpha =& \, \frac{e}{k_B T_e} \frac{u_B}{n_f K_0} N_\alpha Z_\alpha \boldsymbol{E} \\
& - \sum_\beta \frac{M_\alpha M_\beta}{M_\alpha + M_\beta} N_\alpha N_\beta \epsilon_{\alpha\beta} (V_\alpha - V_\beta) \\
& - M_\alpha V_\alpha \sum_{R_\alpha} G_{R_\alpha} N_{R_1} N_{R_2} \epsilon_R
\end{aligned}$$

$$\begin{aligned} N'_\alpha =& \gamma_\alpha N_\alpha Z_\alpha \zeta \\ &- \gamma_\alpha \sum_\beta \frac{M_\alpha M_\beta}{M_\alpha + M_\beta} \epsilon_{\alpha\beta} \left(N_\beta \Gamma_\alpha - N_\alpha \Gamma_\beta \right) \\ &- M_\alpha \frac{\Gamma_\alpha}{N_\alpha} \gamma_\alpha \sum_{R_\alpha} G_{R_\alpha} N_{R_1} N_{R_2} \epsilon_R \end{aligned} \tag{3.7}$$

In the last step used to obtain (3.7), a normalised electric field, ζ, was introduced, as defined by (3.8). The normalised flux was also used to eliminate the particle velocity, as the particle conservation equation (3.6) is in terms of fluxes; velocity is not used elsewhere.

$$\boldsymbol{E} = \frac{k_B T_e}{e} \frac{n_f K_0}{u_B} \zeta \tag{3.8}$$

The expressions given in (3.6) and (3.7) can be built into a system that describes the behaviour of the densities and fluxes of an arbitrary number of species across a region of space. The equations are coupled between species through the collision terms; the densities through both elastic and reaction collisions, whereas the fluxes are directly coupled only through creation and destruction mechanisms. There is also a coupling between charged species densities through the electric field, as shown below.

The use of Poisson's equation is known to adversely affect the numerical complexity of fluid models by introducing a high level of stiffness into the equation set, which requires more complicated numerical solvers and smaller step sizes than a non-stiff equation set [105]. To avoid this, Poisson's equation is discarded and a different electric field term is used. This electric field is obtained from (3.7) and the quasineutrality condition (3.9). By collecting terms that are independent of the electric field, so that (3.7) becomes $N'_\alpha = Z_\alpha \gamma_\alpha N_\alpha \zeta + C_\alpha$, it is straightforward to derive an 'equilibrium' electric field, given in (3.10). This field can be explained as the electric field necessary to counteract all of the forces acting on the charged species, in order to maintain quasineutrality, as would be expected in an equilibrium system. This expression, like (3.6) and (3.7) can be applied to an arbitrary number of species.

$$\begin{aligned} \sum_\alpha Z_\alpha N_\alpha &= 0 \\ \sum_\alpha Z_\alpha N'_\alpha &= 0 \\ \sum_\alpha Z_\alpha^2 \gamma_\alpha N_\alpha \zeta + \sum_\alpha Z_\alpha C_\alpha &= 0 \end{aligned} \tag{3.9}$$

$$\zeta \sum_{\alpha} Z_{\alpha}^{2} \gamma_{\alpha} N_{\alpha} = -\sum_{\alpha} Z_{\alpha} C_{\alpha}$$

$$\zeta = \frac{-\sum_{\alpha} Z_{\alpha} C_{\alpha}}{\sum_{\alpha} Z_{\alpha}^{2} \gamma_{\alpha} N_{\alpha}} \tag{3.10}$$

Further to the expressions used in the system of differential equations, there are a handful of other useful expressions that arise from the assumption of a time averaged quasineutral plasma. As well as the aforementioned quasineutrality, the total current through the system must be zero at all locations, otherwise a charge imbalance would arise. Similarly, to prevent a net change in the mass contained in the system, the mass flow of species must also sum to zero. These two concepts can be expressed in terms of species fluxes, and are named current (3.11) and mass conservation (3.12) respectively.

$$\sum_{\alpha} Z_{\alpha} \Gamma_{\alpha} = 0 \tag{3.11}$$

$$\sum_{\alpha} M_{\alpha} \Gamma_{\alpha} = 0 \tag{3.12}$$

3.2 Parameter Specification

In order to obtain solutions for a system built using these equations, which is to be done numerically as previously discussed, one must obtain numbers for each of the remaining quantities. The species densities and fluxes require values provided by the boundary conditions. Values or expressions must also be determined for those variables that are not accounted for in the integration. The particle mass (m_{α}) and charge (Z_{α}) are simply determined by the species included in the model, but the rate coefficients for elastic collisions and chemical reactions, $K_{\alpha\beta}$ and K_R respectively, will need to be obtained from literature values for the specific reactions, and may be energy dependent. Temperatures for species will need to be estimated, or used as controls for the model, depending on the species.

3.2.1 Boundary Conditions

In order to perform a numerical integration, boundary conditions need to be specified. The densities and fluxes of each species each require a definition for at least one point in space. The species fluxes are simple to define: symmetry across the discharge centre requires that the species fluxes be zero at the centre. As the system being investigated

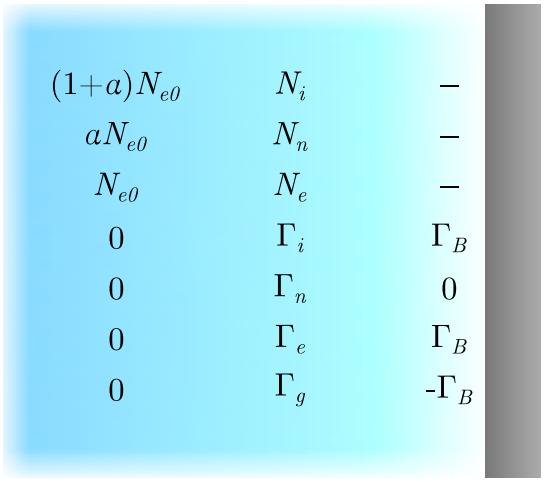

Figure 7: Isothermal model boundary conditions. Central plasma conditions are on the left, edge values are on the right.

is symmetric, any non-zero flux across the centre would represent a deviation from equilibrium, which does not agree with the assumption of time averaging. The species densities are not prescribed by symmetry or other assumptions made, however at this point it is useful to recognise that the definition of electronegativity is still valid, and that it can be used to reduce the boundary conditions that are required. Thus the central densities of the three species are determined through the normalised central electron density and the electronegativity. These conditions are demonstrated in figure 7, which also shows that the species fluxes have specified values at the edge, as is discussed below.

An unfortunate side effect of the normalisation scheme is that, due to the decoupling of the physical discharge parameters, the spatial extent of the plasma is not known until the edge boundary conditions are met. As the system edge is the start of a sheath, then the obvious measure for detecting this point is the Bohm criterion, which specifies the positive ion velocity at the boundary between the bulk and sheath, as discussed in Section 2.1. This then allows the specification of the ion flux at the outer boundary. As the negative ion flux is assumed to be zero at this point (see below), then one can also state boundary values for the electron and neutral fluxes through the current and mass conservation equations.

As the system to be modelled is fully quasineutral, only the bulk plasma is considered, and integration stops at the sheath edge. If one combines this with the knowledge that the negative ion flux is always towards the centre due to the confining potential that exists, and that no negative ions are produced in the sheath, then the negative ion

flux must be zero at the sheath edge. This does not mean that the negative ion flux is always zero at the system edge; non-negligible negative ion fluxes have been reported in a variety of real and theoretical systems [106–111]. However the assumptions applied to be able to effectively solve the model preclude these system from being described by this model.

Due to having boundary conditions at both the centre and edge of the system, the negative ion flux is overdetermined, and its edge boundary condition can be used to determine a value for the central electronegativity, which would otherwise be a free parameter. The normalised central electron density is to be used as a control variable for the model, as the relative plasma density is an important parameter in physical systems.

Through the collection of boundary conditions described above, and from examination of the equation set built using (3.6) and (3.7), it is apparent that the model requires the specification of only the temperature of each species and the central normalised electron density.

Up to this stage in the development of the model, the system has remained general, and applicable to any chosen set of species. In order to provide values for the particle properties and the reaction rate coefficients, one must choose the species to be modelled and the reactions between them.

3.2.2 Species and reaction selection

In order to test the model under development, a relatively simple test case gas is desired, one that provides negative ions but can be well described with a minimum of other required species, and is also well studied so that the necessary literature values are available and comparisons can be drawn with previous work. Oxygen fits all of these requirements, and is additionally relevant for a number of industrial processes, such as sterilisation, growth of metal oxide films, or modification of surface work functions [112–114]. The properties of an oxygen plasma can be moderately well described by considering only the dominant ionic species O_2^+ and O^- [13]. However, one must also take into account the effects of one of the molecular excited states, $O_2\left(^1\Delta_g\right)$, which takes part in a number of the dominant reactions [115]. It is an important reaction partner for the O^- negative ion, and an additional ionisation pathway for the creation of O_2^+. Unfortunately, as $O_2\left(^1\Delta_g\right)$ is influenced heavily by wall interactions, it is not possible to include it as a self consistent fluid in the model. To provide a

Table 2: Reaction set to be used for modelling of an oxygen discharge

Code	Reaction	Process
I	$O_2 + e^- \rightarrow O_2^+ + 2e^-$	Ionisation
IM	$O_2 + e^- \rightarrow O^- + \frac{1}{2}O_2$	Dissociative attachment
EN	$O_2^+ + e^- \rightarrow O_2$	Electron attachment neutralisation
ED	$O^- + e^- \rightarrow \frac{1}{2}O_2 + 2e^-$	Electron impact detachment neutralisation
SI	$O_2\left(^1\Delta_g\right) + e^- \rightarrow O_2^+ + 2e^-$	Ionisation
SB	$O_2\left(^1\Delta_g\right) + e^- \rightarrow O^- + \frac{1}{2}O_2$	Dissociative attachment
MN	$O_2^+ + O^- \rightarrow O_2 + \frac{1}{2}O_2$	Mutual Neutralisation
SD	$O_2\left(^1\Delta_g\right) + O^- \rightarrow O_2 + \frac{1}{2}O_2 + e^-$	De-excitation detachment
eg	$O_2 + e^- \rightarrow O_2 + e^-$	Momentum transfer
ig	$O_2 + O_2^+ \rightarrow O_2 + O_2^+$	Momentum transfer
ng	$O_2 + O^- \rightarrow O_2 + O^-$	Momentum transfer

value for the fractional density of $O_2\left(^1\Delta_g\right)$, $f_s = \bar{n}_{O_2(^1\Delta_g)}/\bar{n}_{O_2}$, data taken from a full fluid model [116] was analysed for a range of conditions. It was found that a simple polynomial fit as a function of T_e well described the behaviour of the $O_2\left(^1\Delta_g\right)$ density fraction, as it varied between 10% and 30%.

The restriction to these particular species also removes additional excited states of O_2, atomic oxygen and associated excited states, ozone (O_3), and other ionisation states of these species. By further assuming that the model applies to low pressure systems, and so three body collisions can be neglected, the set of reactions for oxygen is reduced from 117 to just 11 [117], which are shown in table 2. Some of these reactions generate atomic oxygen, the behaviour of which is also dominated by wall interactions. As wall interactions are not considered, the product of these reactions is instead represented as $\frac{1}{2}O_2$.

3.2.3 Reaction Rate Coefficients

In order to include the reactions listed in the model, one needs to obtain values that can be used to describe them. As discussed in Section 2.3, values for reaction rate coefficients are not always simple to obtain. As the primary focus of this work is currently model development and comparability, the reaction rate coefficients to be used are obtained in a similar manner to those used in [13], with rate coefficients for reactions involving electrons calculated using BOLSIG+, as discussed in Section 2.3.3. The

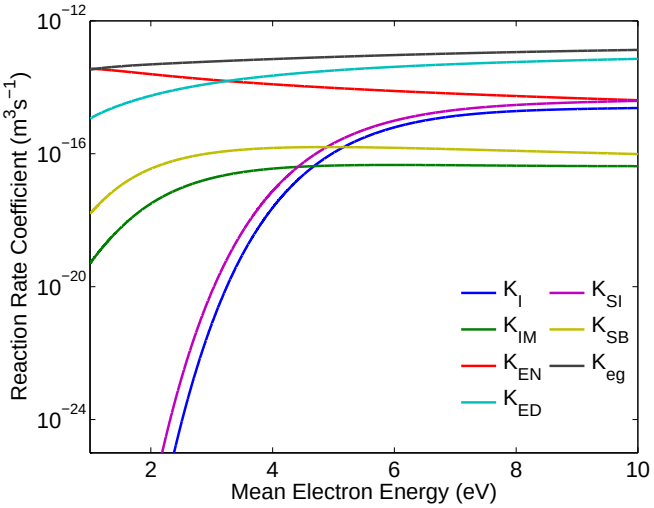

Figure 8: Dependence on mean electron energy of reaction rate coefficients for reactions involving electrons.

output from the program is tabulated values of reaction rate coefficient as a function of mean electron energy. It is possible to then estimate the value of these rate coefficients for any value of mean electron energy by interpolating between two known values. However, interpolation from a table is significantly more computationally expensive than evaluating a function. It was found that all of the rate coefficients could be well estimated, to within roughly 1%, by the function given in (3.13), where the coefficients $a_{R,n}$ are found through linear regression in logarithmic space.

$$K_R = \exp\left[\sum_{n=1}^{9} a_{R,n} \ln\left(T_e\right)^{n-1}\right] \tag{3.13}$$

Reactions between heavy species can be estimated through assuming a Maxwellian EDF, and values for these have been taken from the literature. Some, such the mutual neutralisation coefficient [118], are easy to find, but others require a significant amount of searching. The set of rate coefficients used in the model are given in table 3, and those listed as a function of electron energy are plotted in figure 8. The coefficients used by the model to recreate these curves as a function of T_e can be found in table 4.

At this stage it is useful to specify the species temperatures as $T_i = T_n = T_g = 300\,\mathrm{K}$, and T_e as a control parameter.

Table 3: O_2 reaction rate coefficients to be used in the isothermal model. T_g in Kelvin. $f(T_e)$ indicates RRC estimated from function fitted to tabulated data.

Code	Reaction	RRC (m^3s^{-1})	Reference
I	$O_2 + e^- \rightarrow O_2^+ + 2e^-$	$f(T_e)$	[119]
IM	$O_2 + e^- \rightarrow O^- + \frac{1}{2}O_2$	$f(T_e)$	[120]
EN*	$O_2^+ + e^- \rightarrow O_2$	$f(T_e)$	[82, 120]
ED	$O^- + e^- \rightarrow \frac{1}{2}O_2 + 2e^-$	$f(T_e)$	[120]
SI	$O_2\left(^1\Delta_g\right) + e^- \rightarrow O_2^+ + 2e^-$	$f(T_e)$	[117]
SB	$O_2\left(^1\Delta_g\right) + e^- \rightarrow O^- + \frac{1}{2}O_2$	$f(T_e)$	[121]
MN	$O_2^+ + O^- \rightarrow O_2 + \frac{1}{2}O_2$	$2 \times 10^{-13}\left(\frac{300}{T_g}\right)$	[118]
SD	$O_2\left(^1\Delta_g\right) + O^- \rightarrow O_2 + \frac{1}{2}O_2 + e^-$	$3 \times 10^{-16}\left(\frac{T_g}{300}\right)^{0.5}$	[117]
eg	$O_2 + e^- \rightarrow O_2 + e^-$	$f(T_e)$	[119]
ig	$O_2 + O_2^+ \rightarrow O_2 + O_2^+$	$1 \times 10^{-15}\left(\frac{T_g}{300}\right)^{0.5}$	[117]
ng	$O_2 + O^- \rightarrow O_2 + O^-$	2×10^{-15}	[122]

* Recombination to excited state and subsequent de-excitation is considered but not explicitly included.

Table 4: Fitting coefficients $a_{R,n}$ from (3.13) for reactions that are a function of T_e, given to 5 significant figures.

Code	n								
	1	2	3	4	5	6	7	8	9
I	-0.047732	0.93623	-7.2361	27.384	-49.657	30.313	4.9540	36.203	-95.053
IM	-0.0060283	0.11377	-0.82932	2.851	-4.2799	1.1865	0.76977	5.7634	-44.443
EN	0.00056304	-0.011162	0.087716	-0.34414	0.68838	-0.57155	-0.25464	-0.27301	-30.937
ED	-0.00057099	0.012191	-0.10469	0.45519	-1.0201	1.0269	-0.54625	2.4233	-34.404
SI	-0.035885	0.69742	-5.3128	19.589	-33.475	15.708	6.6035	36.267	-89.567
SB	-0.0014788	0.025949	-0.16598	0.40976	0.08844	-1.8681	0.73798	4.7871	-40.999
eg	0.00046639	-0.0091317	0.06973	-0.25547	0.42606	-0.17783	-0.19301	0.64854	-31.011

3.3 Numerical Solution

The model as described so far gives a description of the featured properties for a region of space between the discharge centre and the sheath. As mentioned previously the equations require solution through numerical methods, and so this region must be discretised. There is a choice between two families of solution methods, as the model is currently suitable for integration as either a BVP or IVP. Formulation as a BVP would allow a reasonably simple solution through discretisation, but this faces the same long execution time as a full fluid model. Solving the system as an IVP gives the potential for a greatly reduced integration time, at the expense of a more complicated numerical scheme. As one of the main motivations for this model is fast computation, the ability to solve as an IVP is valuable. This section details the numerical considerations and algorithms required to solve the system as such.

3.3.1 Numerical Integration Method

Many tools are available to perform initial value integration of systems of first order ordinary differential equations, as the problem is one faced by many disciplines. Dedicated applications exist, as do libraries for a large variety of programming languages and environments. Due to its flexibility, availability, and reputation, the numerical schemes are developed in MATLAB. For numerical integration, the `ode113` routine in MATLAB 7.14 [123] is used, which employs a predictor-corrector, linear, variable order, multistep solver (Adams-Bashforth-Moulton method [124]). See Section 2.5 for more details on numerical integration methods.

The boundary conditions specified in figure 7 indicate that the integration as an IVP is best performed spatially from the centre of the discharge to the sheath edge. Despite not being solved as a typical boundary value problem, it is still highly beneficial to have known system bounds. However, as previously mentioned, the physical size of the plasma is not known before the integration is complete. Thus in order to have definitive integration bounds, a different coordinate must be used. The only variable known to be monotonic over the discharge, and have defined centre and edge values for all discharge conditions, is the normalised positive ion velocity, $V_i = \Gamma_i/N_i$. As shown in figure 7 and discussed in Section 3.2.1, the sheath boundary is determined by the point at which the positive ions reach the Bohm velocity. As velocities are normalised to this value, the integration bounds are determined by $V_i = 0$ at the centre, and $V_i = 1$ at the edge. This change is effected by simply dividing the calculated gradients by V_i'

(3.14) and including an extra variable, with a spatial derivative of 1, to track the true spatial coordinate.

$$\begin{aligned} V_i' &= \left(\frac{\Gamma_i}{N_i}\right)' \\ &= \frac{N_i\Gamma_i' - \Gamma_i N_i'}{N_i^2} \\ V_i' &= \frac{\Gamma_i' - \Gamma_i \left(\ln N_i\right)'}{N_i} \end{aligned} \tag{3.14}$$

It is worth noting that despite there existing a modified Bohm criterion for electronegative plasmas [29], it is derived by assuming that both negative ions and electrons are in Boltzmann equilibrium with the plasma potential (see Section 2.1), and that negative ions are present at the sheath edge. As neither of these assumptions hold in this system, the modified Bohm criterion is not considered here.

A further change to the integration scheme is made by transforming the equations to describe the natural logarithm of density values. This is done to improve the numerical stability of the integration, due to the occasionally large differences between density values, and also prevents overshoot to negative density if the automatic step size is too large. To make this change, (3.7) is divided by the species density to provide the logarithmic derivative, and then (3.6) and (3.7) are updated to accept $L_\alpha = \ln\left(N_\alpha\right)$ as arguments, as shown in (3.15) and (3.16).

$$\Gamma_\alpha' = \sum_{R_\alpha} G_{R_\alpha} \epsilon_R \exp\left(L_{R_1} + L_{R_2}\right) \tag{3.15}$$

$$\begin{aligned} L_\alpha' = &\gamma_\alpha Z_\alpha \zeta \\ &- \gamma_\alpha \mathrm{e}^{-L_\alpha} \sum_\beta \frac{M_\alpha M_\beta}{M_\alpha + M_\beta} \epsilon_{\alpha\beta} \left(\mathrm{e}^{L_\beta}\Gamma_\alpha - \mathrm{e}^{L_\alpha}\Gamma_\beta\right) \\ &- M_\alpha \Gamma_\alpha \mathrm{e}^{-L_\alpha} \gamma_\alpha \Gamma_\alpha' \end{aligned} \tag{3.16}$$

3.3.2 Electronegativity Minimisation

As shown in figure 7, the negative ion flux (Γ_n) is required to be zero at the sheath edge, that is $\Gamma_{n,L} = 0$, where L refers to edge values. As symmetry dictates also that $\Gamma_{n,0} = 0$, it is the species densities that have control over whether or not this edge boundary condition is met. As mentioned above, $\Gamma_{n,L}$ is controlled indirectly by the central electronegativity α_0. It is therefore necessary to repeat the integration with different values of α_0 and minimise the value of $|\Gamma_{n,L}|$. Unfortunately, due to

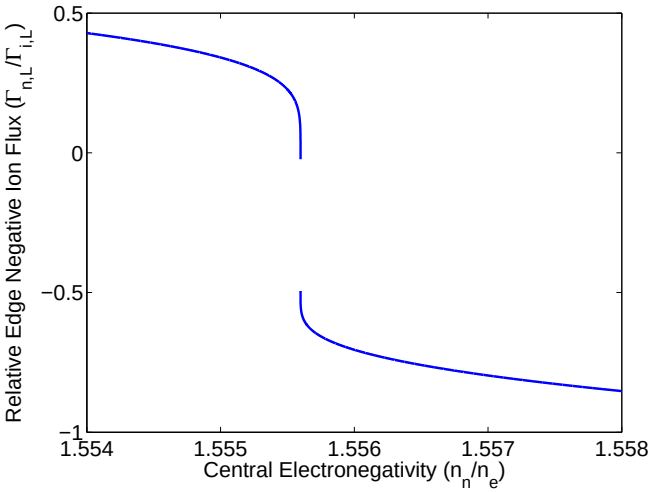

Figure 9: Example of how the edge value of negative ion flux depends on the central electronegativity. At the limit of double precision, there is a jump discontinuity close to, but not at, $\Gamma_{n,L} = 0$. Finding the root of this function through the use of gradients or fitting would most likely fail.

the highly non-linear characteristics of the equation system, the parameter space of α_0 and $\Gamma_{n,L}$ is not trivial, and can contain steep gradients and discontinuities, as demonstrated in figure 9. Thus standard root finding routines often fail to converge, or are impractically slow. In order to have an automatic solution, a custom root finding algorithm is required.

The algorithm starts with a very low value (10^{-2}) for the electronegativity, which is increased until two values are found that bracket the solution. From here, the algorithm progresses using minimisation by bisection, with a variety of integration outputs being used to indicate in which direction the minimisation should progress to avoid the discontinuities. The routine continues until either $|\Gamma_{n,L}| < 10^{-10} \times \Gamma_{i,L}$ or the value of α_0 is specified to the working numerical precision. Relating the negative to positive ion flux means that the minimisation tolerance is expressed as a relative value, enabling the same value to be used regardless of the input conditions. This proves to be a robust method for a large range of input conditions.

3.3.3 Perturbations

Despite the minimisation routine being able to give the required α_0 to the limit of double precision (approximately 15 significant figures), there are still cases where the highly non-linear nature of the equations prevents the condition $\Gamma_{n,L} = 0$ from being met to an acceptable level, through an inability to specify a precise enough α_0.

Each set of initial conditions can be considered the starting point for a trajectory

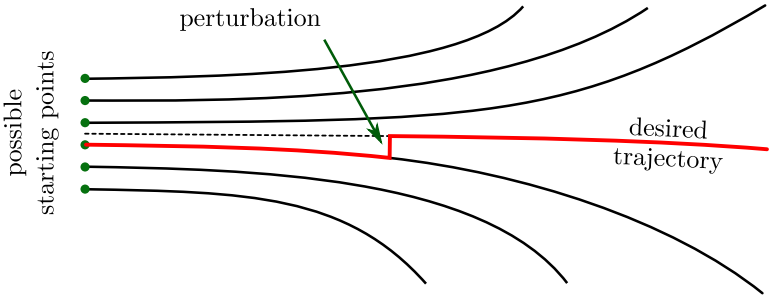

Figure 10: Demonstration of the concept of using perturbations to overcome sensitivity in initial conditions in computational systems. Points show the discretised starting conditions, and the bold line is numerical path taken.

in the full parameter space, approximated by the numerical integration process. Under certain conditions, these trajectories are highly divergent, and those that meet the edge boundary conditions may differ in their initial state from those that do not by an impractically small amount. To access these trajectories one of two things must happen. One could increase the working precision of the integration, allowing access to more initial trajectories. Although this is a rigorous solution, it drastically increases the computation time. The alternative is to join the desired trajectory at a later point in the integration, when the difference between them in parameter space is large enough to be resolved at the working precision, as shown in figure 10.

Thus the trajectories are accessed part way through the integration, through small perturbations to the ion densities, on the order of $\Delta N/N \approx 10^{-7}$. A bisection type search is performed on the best solution found using the α_0 minimisation by applying a small increase to the positive and negative ion densities, equal to $d \times N_n$, where $d_0 = 10^{-7}$, at integration output points until the last point is found that does not change the sign of $\Gamma_{n,L}$. From here a second bisection is performed on d until either $(N_n + d \times N_n)$ is specified to double precision or the tolerance on $|\Gamma_{n,L}|$ is met, which is $10^{-10} \times \Gamma_{i,L}$ as mentioned above. In the case that $(N_n + d \times N_n)$ is specified to the limit of double precision without the condition on $\Gamma_{n,L}$ being met, then the perturbation process is repeated. An example of this process is given in figure 11.

The perturbation of order 10^{-7} is smaller than or comparable to the change in densities between each integration step, so the effect on the final solution compared with increasing the working precision is negligible.

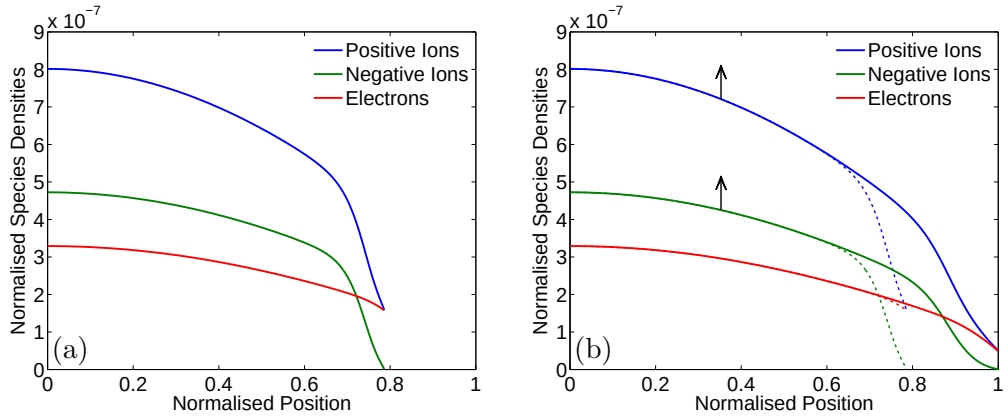

Figure 11: Example of the perturbation process. Shown in (a) are the charged species densities profiles with α_0 specified to the limit of double precision, but with $\Gamma_{n,L} \neq 0$. In (b) a single small perturbation is applied, increasing the ion densities by roughly one part in 10^7. The downstream effect of this small change is clear.

3.4 Results

When creating a model, being confident of the assumptions, analytics, and numerics behind it does not guarantee that the results from it are correct or even sensible. To make judgements on this, the model must be used to generate outputs, and these outputs analysed. This process will be started by investigation of the model outputs from a single set of input conditions, chosen to represent typical operating parameters found in the literature [49, 82, 86, 125, 126]. From the inputs, profiles of densities and fluxes are calculated as described, and these are shown in figure 12.

3.4.1 Typical Conditions

The first thing that one may notice in these plots is that there are two distinct regions in space. From the centre, charged species densities, given in figure 12(a), are approximately parabolic, but there is then a transition into some sort of presheath structure. This behaviour was described by [67], and fits in with their idea of a collisional electronegative plasma where the negative ion behaviour is dominated by electron detachment, as opposed to recombination processes. For the discharge shown, the maximum mean free paths, as a fraction of the discharge length, of the positive and negative ions are 1.5 % and 0.73 % respectively, and for the electrons it is 8 %. This shows that the discharge is collisional, and it can also be shown through analysis of the reaction rates that this particular plasma falls within the detachment dominated regime.

Further examination of these plots shows that all of the boundary conditions detailed in figure 7 are met, and that the conservation laws (3.11) and (3.12) hold. These

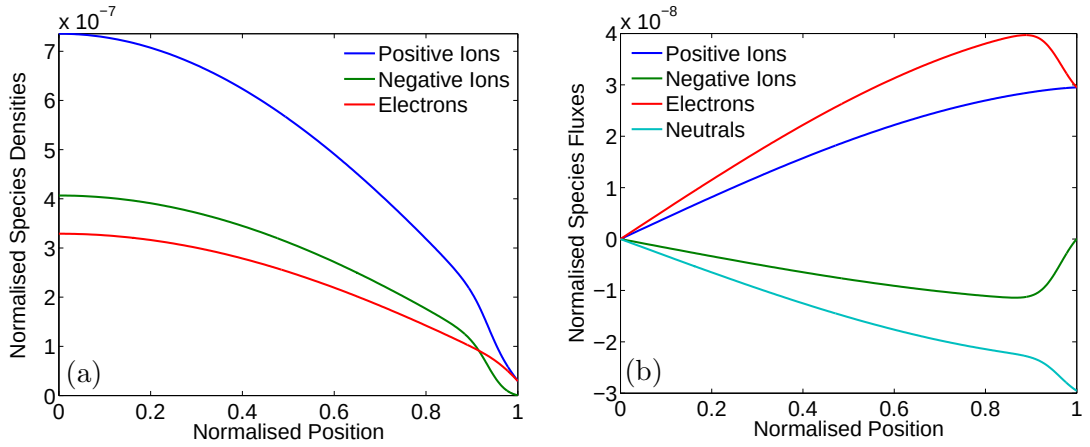

Figure 12: Normalised species densities (a) and fluxes (b) for the isothermal model, with input parameters of $T_e = 4\,\text{eV}$ and $N_{e0} = 3.3 \times 10^{-7}$. The spatial coordinate has been normalised for ease of understanding.

can also be confirmed numerically. When looking at the species fluxes, it could be interpreted that the electrons are retarded as they approach the edge, which would contradict the usual understanding of the electrons and positive ion streaming out from the discharge centre. In fact, the steady decrease in electron density means that the electron velocity is monotonically increasing across the discharge.

3.4.2 Multiple Inputs

The results from a single set of inputs are encouraging, but the model must also be able to handle a large range of discharge conditions. For this reason, a selection of results were calculated for a number of different electron temperatures and densities; these are given in figures 13 to 15.

Looking first at the plots of density, in figure 13, it is shown that the change in electron temperature has the largest impact. Increasing the electron density by four orders of magnitude has very little effect on these results. The profiles taken with $T_e = 3.8\,\text{eV}$ are similar to the density shown in figure 12, with an approximately parabolic trajectory for each species, and a small transition region at the edge. In fact, the densities for the lower electron density ($N_{e0} = 1 \times 10^{-10}$) are closest to parabolic; the profiles given in figure 13(b) have been influenced by the increase in the electron density, and the densities do not fall as rapidly as those with lower N_{e0}.

Turning to the effect of increased electron temperature, there is a dramatic change in the density profiles, and the electronegativity has increased markedly. Instead of all three charged species decreasing together, the electron density is roughly constant, and ion densities drop until the negative ion density is very low. Then there is a

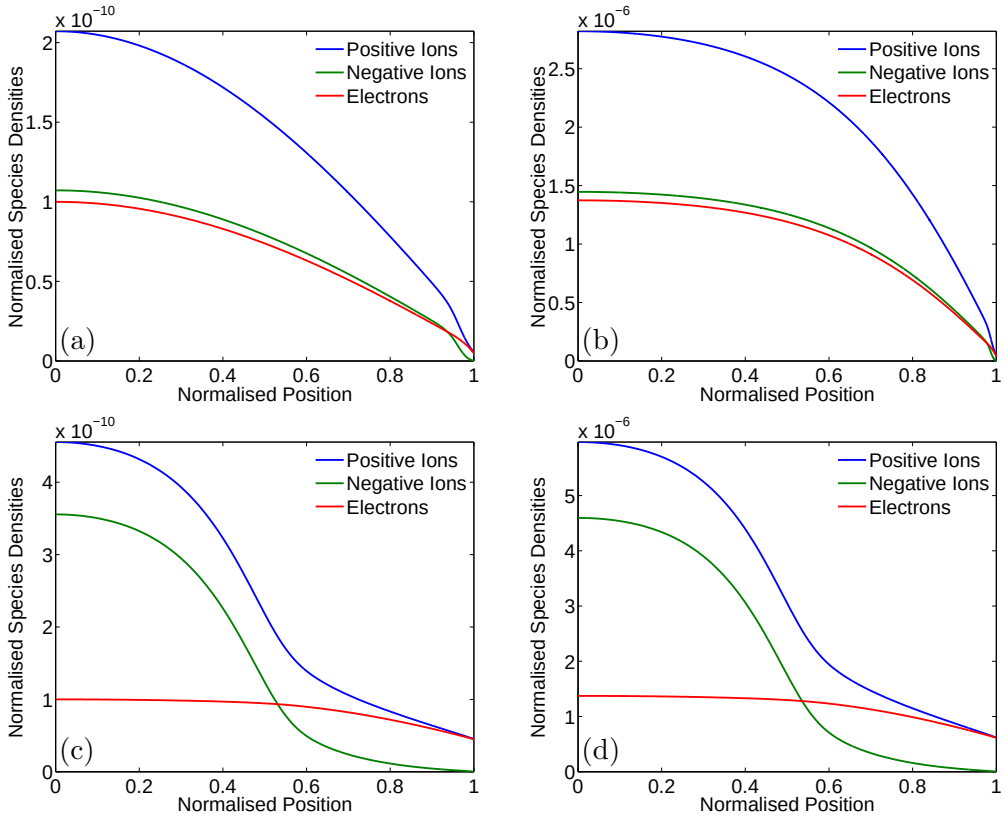

Figure 13: Normalised species densities for different values of electron temperature and density. $T_e = 3.8\,\text{eV}$ in (a) and (b), and $5\,\text{eV}$ for (c) and (d). $N_{e0} = 1 \times 10^{-10}$ in (a) and (c), and 1.4×10^{-6} for (b) and (d).

change in behaviour, and the electron density drops off while the negative ions slowly decay to zero. Looking back to [67], this adheres to their description of the difference between 'structured' and 'non-structured' discharges. The 'structure' being referred to in this instance is the separation of the plasma bulk into an electronegative core, and a (mostly) electropositive edge region. They use the ratios of the positive and negative ion mobilities and production rates to determine a dimensionless numerical measure of the degree of structuring that should occur. The results presented so far all agree with this measure, and fall the appropriate side of the structured/non-structured boundary.

Turning to the results for the particle fluxes, given in figure 14, the interpretation of these plots is found to be more abstract than for the species densities. In the 'unstructured' results, parts (a) and (b) of figures 13 and 14, there is again the sudden transition into a presheath, but this time the effect of the change in electron density is clearer. Although the numerical values for the initial flux gradients are greater in figure 14(b) than in figure 14(a), as the plasma density is higher, they are lower relative to the rest of the discharge. This could be due to the plasma density remaining higher for further, and so increasing the flux gradients later in the integration.

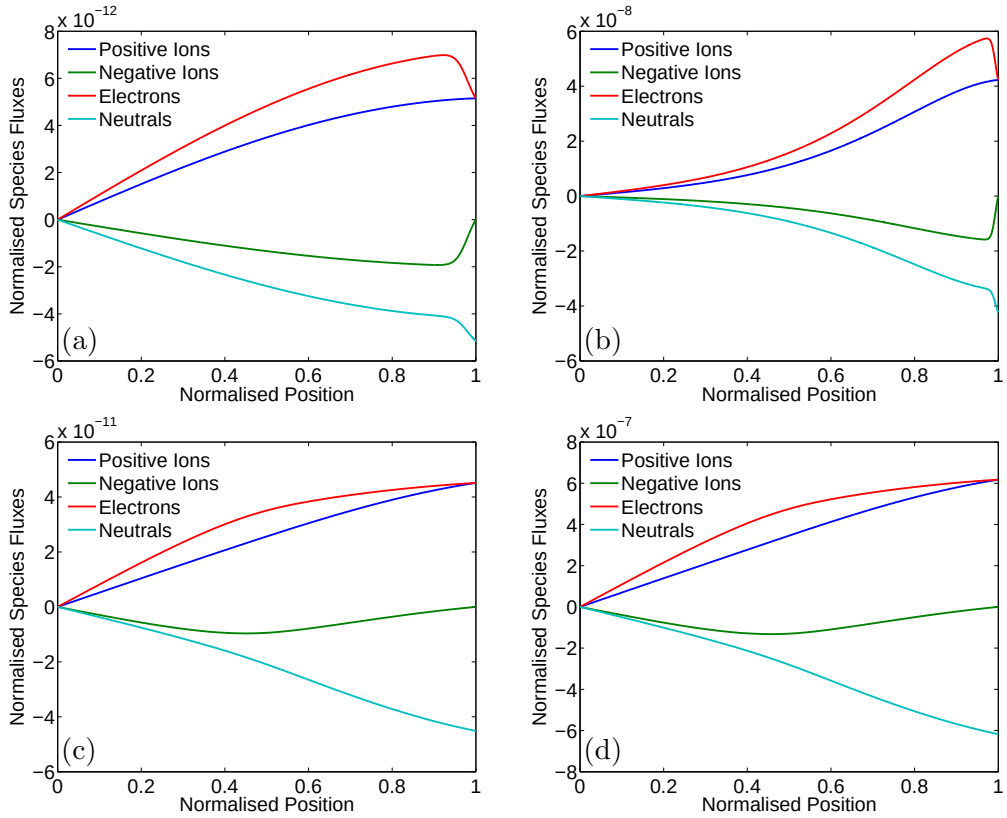

Figure 14: Normalised species fluxes for different values of electron temperature and density. $T_e = 3.8\,\text{eV}$ in (a) and (b), and $5\,\text{eV}$ for (c) and (d). $N_{e0} = 1 \times 10^{-10}$ in (a) and (c), and 1.4×10^{-6} for (b) and (d).

This is in contrast to the results for the structured discharge, given in figures 14(c) and (d), where, like the density results, the two sets of profiles are qualitatively almost indistinguishable. This identical behaviour despite the electron density differing by four orders of magnitude can be attributed to the high electron temperature drastically increasing certain rate coefficients. The system behaviour is then determined more by the reactions between electrons and neutrals than those between charged particles, so increasing the plasma density has a smaller impact on the relative creation and destruction rates than similar changes at a lower electron temperature. Also worth noting is that although the negative ion density is very small from a normalised position of 0.6 onwards, the magnitude of the negative ion flux is still quite high. This indicates that the velocity of negative ions is large in the outer section of the plasma, and is explained by a confining potential that accelerates any negative ions that are created outside of the electronegative core.

Further to the predictions of [67], qualitative agreement can be shown with experimental results. For the results with high electron temperature given in figures 13 and 14, the ion density profiles match well qualitatively with the low pressure results

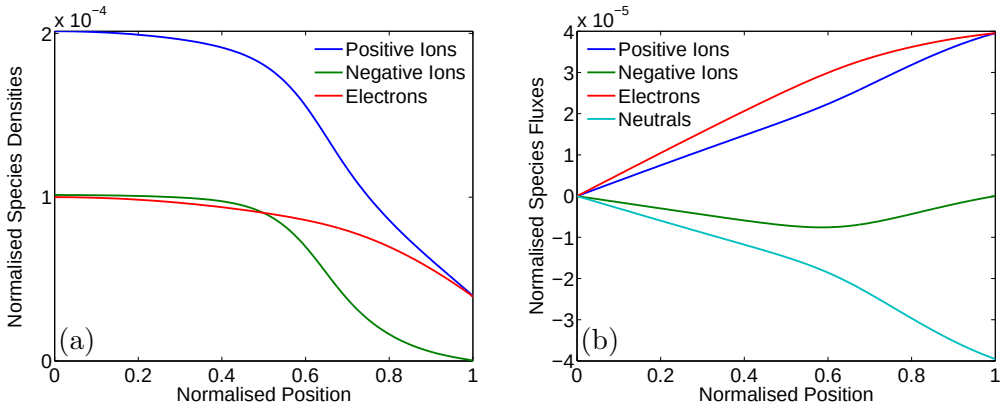

Figure 15: Normalised species densities (a) and fluxes (b) for $T_e = 5\,\text{eV}$ and $N_{e0} = 1 \times 10^{-4}$.

from [127].

When gathering the example results given in figures 13 and 14, it was discovered that at $T_e = 3.8\,\text{eV}$, it was not possible to obtain a result for a relative electron density of greater than 10^{-6}. However, it was possible at $T_e = 5\,\text{eV}$, the results of which are shown in figure 15. Comparing this result to figures 13(d) and 14(d) it is clear that the increase in electron density now has an effect. Although the flux behaviour is similar, the density profiles are notably different. In particular, although the 'structured' behaviour remains, the electronegativity is lower, and similar to that of the low electron temperature examples. This indicates that at higher plasma densities, changes to the density can cause changes to the behaviour of the system, in contrast to low electron density where such properties are almost wholly dependent on the electron temperature. However, further insight requires a more detailed investigation to be carried out, which will also provide more information on the inability to solve for certain conditions.

3.4.3 Parameter Sweep

One of the main advantages of the semi-analytical model is the short time taken to provide a solution. This means it is possible to conduct a detailed investigation of behaviour over a large range of input parameters in a practical amount of time. An automated sweep across a wide range of electron densities and temperatures was performed, with 2000 individual runs of the model taking an average of 60.4 seconds per run, although the majority of runs took less than 26 seconds. This disparity will be discussed later. The relative electron density was varied logarithmically from 10^{-10} to 10^{-2}, and the electron temperature linearly from 3.5 eV to 7 eV. In order to investigate

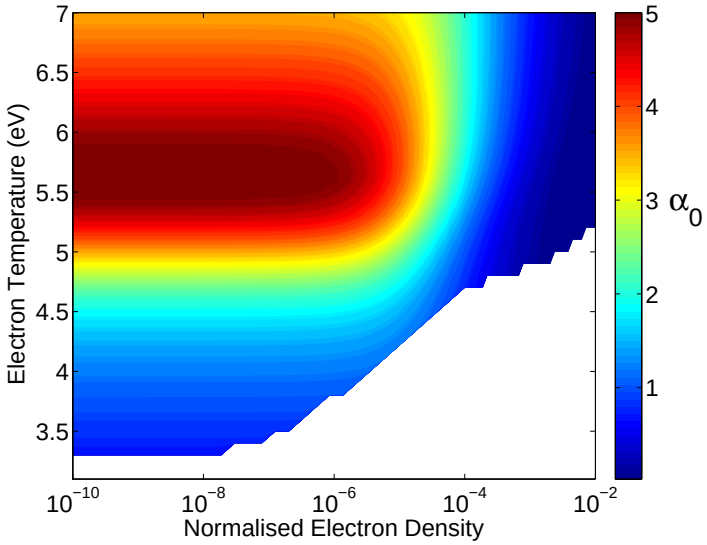

Figure 16: Behaviour of central electronegativity as a function of electron density and temperature input to the isothermal model.

the behaviour of the model over such a broad range, it is useful to designate single numerical values that can provide insight into the characteristics of each run. The central electronegativity (α_0) is known to be non-trivially altered by both input parameters, and so this has been plotted as a function of the input parameters in figure 16.

There are two features of this plot that are immediately apparent. One is that the lack of solution at high electron density and low electron temperature has a clear boundary, but not a trivial shape. The other obvious feature is that there is a maximum in electronegativity at a certain electron temperature of roughly 5.6 eV. A third important feature, but one that does not stand out as much, is that the electronegativity exhibits differing behaviours either side of a relative electron density of around 10^{-6}.

If one refers to the profiles of species fluxes, it is clear that the positive and negative ion fluxes, $\Gamma_{i,0}$ and $\Gamma_{n,0}$, are always positive and negative, respectively. The same is true of their respective initial gradients, $\Gamma'_{i,0}$ and $\Gamma'_{n,0}$. Through investigation of the initial conditions, it becomes clear that if either $\Gamma_{i,0} < 0$ or $\Gamma_{n,0} > 0$ then the numerical integration rapidly deteriorates to a situation that is unphysical, often through a collapse or explosion of densities. It can be said that the central flux gradients must adhere to the inequalities $\Gamma_{i,0} \geq 0$ and $\Gamma_{n,0} \leq 0$, otherwise the initial conditions are unphysical for the assumptions that build this model.

From (3.6) and table 2 it is possible to give expressions for both $\Gamma'_{i,0}$ and $\Gamma'_{n,0}$ as a function of the initial conditions T_e, N_{e0}, and α_0. These are given in (3.17) and (3.18),

where the dependence on T_e is through the values for reaction rate coefficients.

$$\Gamma'_{i,0} = (1-f_s)\,N_{g,0}N_{e,0}\epsilon_I - N_{i,0}N_{n,0}\epsilon_{MN} - N_{i,0}N_{e,0}\epsilon_{EN} + f_sN_{g,0}N_{e,0}\epsilon_{SI} \tag{3.17}$$

$$\begin{aligned}\Gamma'_{n,0} = (1-f_s)\,N_{g,0}N_{e,0}\epsilon_{IM} - N_{i,0}N_{n,0}\epsilon_{MN} - N_{n,0}N_{e,0}\epsilon_{ED} \\ - f_sN_{g,0}N_{n,0}\epsilon_{SD} + f_sN_{g,0}N_{e,0}\epsilon_{SB}\end{aligned} \tag{3.18}$$

Each of these two expressions can be rearranged into an inequality that is quadratic in α_0, using $N_g = 1$. $N_n = \alpha_0 N_e$, and $N_i = (1+\alpha_0)\,N_e$, as given in (3.19) and (3.20).

$$\begin{aligned}(1-f_s)\,N_{g,0}N_{e,0}\epsilon_I - N_{i,0}N_{n,0}\epsilon_{MN} - N_{i,0}N_{e,0}\epsilon_{EN} + f_sN_{g,0}N_{e,0}\epsilon_{SI} \geq 0 \\ (1-f_s)\,N_{e,0}\epsilon_I - (1+\alpha_0)\,\alpha_0N_{e,0}^2\epsilon_{MN} \\ - (1+\alpha_0)\,N_{e,0}\epsilon_{EN} + f_sN_{e,0}\epsilon_{SI} \geq 0 \\ [(1-f_s)\,N_{e,0}\epsilon_I + f_sN_{e,0}\epsilon_{SI} - N_{e,0}\epsilon_{EN}] \\ - \alpha_0\left[N_{e,0}^2\epsilon_{MN} + N_{e,0}\epsilon_{EN}\right] - \alpha_0^2N_{e,0}^2\epsilon_{MN} \geq 0 \\ [(1-f_s)\,\epsilon_I + f_s\epsilon_{SI} - \epsilon_{EN}] - \alpha_0\left[N_{e,0}\epsilon_{MN} + \epsilon_{EN}\right] - \alpha_0^2N_{e,0}\epsilon_{MN} \geq 0\end{aligned} \tag{3.19}$$

$$\begin{aligned}(1-f_s)\,N_{g,0}N_{e,0}\epsilon_{IM} - N_{i,0}N_{n,0}\epsilon_{MN} \\ - N_{n,0}N_{e,0}\epsilon_{ED} - f_sN_{g,0}N_{n,0}\epsilon_{SD} + f_sN_{g,0}N_{e,0}\epsilon_{SB} \leq 0 \\ (1-f_s)\,N_{e,0}\epsilon_{IM} - (1+\alpha_0)\,\alpha_0N_{e,0}^2\epsilon_{MN} \\ - \alpha_0N_{e,0}^2\epsilon_{ED} - f_s\alpha_0N_{e,0}\epsilon_{SD} + f_sN_{e,0}\epsilon_{SB} \leq 0 \\ [(1-f_s)\,N_{e,0}\epsilon_{IM} + f_sN_{e,0}\epsilon_{SB}] \\ - \alpha_0[N_{e,0}^2\epsilon_{MN} + N_{e,0}^2\epsilon_{ED} + f_sN_{e,0}\epsilon_{SD}] - \alpha_0^2N_{e,0}^2\epsilon_{MN} \leq 0 \\ [(1-f_s)\,\epsilon_{IM} + f_s\epsilon_{SB}] \\ - \alpha_0[N_{e,0}\epsilon_{MN} + N_{e,0}\epsilon_{ED} + f_s\epsilon_{SD}] - \alpha_0^2N_{e,0}\epsilon_{MN} \leq 0\end{aligned} \tag{3.20}$$

As each of the expressions (3.19) and (3.20) contain simple quadratics, it is easy to find the roots of the associated equations as functions of electron temperature and density. It is found that (3.19) provides an upper bound, and (3.20) a lower bound on the possible values of α_0. As the electron temperature and density change, these bounds shift independently. In some cases they cross, meaning that there is no physical value of α_0 that meets both inequalities. If a detailed search is performed on where this occurs, it is found that the electron density-temperature parameter space is split into two regions. The boundary between these two regions is plotted over the previous parameter sweep results in figure 17.

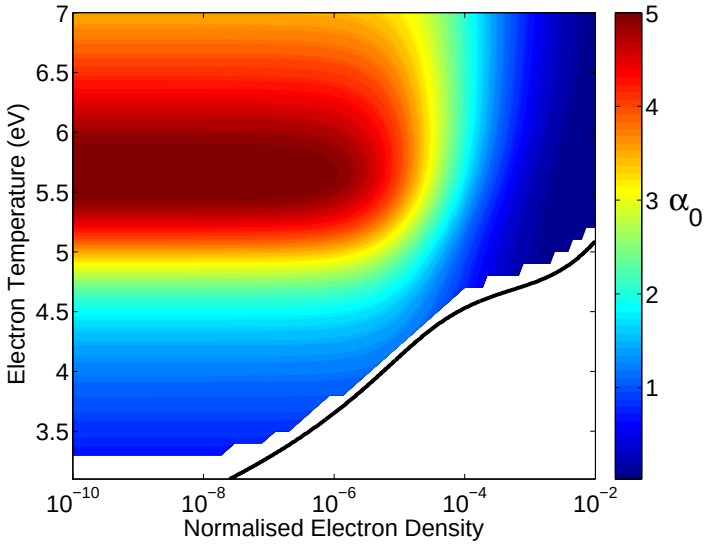

Figure 17: Behaviour of central electronegativity as a function of electron density and temperature input to the isothermal model, including the theoretical boundary of validity.

It is clear that this theoretical restriction plays a large role in determining where solutions to the model exist, but also that it does not give the full picture. The stepping that is evident in the electronegativity results and some of the discrepancy between the edge of the solutions and the theoretical limit can be explained by the comparatively coarse stepping used in the parameter sweep. It may also be partly due to the different method of calculation used in the root finding of (3.20) compared with in the model. As some reaction rates differ by many orders of magnitude, numerical artefacts can be caused by performing calculations in a different order, leading to a difference in the reported root. However, at the low electron densities and temperatures, there is a discrepancy that cannot be explained by these effects.

It is possible to explain the issues at the lowest electron temperatures through a numerical issue, rather than a theoretical one. As the electron temperature decreases, the value of α_0 that gives the correct $\Gamma_{n,L}$ moves closer to the lower bound given by (3.20). This means that for a given electron density, the absolute value of $\Gamma'_{n,0}$ at the correct value of α_0 decreases as one decreases the electron temperature. On top of this the magnitude of the gradient $\mathrm{d}\Gamma'_{n,0}/\mathrm{d}\alpha_0$ increases with decreasing electron temperature. These two effects compound into a dramatically increased sensitivity to initial conditions at the lower electron temperatures. This can be seen in figure 18. Shown is the negative correlation between the computation time needed, which is indicative of the number of perturbations required, and the distance of the 'correct' α_0 from the lower bound from (3.20).

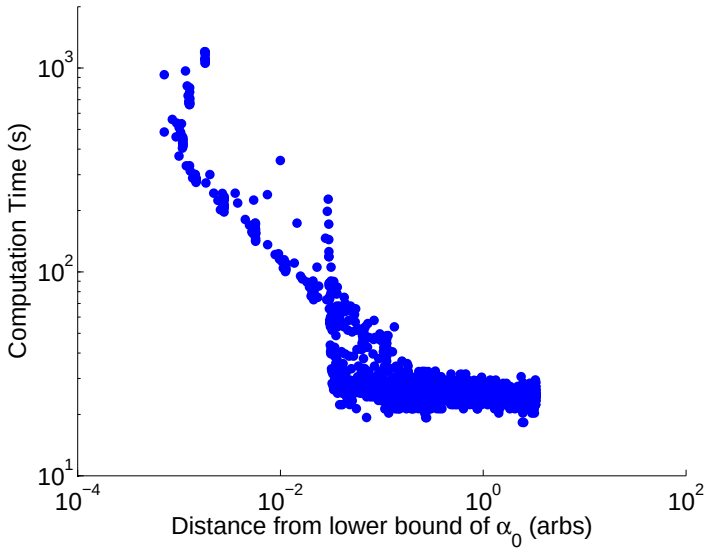

Figure 18: Scatter plot demonstrating the negative correlation between the computation time of the isothermal model and the distance between the final value of α_0 and the lower bound. The Pearson correlation coefficient between the logarithms of the two variables is -0.820, indicating a strong negative correlation. Data is taken from the same model runs as figure 16.

As an explanation for the lack of solution at values of T_e lower than 3.3 eV, as the sensitivity increases, the computation time is indicative of the computational difficulty of finding the correct solution. Thus as the electron temperature drops below about 3.5 eV, the computational difficulty starts to increase dramatically, before the solver automatically terminates the execution due to the excessive computation time. There is also the question of how many perturbations can be applied before the result starts to deviate from the actual solution.

A similar situation is observed at higher values of T_e if the electron density causes one to approach the limit of validity shown in figure 17. Closer to this line the sensitivity and computational complexity increase, and so the model is unable to provide solutions that are close to it in parameter space. This dramatic increase in computational difficulty also explains the previously mentioned disparity between the mean and median of the execution times for this data.

With the parameter space irregularities explained, it is now desirable to investigate the actual behaviour of the electronegativity across the valid parameter range. A cursory observation of the electronegativity values shows that at low electron densities, α_0 depends almost exclusively on the electron temperature. At higher electron densities, this situation is reversed, and most of the dependence is on electron density. At the lower electron densities, there is also a clear maximum in electronegativity at

$T_e \approx 5.6\,\mathrm{eV}$, though this disappears as the behaviour of α_0 changes to depend on N_{e0}.

The explanation of the change in behaviour is that at low ionisation fractions, the negative ion destruction pathways involving neutral species dominate many times over those between charged particles only. However, as one increases the ionisation fraction, reactions between charged species start to become important. This then elicits a mode transition such that destruction of negative ions through collisions with positive ions and electrons starts to noticeably alter the dominant reactions of the system, at an ionisation fraction of around 10^{-6}, causing a reduction in electronegativity with increasing electron density. The change in behaviour is over too wide a range of conditions to be observed in a typical experiment, however an inverse trend of electronegativity with input power has been demonstrated [128], along with the expected positive trend of electron density with input power.

Turning to the relationship between α_0 and T_e, there is a clear maximum at the lower electron densities. Through analysis of the behaviours of the various reaction rates and how they influence the electronegativity, it is found that there is a concurrent minimum in the expression for f_s, the fractional density of $O_2\left(^1\Delta_g\right)$, which is entirely responsible for the maximum shown in figure 16. As reported in [116], the precise density of $O_2\left(^1\Delta_g\right)$ is highly dependent on specific discharge properties, such as the surface loss probability. As $O_2\left(^1\Delta_g\right)$ is an important destruction pathway for O^-, the electronegativity is also affected in this manner, particularly when the rate of destruction through electron impact detachment is small due to a low electron density. Due to this sensitivity, and because the maximum in electronegativity is solely due to the density of $O_2\left(^1\Delta_g\right)$, it is not clear whether or not this maximum should exist, or if it is an artefact of the model itself.

It is reported in [129] that the electronegativity should decrease with increasing system pressure, although these results were obtained from a PIC model that does not self consistently solve for the $O_2\left(^1\Delta_g\right)$ density, but assumes it is constant. As shown in figure 19, the electron temperature is strongly negatively correlated with the system pressure-length product, which is consistent with both simple theoretical descriptions [19] and experimental results [45]. Thus the increase of electronegativity with increasing T_e would be consistent with the findings of [129], which can be seen between electron temperatures of 3.3 eV to 5 eV. As temperatures above this range are beyond the scope of the empirical relation used for the density of $O_2\left(^1\Delta_g\right)$, the results for electronegativity at higher electron temperatures above around 5.5 eV, particularly

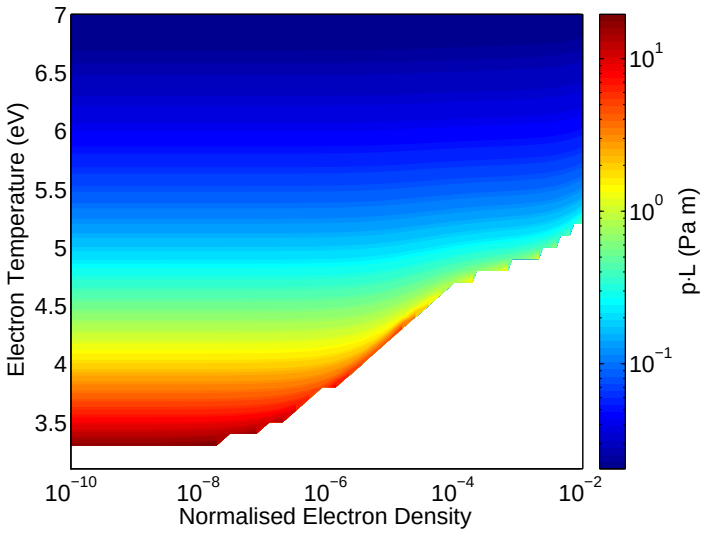

Figure 19: Behaviour of system pressure-length product as a function of electron density and temperature for the isothermal model. The contours are spaced logarithmically to capture the large variation.

those having $N_{e0} \leq 10^{-6}$, are considered incorrect. This is conformant with the general inability of fluid models to provide accurate results at low pressures, due to the breakdown of the assumption of high collisionality.

The predictions of simple theoretical treatments of plasmas state that in a physical system, T_e is determined by the system pressure-length product, and n_e by the input power density. The power deposition into the plasma is not considered in this model, so the second prediction is moot. Looking in more detail at figure 19, it is clear that although the first prediction broadly holds, there is some dependence of $p \cdot L$ on the electron density, most noticeably at higher values of N_{e0}, and as one approaches the limit of possible solutions discussed previously. This can again be attributed to the self interaction of the plasma as the charged species density increases, which is not considered in the theoretical predictions.

3.5 Conclusions

In order to demonstrate the inaccuracies of the isothermal model, detailed data was obtained from a full fluid model [13] to compare against (see Appendix A for more details). The relative electron density and mean electron energy from a set of data from the full fluid model was used to perform a run of the isothermal model, and the gas density from the full fluid model was used to unravel the normalisations in the results. The absolute charged species densities of each model are given in figure 20.

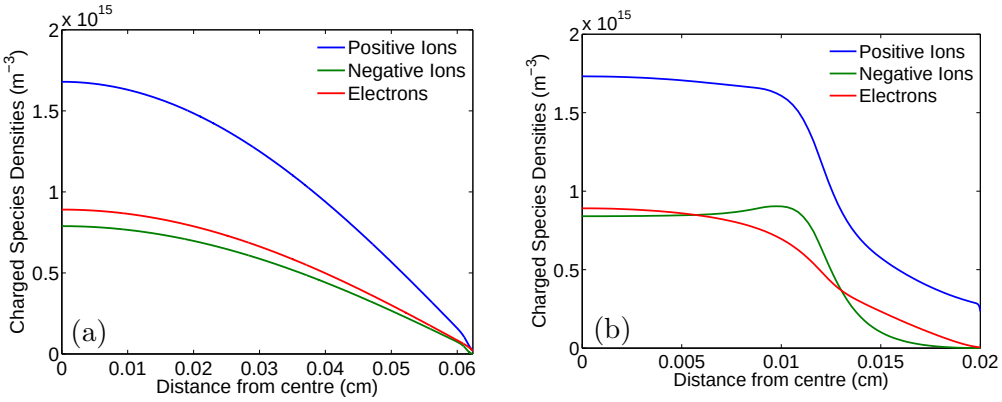

Figure 20: Comparison of charged species density profiles from (a) the isothermal model and (b) a full fluid model for a relative electron density of 6.15×10^{-8} and mean electron energy of 3.56 eV.

As the full fluid model includes a great deal more information, including space charges, time resolution and no assumptions on isothermality of the electrons, the large differences between the two results shows that the isothermal model performs poorly. Although the electronegativity differs by less than 10 %, the rest of the density information disagrees. In particular, the full fluid model has profiles that are far from parabolic, and actually non-monotonic. There is also a difference in the spatial scale of the two models. In the full fluid model, solution is through a boundary value integration, and so the spatial extent is prescribed. Although the inclusion of space charges means that the discharge length of the semi-analytical model will be different compared with the full fluid model, it should be smaller due to the space taken by the sheath, and not greater as shown in figure 20(a).

Despite the results obtained from this isothermal model appearing mostly sensible, there is still a disparity between the model results and those given in experiments and other models. Qualitative agreements are hard to come by, and quantitative agreements do not exist.

When investigating the literature for experimental results to compare against, data was found for the spatial profile of electron temperature, in a discharge that has conditions that fall within the remit of the isothermal model [130]. Experiments and models have shown that the electron temperature in this type of discharge is far from constant, and can vary by a few eV across the discharge [36, 131, 132]. This can also be seen in results from the full fluid model. If one looks at how a few eV affects reaction rate coefficients, as given in figure 8, it is clear that a few eV could change reaction rates by multiple orders of magnitude. In particular, the ionisation rates for the creation of

O_2^+ are very strongly affected by small changes in electron temperature in the region of 3 eV to 4 eV.

Despite the obvious inaccuracies of the isothermal model, the fact that the results are not preposterous shows that the theoretical and numerical procedures used are valid, and that it is the assumptions that require changing. This is presented in the next chapter.

Chapter 4

Non-Uniform Electron Temperature

In the previous chapter, it was shown that while it is possible to create an isothermal model of an electronegative plasma, the results do not elicit great confidence. This is partly as, in reality, the temperature of the electrons is far from constant in space or time, and so an isothermal approximation is not valid. In this chapter, the extension of the model to provide a self-consistent evaluation of the spatial profile of electron temperature will be demonstrated. Discussions of electron heating and power deposition effects will take place, and the effect on the solutions when compared to the isothermal model will be examined.

4.1 Equation Development

The plasma being described in this chapter, and the assumptions made, are otherwise the same as is detailed in Chapter 3, and so the representations of the zeroth Boltzmann moment are the same as given in (3.3). However, as the assumption of isothermal electrons has been removed, there are differences to consider. For the first moment of the Boltzmann equation, the inclusion of an electron temperature gradient means that when simplifying the pressure term in (3.2), a temperature gradient term emerges and must be included on the RHS of (3.4). As mentioned in Section 2.4.4, it is also important to consider the effect that the spatially varying temperature has on elastic collisions. As the electron-neutral elastic collision rate coefficient is energy dependent, a gradient in electron temperature will also create a gradient in elastic collision rate. This results in a spatially varying mean free path, and so particles travelling in opposite

directions, but otherwise identical, will experience different number of collisions, and so there will be a net effect on the average particle momentum.

Crucially, there is now an additional equation for the electron energy balance, the full form of which is given in (2.42). There is also the need to provide an expression for the electron heat flux, which is discussed in Section 2.4.5, and given in (2.44).

4.1.1 Assumption Application

The assumptions from the isothermal model, with the exception of that of isothermal electrons, are applied to equations (2.40) to (2.42). In addition, a combination of three assumptions $T_e \gg T_g$, $m_e \ll m_g$, and $n_e < n_g$ allow the simplification of the terms in (2.41) and (2.42) involving the effect of temperature gradients on the elastic collision rate. This is shown in (4.1) where the dimensionless factor g_e is derived to be a function of T_e.

$$\frac{T_{eg}}{\nu_{eg}}\frac{\mathrm{d}\nu_{eg}}{\mathrm{d}T_{eg}} \approx \frac{T_e}{n_g K_{eg}}\frac{\mathrm{d}\left(n_g K_{eg}\right)}{\mathrm{d}T_e} \tag{4.1a}$$

$$= \frac{T_e}{n_g K_{eg}}\left[n_g \frac{\mathrm{d}K_{eg}}{\mathrm{d}T_e} + K_{eg}\frac{\mathrm{d}n_g}{\mathrm{d}T_e}\right] \tag{4.1b}$$

$$\approx \frac{T_e}{K_{eg}}\frac{\mathrm{d}K_{eg}}{\mathrm{d}T_e} \tag{4.1c}$$

$$= g_e\left(T_e\right) \tag{4.1d}$$

Power deposition in a collisional RF plasma is mostly in the form of ohmic heating, as discussed in Section 2.1. As the electric field oscillates, electrons are driven back and forth across the plasma and extract energy from the RF field through collisions with the neutral species. However, as the equations describing this model are time averaged, this effect is not captured. In order to deposit energy in the electrons, an external power source must be included in the energy balance equation. Applying these considerations results in (4.2) to (4.4), where S_e is a volumetric power deposition in $\mathrm{W\,m^{-3}}$. Also included in this term are energy losses through inelastic collisions, as will be discussed later.

$$\boldsymbol{\nabla}\cdot\left(n_\alpha \boldsymbol{u}_\alpha\right) = \sum_{R_\alpha} G_{R_\alpha} n_{R_1} n_{R_2} K_R \tag{4.2}$$

$$\begin{aligned} k_B T_\alpha \boldsymbol{\nabla} n_\alpha =& n_\alpha Z_\alpha e\boldsymbol{E} - \sum_\beta \frac{m_\alpha m_\beta}{m_\alpha + m_\beta} n_\alpha n_\beta K_{\alpha\beta}\left(\boldsymbol{u}_\alpha - \boldsymbol{u}_\beta\right) \\ & - m_\alpha \boldsymbol{u}_\alpha \sum_{R_\alpha} G_{R_\alpha} n_{R_1} n_{R_2} K_R \underbrace{-n_\alpha k_B \boldsymbol{\nabla} T_\alpha + n_\alpha k_B g_\alpha \boldsymbol{\nabla} T_\alpha}_{\text{for e}^- \text{ only}} \end{aligned} \tag{4.3}$$

$$\begin{aligned}\tfrac{3}{2}k_B n_e \boldsymbol{u}_e \cdot \boldsymbol{\nabla} T_e + n_e k_B T_e \boldsymbol{\nabla} \cdot \boldsymbol{u}_e + \boldsymbol{\nabla} \cdot \boldsymbol{q}_e = S_e \\ + \left(\tfrac{1}{2}m_e u_e^2 - \tfrac{3}{2}k_B T_e\right) \sum_{R_e} G_{R_e} n_{R_1} n_{R_2} K_R - n_e \boldsymbol{u}_e g_e k_B \boldsymbol{\nabla} T_e \\ + \sum_{\beta} \frac{m_e m_\beta}{(m_e + m_\beta)^2} n_e n_\beta K_{e\beta} \left[m_\beta \left(\boldsymbol{u}_e - \boldsymbol{u}_\beta\right)^2 - 3k_B \left(T_e - T_\beta\right) \right]\end{aligned} \tag{4.4}$$

As can be seen in (4.4), it is the gradient of the heat flux that is required for solution of the equation set. The two parts of the electron heat flux gradient are derived below, and the result is given in (4.5).

$$\begin{aligned}\boldsymbol{\nabla} \boldsymbol{q}_e &= \boldsymbol{\nabla} \left[-\left(\frac{5}{2} - g_e\right) k_B^2 \frac{n_e T_e}{m_e \nu_{\alpha\beta}} \boldsymbol{\nabla} T_e - g_e n_e k_B T_e \boldsymbol{u}_e \right] \\ &= \boldsymbol{\nabla} \left[-\left(\frac{5}{2} - g_e\right) k_B^2 \frac{n_e T_e}{m_e \nu_{\alpha\beta}} \boldsymbol{\nabla} T_e \right] + \boldsymbol{\nabla} \left[-g_e n_e k_B T_e \boldsymbol{u}_e \right]\end{aligned}$$

$$\begin{aligned}\boldsymbol{\nabla} \left[-\left(\tfrac{5}{2} - g_e\right) k_B^2 \frac{n_e T_e}{m_e \nu_{\alpha\beta}} \boldsymbol{\nabla} T_e \right] = \\ - \frac{k_B^2}{m_e} \Bigg[\frac{n_e T_e}{\nu_{eg}} \boldsymbol{\nabla} T_e \left(-\boldsymbol{\nabla} g_e\right) + \left(\tfrac{5}{2} - g_e\right) \frac{T_e}{\nu_{eg}} \boldsymbol{\nabla} T_e \boldsymbol{\nabla} n_e \\ + \left(\tfrac{5}{2} - g_e\right) \frac{n_e T_e}{\nu_{eg}} \boldsymbol{\nabla}^2 T_e + \left(\tfrac{5}{2} - g_e\right) n_e \boldsymbol{\nabla} T_e \frac{\boldsymbol{\nabla} T_e \nu_{eg} - T_e \boldsymbol{\nabla} \nu_{eg}}{\nu_{eg}^2} \Bigg]\end{aligned}$$

$$\begin{aligned}\boldsymbol{\nabla} \left[-\left(\tfrac{5}{2} - g_e\right) k_B^2 \frac{n_e T_e}{m_e \nu_{\alpha\beta}} \boldsymbol{\nabla} T_e \right] = \\ - \frac{k_B^2}{m_e} \Bigg[\frac{n_e}{\nu_{eg}} T_e \frac{\mathrm{d}g_e}{\mathrm{d}T_e} \left(\boldsymbol{\nabla} T_e\right)^2 + \left(\tfrac{5}{2} - g_e\right) \frac{T_e}{\nu_{eg}} \boldsymbol{\nabla} T_e \boldsymbol{\nabla} n_e \\ + \left(\tfrac{5}{2} - g_e\right) \frac{n_e T_e}{\nu_{eg}} \boldsymbol{\nabla}^2 T_e + \left(\tfrac{5}{2} - g_e\right) \frac{n_e}{\nu_{eg}} \left(\boldsymbol{\nabla} T_e\right)^2 - \left(\tfrac{5}{2} - g_e\right) \frac{n_e}{\nu_{eg}} g_e \left(\boldsymbol{\nabla} T_e\right)^2 \Bigg]\end{aligned}$$

$$\begin{aligned}\boldsymbol{\nabla} \left[-\left(\tfrac{5}{2} - g_e\right) k_B^2 \frac{n_e T_e}{m_e \nu_{\alpha\beta}} \boldsymbol{\nabla} T_e \right] = - \left(\tfrac{5}{2} - g_e\right) k_B^2 \frac{n_e T_e}{m_e \nu_{eg}} \boldsymbol{\nabla}^2 T_e \\ - \left(\tfrac{5}{2} - g_e\right) k_B^2 \frac{T_e}{m_e \nu_{eg}} \boldsymbol{\nabla} T_e \boldsymbol{\nabla} n_e - \left[(1 - g_e) \left(\tfrac{5}{2} - g_e\right) - T_e \frac{\mathrm{d}g_e}{\mathrm{d}T_e} \right] k_B^2 \frac{n_e}{m_e \nu_{eg}} \left(\boldsymbol{\nabla} T_e\right)^2\end{aligned}$$

$$\begin{aligned}\boldsymbol{\nabla} \left(-k_B g_e n_e T_e \boldsymbol{u}_e\right) = -k_B g_e n_e T_e \boldsymbol{\nabla} \left(n_e \boldsymbol{u}_e\right) - k_B g_e n_e \boldsymbol{u}_e \boldsymbol{\nabla} T_e \\ - k_B n_e \boldsymbol{u}_e T_e \frac{\mathrm{d}g_e}{\mathrm{d}T_e} \boldsymbol{\nabla} T_e\end{aligned}$$

$$\begin{aligned}\boldsymbol{\nabla}\cdot\boldsymbol{q} = &-\left(\tfrac{5}{2}-g_e\right)k_B^2\frac{n_eT_e}{m_e\nu_{eg}}\boldsymbol{\nabla}^2T_e-\left(\tfrac{5}{2}-g_e\right)k_B^2\frac{T_e}{m_e\nu_{eg}}\boldsymbol{\nabla}T_e\boldsymbol{\nabla}n_e\\ &-k_Bg_en_e\boldsymbol{u}_e\boldsymbol{\nabla}T_e-\left[(1-g_e)\left(\tfrac{5}{2}-g_e\right)-T_e\frac{\mathrm{d}g_e}{\mathrm{d}T_e}\right]k_B^2\frac{n_e}{m_e\nu_{eg}}\left(\boldsymbol{\nabla}T_e\right)^2\\ &-k_Bg_eT_e\boldsymbol{\nabla}\left(n_e\boldsymbol{u}_e\right)-k_Bn_e\boldsymbol{u}_eT_e\frac{\mathrm{d}g_e}{\mathrm{d}T_e}\boldsymbol{\nabla}T_e\end{aligned}\tag{4.5}$$

4.1.2 Normalisation

The system of equations (4.2) to (4.5) are to be normalised in a similar fashion to those in Section 3.1.2. The only difference is that, as T_e is no longer constant, temperatures will be normalised to the central electron temperature, so that $T_\alpha = T_{e0}/\gamma_\alpha$. This also changes the used definition of the Bohm velocity to $u_B^2 = k_BT_{e0}/m_i$, so that the edge criterion is not affected by the evolution of the electron temperature through space. The derivation of a Bohm criterion requires Maxwellian electrons in a collisionless plasma, and so any expression for it is only ever an estimation of the sheath edge. Indeed, the existence, or not, of any rigorous expression for a sheath edge, and the form that it may take, is an ongoing topic of contention [133–138]. These are the justifications for the slight differences that may exist between the definition of u_B presented here, and those found elsewhere.

With these small changes to the normalisation scheme in mind, the normalisations are applied to (4.2) to (4.5) below. From (4.2):

$$\begin{aligned}\boldsymbol{\nabla}\cdot\left(n_\alpha\boldsymbol{u}_\alpha\right) &= \sum_{R_\alpha}G_{R_\alpha}n_{R_1}n_{R_2}K_R\\ n_fu_B\frac{n_fK_0}{u_B}\Gamma'_\alpha &= n_f^2K_0\sum_{R_\alpha}G_{R_\alpha}N_{R_1}N_{R_2}\epsilon_R\\ \Gamma'_\alpha &= \sum_{R_\alpha}G_{R_\alpha}N_{R_1}N_{R_2}\epsilon_R\end{aligned}\tag{4.6}$$

For brevity, the normalisation is applied to (4.3) as it applies to electrons. The term involving the gradient of the elastic collision rate is removed for species that are not electrons. From the normalisation scheme, $T'_\alpha/T_{e0} = -\gamma'_\alpha/\gamma_\alpha^2$, which is used in the

following derivations.

$$
\begin{aligned}
k_B T_\alpha \boldsymbol{\nabla} n_\alpha =& \, n_\alpha Z_\alpha e \boldsymbol{E} \\
&- \sum_\beta \frac{m_\alpha m_\beta}{m_\alpha + m_\beta} n_\alpha n_\beta K_{\alpha\beta} \left(\boldsymbol{u}_\alpha - \boldsymbol{u}_\beta \right) \\
&- m_\alpha \boldsymbol{u}_\alpha \sum_{R_\alpha} G_{R_\alpha} n_{R_1} n_{R_2} K_R \\
&+ n_\alpha k_B g_\alpha \boldsymbol{\nabla} T_\alpha - n_\alpha k_B \boldsymbol{\nabla} T_\alpha \\
k_B n_f \frac{n_f K_0}{u_B} T_{e0} \gamma_\alpha^{-1} N'_\alpha =& \, n_f N_\alpha Z_\alpha e \boldsymbol{E} \\
&- m_i n_f^2 K_0 u_B \sum_\beta \frac{M_\alpha M_\beta}{M_\alpha + M_\beta} N_\alpha N_\beta \epsilon_{\alpha\beta} \left(V_\alpha - V_\beta \right) \\
&- m_i u_B n_f^2 K_0 M_\alpha V_\alpha \sum_{R_\alpha} G_{R_\alpha} N_{R_1} N_{R_2} \epsilon_R \\
&- k_B n_f \frac{n_f K_0}{u_B} \left(1 - g_\alpha \right) N_\alpha T'_\alpha \\
\gamma_\alpha^{-1} N'_\alpha =& \, \frac{e}{k_B T_{e0}} \frac{u_B}{n_f K_0} N_\alpha Z_\alpha \boldsymbol{E} \\
&- \frac{m_i u_B^2}{k_B T_{e0}} \sum_\beta \frac{M_\alpha M_\beta}{M_\alpha + M_\beta} N_\alpha N_\beta \epsilon_{\alpha\beta} \left(V_\alpha - V_\beta \right) \\
&- \frac{m_i u_B^2}{k_B T_{e0}} M_\alpha V_\alpha \sum_{R_\alpha} G_{R_\alpha} N_{R_1} N_{R_2} \epsilon_R \\
&- \left(1 - g_\alpha \right) N_\alpha \frac{T'_\alpha}{T_{e0}}
\end{aligned}
$$

$$
\begin{aligned}
N'_\alpha =& \, N_\alpha \gamma_\alpha Z_\alpha \zeta - \gamma_\alpha \sum_\beta \frac{M_\alpha M_\beta}{M_\alpha + M_\beta} \epsilon_{\alpha\beta} \left(N_\beta \Gamma_\alpha - N_\alpha \Gamma_\beta \right) \\
&- \gamma_\alpha M_\alpha \frac{\Gamma_\alpha}{N_\alpha} \sum_{R_\alpha} G_{R_\alpha} N_{R_1} N_{R_2} \epsilon_R + \left(1 - g_\alpha \right) N_\alpha \frac{\gamma'_\alpha}{\gamma_\alpha}
\end{aligned}
\tag{4.7}
$$

For ease of understanding, the normalisations will be applied separately to (4.4) and (4.5), and the two results will then be combined. Were they to be combined before normalisation, the resulting expression would be unwieldy and incredibly difficult to follow. The elastic collision frequency gradient coefficient is already dimensionless, so does not need normalisation. Both it and its relative energy derivative, $T_e \frac{\mathrm{d}g_e}{\mathrm{d}T_e}$, are untouched by the normalisation process also because later steps to find values for them are made easier by doing so.

Starting at (4.4), and introducing a normalised volumetric power deposition, $\Sigma_e =$

$S_e/(n_f^2 K_0 k_B T_{e0})$, one can normalise the power balance expression to obtain (4.8).

$$
\begin{aligned}
\left(\tfrac{3}{2}+g_e\right) k_B n_e \boldsymbol{u}_e \cdot \boldsymbol{\nabla} T_e = &- k_B T_e \boldsymbol{\nabla}\cdot(n_e \boldsymbol{u}_e) \\
&+ \boldsymbol{u}_e k_B T_e \boldsymbol{\nabla} n_e \\
&- \boldsymbol{\nabla}\cdot \boldsymbol{q}_e \\
&+ \left(\tfrac{1}{2} m_e u_e^2 - \tfrac{3}{2} k_B T_e\right) \sum_{R_e} G_{R_e} n_{R_1} n_{R_2} K_R \\
&+ S_e \\
&+ \sum_\beta \Bigg\{ \frac{m_e m_\beta}{(m_e+m_\beta)^2} n_e n_\beta K_{e\beta} \\
&\quad \times \left[m_\beta (\boldsymbol{u}_e - \boldsymbol{u}_\beta)^2 - 3 k_B (T_e - T_\beta) \right] \Bigg\} \\
k_B n_f u_B \frac{n_f K_0}{u_B} T_{e0} \left(\tfrac{3}{2}+g_e\right) \Gamma_e \frac{T_e'}{T_{e0}} = &- k_B n_f u_B \frac{n_f K_0}{u_B} T_{e0} \gamma_e^{-1} \Gamma_e' \\
&+ k_B n_f u_B \frac{n_f K_0}{u_B} T_{e0} \gamma_e^{-1} V_e N_e' \\
&- n_f u_B k_B T_{e0} \frac{n_f K_0}{u_B} Q' \\
&+ \left(m_i u_B^2 \tfrac{1}{2} M_e V_e^2 - \tfrac{3}{2} k_B T_{e0} \gamma_\alpha^{-1} \right) n_f^2 K_0 \\
&\quad \times \sum_{R_e} G_{R_e} N_{R_1} N_{R_2} \epsilon_R \\
&+ n_f^2 K_0 k_B T_{e0} \Sigma_e \\
&+ n_f^2 K_0 \sum_\beta \Bigg\{ \frac{M_e M_\beta}{(M_e+M_\beta)^2} N_e N_\beta \epsilon_{e\beta} \\
&\quad \times \left[m_i u_B^2 M_\beta (V_e - V_\beta)^2 - 3 k_B T_{e0} \left(\gamma_e^{-1} - \gamma_\beta^{-1} \right) \right] \Bigg\} \\
\left(\tfrac{3}{2}+g_e\right) \Gamma_e \frac{\gamma_e'}{\gamma_e^2} = &\gamma_e^{-1} \Gamma_e' \\
&- \gamma_e^{-1} V_e N_e' \\
&+ Q' \\
&- \left(\frac{m_i u_B^2}{k_B T_{e0}} \tfrac{1}{2} M_e V_e^2 - \tfrac{3}{2} \gamma_\alpha^{-1} \right) \sum_{R_e} G_{R_e} N_{R_1} N_{R_2} \epsilon_R \\
&- \Sigma_e \\
&- \sum_\beta \Bigg\{ \frac{M_e M_\beta}{(M_e+M_\beta)^2} N_e N_\beta \epsilon_{e\beta} \\
&\quad \times \left[\frac{m_i u_B^2}{k_B T_{e0}} M_\beta (V_e - V_\beta)^2 - 3 \left(\gamma_e^{-1} - \gamma_\beta^{-1} \right) \right] \Bigg\}
\end{aligned}
$$

$$
\begin{aligned}
\left(\tfrac{3}{2}+g_e\right)\Gamma_e\frac{\gamma_e'}{\gamma_e^2} =& \frac{\Gamma_e'}{\gamma_e}-\frac{\Gamma_e}{\gamma_e}\frac{N_e'}{N_e}+Q'-\Sigma_e \\
&-\left(\tfrac{1}{2}M_e\frac{\Gamma_e^2}{N_e^2}-\tfrac{3}{2}\gamma_e^{-1}\right)\sum_{R_e}G_{R_e}N_{R_1}N_{R_2}\epsilon_R \\
&-\sum_\beta\left\{\frac{M_eM_\beta}{\left(M_e+M_\beta\right)^2}\epsilon_{e\beta}\left[M_\beta\frac{\left(N_\beta\Gamma_e-N_e\Gamma_\beta\right)^2}{N_eN_\beta}\right.\right. \\
&\left.\left.-3N_eN_\beta\left(\gamma_e^{-1}-\gamma_\beta^{-1}\right)\right]\right\}
\end{aligned}
\tag{4.8}
$$

From (4.5), the expression for the electron heat flux gradient:

$$
\begin{aligned}
\boldsymbol{\nabla}\cdot\boldsymbol{q} =& -\left(\tfrac{5}{2}-g_e\right)k_B^2\frac{n_eT_e}{m_e\nu_{eg}}\boldsymbol{\nabla}^2T_e \\
&-\left(\tfrac{5}{2}-g_e\right)k_B^2\frac{T_e}{m_e\nu_{eg}}\boldsymbol{\nabla}T_e\boldsymbol{\nabla}n_e \\
&-k_Bg_en_e\boldsymbol{u}_e\boldsymbol{\nabla}T_e \\
&-\left[\left(1-g_e\right)\left(\tfrac{5}{2}-g_e\right)-T_e\frac{\mathrm{d}g_e}{\mathrm{d}T_e}\right]k_B^2\frac{n_e}{m_e\nu_{eg}}\left(\boldsymbol{\nabla}T_e\right)^2 \\
&-k_Bg_eT_e\boldsymbol{\nabla}\left(n_e\boldsymbol{u}_e\right) \\
&-k_Bn_e\boldsymbol{u}_eT_e\frac{\mathrm{d}g_e}{\mathrm{d}T_e}\boldsymbol{\nabla}T_e \\
n_fu_Bk_BT_{e0}\frac{n_fK_0}{u_B}Q' =& -\frac{k_B^2n_fT_{e0}}{m_in_fK_0}\frac{n_f^2K_0^2}{u_B^2}T_{e0}\left(\tfrac{5}{2}-g_e\right)\frac{N_e}{M_eN_g\epsilon_{eg}\gamma_e}\frac{T_e''}{T_{e0}} \\
&-\frac{k_B^2n_fT_{e0}}{m_in_fK_0}\frac{n_f^2K_0^2}{u_B^2}T_{e0}\left(\tfrac{5}{2}-g_e\right)\frac{1}{M_eN_g\epsilon_{eg}\gamma_e}\frac{T_e'}{T_{e0}}N_e' \\
&-k_Bn_fu_B\frac{n_fK_0}{u_B}T_{e0}g_e\Gamma_e\frac{T_e'}{T_{e0}} \\
&-\frac{k_B^2n_f}{m_in_fK_0}\frac{n_f^2K_0^2}{u_B^2}T_{e0}^2 \\
&\quad\times\left[\left(1-g_e\right)\left(\tfrac{5}{2}-g_e\right)-T_e\frac{\mathrm{d}g_e}{\mathrm{d}T_e}\right]\frac{N_e}{M_eN_g\epsilon_{eg}}\left(\frac{T_e'}{T_{e0}}\right)^2 \\
&-k_BT_{e0}\frac{n_fK_0}{u_B}n_fu_Bg_e\gamma_e^{-1}\Gamma_e' \\
&-k_BT_{e0}\frac{n_fK_0}{u_B}n_fu_B\Gamma_e\left(T_e\frac{\mathrm{d}g_e}{\mathrm{d}T_e}\right)\frac{T_e'}{T_{e0}}
\end{aligned}
$$

$$
\begin{aligned}
Q' = &- \frac{k_B T_{e0}}{m_i u_B^2} \left(\tfrac{5}{2} - g_e\right) \frac{N_e}{M_e N_g \epsilon_{eg} \gamma_e} \frac{T_e''}{T_{e0}} \\
&- \frac{k_B T_{e0}}{m_i u_B^2} \left(\tfrac{5}{2} - g_e\right) \frac{1}{M_e N_g \epsilon_{eg} \gamma_e} \frac{T_e'}{T_{e0}} N_e' \\
&- g_e \Gamma_e \frac{T_e'}{T_{e0}} \\
&- \frac{k_B T_{e0}}{m_i u_B^2} \left[(1 - g_e)\left(\tfrac{5}{2} - g_e\right) - T_e \frac{\mathrm{d}g_e}{\mathrm{d}T_e}\right] \frac{N_e}{M_e N_g \epsilon_{eg}} \left(\frac{T_e'}{T_{e0}}\right)^2 \\
&- g_e \gamma_e^{-1} \Gamma_e' \\
&- \Gamma_e \left(T_e \frac{\mathrm{d}g_e}{\mathrm{d}T_e}\right) \frac{T_e'}{T_{e0}}
\end{aligned}
$$

In the final step to generate (4.9), the following relations are used:

$$
\frac{T_\alpha'}{T_{e0}} = -\frac{\gamma_\alpha'}{\gamma_\alpha^2} \qquad \left(\frac{T_\alpha'}{T_{e0}}\right)^2 = \frac{\gamma_\alpha'^2}{\gamma_\alpha^4} \qquad \frac{T_\alpha''}{T_{e0}} = 2\frac{\gamma_\alpha'^2}{\gamma_\alpha^3} - \frac{\gamma_\alpha''}{\gamma_\alpha^2}
$$

$$
\begin{aligned}
Q' = &\left(\tfrac{5}{2} - g_e\right) \frac{N_e}{M_e N_g \epsilon_{eg}} \frac{\gamma_\alpha''}{\gamma_\alpha^3} - 2\left(\tfrac{5}{2} - g_e\right) \frac{N_e}{M_e N_g \epsilon_{eg}} \frac{\gamma_\alpha'^2}{\gamma_\alpha^4} \\
&+ \left(\tfrac{5}{2} - g_e\right) \frac{1}{M_e N_g \epsilon_{eg}} \frac{\gamma_\alpha'}{\gamma_\alpha^3} N_e' + \left(g_e + T_e \frac{\mathrm{d}g_e}{\mathrm{d}T_e}\right) \Gamma_e \frac{\gamma_\alpha'}{\gamma_\alpha^2} \\
&- \left[(1 - g_e)\left(\tfrac{5}{2} - g_e\right) - T_e \frac{\mathrm{d}g_e}{\mathrm{d}T_e}\right] \frac{N_e}{M_e N_g \epsilon_{eg}} \frac{\gamma_\alpha'^2}{\gamma_\alpha^4} - g_e \frac{\Gamma_e'}{\gamma_e}
\end{aligned}
\tag{4.9}
$$

The equation for the electron energy balance to be used in the model is now found by substituting (4.9) into (4.8). To help control the size of the resulting expression, it is also useful to replace the collection of chemical reactions with the flux gradient, from (4.6). Terms are first collected into those that share derivatives. The resulting expression is then rearranged to provide an equation for γ_e'', given in (4.10).

$$
\begin{aligned}
\left(\tfrac{5}{2} - g_e\right) \frac{N_e}{M_e N_g \epsilon_{eg}} \frac{\gamma_e''}{\gamma_e^3} = &- \left(\tfrac{5}{2} - g_e\right) \frac{1}{M_e N_g \epsilon_{eg}} \frac{\gamma_e'}{\gamma_e^3} N_e' + \Sigma_e \\
&+ \left[(3 - g_e)\left(\tfrac{5}{2} - g_e\right) - T_e \frac{\mathrm{d}g_e}{\mathrm{d}T_e}\right] \frac{N_e}{M_e N_g \epsilon_{eg}} \frac{\gamma_e'^2}{\gamma_e^4} + \frac{\Gamma_e}{\gamma_e} \frac{N_e'}{N_e} \\
&+ \left(\tfrac{3}{2} - T_e \frac{\mathrm{d}g_e}{\mathrm{d}T_e}\right) \Gamma_e \frac{\gamma_e'}{\gamma_e^2} + \left[\tfrac{1}{2} M_e \frac{\Gamma_e^2}{N_e^2} - \left(\tfrac{5}{2} - g_e\right) \gamma_e^{-1}\right] \Gamma_e' \\
&+ \sum_\beta \frac{M_e M_\beta}{(M_e + M_\beta)^2} \epsilon_{e\beta} \left[M_\beta \frac{(N_\beta \Gamma_e - N_e \Gamma_\beta)^2}{N_e N_\beta} - 3 N_e N_\beta \left(\gamma_e^{-1} - \gamma_\beta^{-1}\right)\right]
\end{aligned}
$$

$$\begin{aligned}\gamma_e'' =& -\gamma_e' \frac{N_e'}{N_e} + \left[3 - g_e - \frac{T_e \frac{\mathrm{d}g_e}{\mathrm{d}T_e}}{\frac{5}{2} - g_e}\right] \frac{\gamma_e'^2}{\gamma_e} + \left\{ \frac{M_e \gamma_e N_g \epsilon_{eg}}{\left(\frac{5}{2} - g_e\right) N_e} \right\} \\ &\times \left\{ \Gamma_e \gamma_e \frac{N_e'}{N_e} + \left(\frac{3}{2} - T_e \frac{\mathrm{d}g_e}{\mathrm{d}T_e}\right) \Gamma_e \gamma_e' + \left[\frac{1}{2} M_e \gamma_e \frac{\Gamma_e^2}{N_e^2} - \left(\frac{5}{2} - g_e\right)\right] \gamma_e \Gamma_e' \right. \\ &- \gamma_e^2 \Sigma_e + \gamma_e \sum_\beta \frac{M_e M_\beta}{\left(M_e + M_\beta\right)^2} \epsilon_{e\beta} \left[\gamma_e M_\beta \frac{\left(N_\beta \Gamma_e - N_e \Gamma_\beta\right)^2}{N_e N_\beta} \right. \\ &\left. \left. - 3 N_e N_\beta \left(1 - \frac{\gamma_e}{\gamma_\beta}\right) \right] \right\}\end{aligned} \tag{4.10}$$

Similarly to the previous chapter, (4.6), (4.7) and (4.10) can be build into a system of equations that fully describes the gradients of densities and flux for all species, as well as the second differential of the electron temperature.

In order to perform a numerical integration of this system, a number of modifications must be made. Equations are reformulated again to use the natural logarithm of species densities, as discussed in Section 3.3, and given below in (4.11) to (4.13). As numerical integrators typically deal only with first order differential equations, an additional variable must be included to follow the gradient of γ_e, and the gradient of this new variable is then equal to the right hand side of (4.13).

$$\Gamma_\alpha' = \sum_{R_\alpha} G_{R_\alpha} \epsilon_R \exp\left(L_{R_1} + L_{R_2}\right) \tag{4.11}$$

$$\begin{aligned}L_\alpha' =& \gamma_\alpha Z_\alpha \zeta - \gamma_\alpha M_\alpha \mathrm{e}^{-2L_\alpha} \Gamma_\alpha \Gamma_\alpha' + \left(1 - g_\alpha\right) \frac{\gamma_\alpha'}{\gamma_\alpha} \\ &- \gamma_\alpha \sum_\beta \frac{M_\alpha M_\beta}{M_\alpha + M_\beta} \epsilon_{\alpha\beta} \left[\exp\left(L_\beta - L_\alpha\right) \Gamma_\alpha - \Gamma_\beta\right]\end{aligned} \tag{4.12}$$

$$\begin{aligned}\gamma_e'' =& -\gamma_e' L_e' + \left[3 - g_e - \frac{T_e \frac{\mathrm{d}g_e}{\mathrm{d}T_e}}{\frac{5}{2} - g_e}\right] \frac{\gamma_e'^2}{\gamma_e} + \left\{ \frac{M_e \gamma_e \epsilon_{eg}}{\left(\frac{5}{2} - g_e\right)} \exp\left(L_g - L_e\right) \right\} \\ &\times \left\{ \Gamma_e \gamma_e L_e' + \left(\frac{3}{2} - T_e \frac{\mathrm{d}g_e}{\mathrm{d}T_e}\right) \Gamma_e \gamma_e' + \left[\frac{1}{2} M_e \gamma_e \Gamma_e^2 \mathrm{e}^{-2L_e} - \left(\frac{5}{2} - g_e\right)\right] \gamma_e \Gamma_e' \right. \\ &- \gamma_e^2 \Sigma_e + \gamma_e \sum_\beta \frac{M_e M_\beta}{\left(M_e + M_\beta\right)^2} \epsilon_{e\beta} \left[\gamma_e M_\beta \frac{\left(\mathrm{e}^{L_\beta} \Gamma_e - \mathrm{e}^{L_e} \Gamma_\beta\right)^2}{\exp\left(L_e + L_\beta\right)} \right. \\ &\left. \left. - 3 \exp\left(L_e + L_\beta\right) \left(1 - \frac{\gamma_e}{\gamma_\beta}\right) \right] \right\}\end{aligned} \tag{4.13}$$

4.2 Model Development and Implementation

As in the previous chapter, the equation system developed requires further information and numerical methods to be specified. The additional parameters laid out in

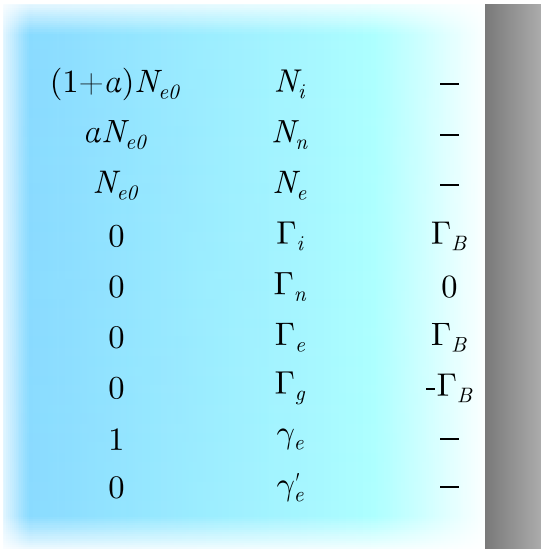

Figure 21: Non-isothermal model boundary conditions. Central plasma conditions are on the left, edge values are on the right.

Section 3.2 are largely unchanged. Boundary conditions are added for γ_e and γ'_e, and two additional reactions are included as they are important electron energy loss pathways.

For the boundary conditions, γ_e must be unity at the centre, due to its definition through the central electron temperature, and symmetry across the discharge must once again be maintained, so the derivative of γ_e should be zero at the centre. There are no particular constraints on the edge values of either the electron temperature coefficient or its gradient. These conditions, and those from before, are summarised in figure 21.

As previously noted, there are some additional parameters that require specification. As the electron temperature is being solved for, all of the important processes that affect it must be considered. This includes energy losses through inelastic collisions and chemical reactions. All of the reactions considered in the isothermal model that take energy from electrons must be included, as well as two additional reactions. Both the excitation of O_2 to $O_2\left(^1\Delta_g\right)$ and the dissociation of the created $O_2\left(^1\Delta_g\right)$ are non-trivial energy sinks for the electrons [115]. Despite the produced species not being solved for, these processes shall be included in the electron energy balance, as discussed later. The reaction set is summarised in table 5.

As in Section 3.2.3, reaction rate coefficients that depend on electron temperature are found using BOLSIG+, and then approximated by a function fitted in logarithmic space, given in (4.14). These rate coefficients are plotted as a function of T_e in

Table 5: O_2 reaction rate coefficients to be used in the non-isothermal model, including the energy loss of any electrons acting as reaction partners. T_g in Kelvin. $f(T_e)$ indicates RRC estimated from function fitted to tabulated data. References are the same as for table 3.

Code	Reaction	RRC (m^3s^{-1})	Energy Loss (eV)
I	$O_2 + e^- \rightarrow O_2^+ + 2e^-$	$f(T_e)$	12.06
IM	$O_2 + e^- \rightarrow O^- + \frac{1}{2}O_2$	$f(T_e)$	4.78
EN*	$O_2^+ + e^- \rightarrow O_2$	$f(T_e)$	T_e
ED	$O^- + e^- \rightarrow \frac{1}{2}O_2 + 2e^-$	$f(T_e)$	1.56
SI	$O_2\left(^1\Delta_g\right) + e^- \rightarrow O_2^+ + 2e^-$	$f(T_e)$	11.08
SB	$O_2\left(^1\Delta_g\right) + e^- \rightarrow O^- + \frac{1}{2}O_2$	$f(T_e)$	3.5
MN	$O_2^+ + O^- \rightarrow O_2 + \frac{1}{2}O_2$	$2 \times 10^{-13}\left(\frac{300}{T_g}\right)$	—
SD	$O_2\left(^1\Delta_g\right) + O^- \rightarrow O_2 + \frac{1}{2}O_2 + e^-$	$3 \times 10^{-16}\left(\frac{T_g}{300}\right)^{0.5}$	—
SDO†	$O_2 + e^- \rightarrow O_2\left(^1\Delta_g\right) + e^-$	$f(T_e)$	0.977
SA†	$O_2\left(^1\Delta_g\right) + e^- \rightarrow 2 \times \frac{1}{2}O_2 + e^-$	$f(T_e)$	5.02
eg	$O_2 + e^- \rightarrow O_2 + e^-$	$f(T_e)$	0
ig	$O_2 + O_2^+ \rightarrow O_2 + O_2^+$	$1 \times 10^{-15}\left(\frac{T_g}{300}\right)^{0.5}$	—
ng	$O_2 + O^- \rightarrow O_2 + O^-$	2×10^{-15}	—

* Recombination to excited state and subsequent de-excitation is considered but not explicitly included.
† Used only in calculating electron energy loss [117].

figure 22(a), and the coefficients that result from the fitting in logarithmic space are given in table 6.

$$K_R = \exp\left[\sum_{n=1}^{9} a_{R,n} \ln(T_e)^{n-1}\right] \tag{4.14}$$

The form of (4.14) has the property of being differentiable, which makes it simple to find an expression for the elastic collision frequency gradient coefficient, discussed in Section 2.4.5, and given as $g_e \approx T_e/K_{eg} \times \mathrm{d}K_{eg}/\mathrm{d}T_e$, as shown in (4.15).

$$\begin{aligned} g_e &\approx \frac{T_e}{K_{eg}} \frac{\mathrm{d}K_{eg}}{\mathrm{d}T_e} \\ &= T_e \frac{\mathrm{d}\ln K_{eg}}{\mathrm{d}T_e} \\ &= T_e \frac{\mathrm{d}}{\mathrm{d}T_e}\left[\sum_{n=1}^{9} a_{eg,n} \ln(T_e)^{n-1}\right] \\ &= T_e\left[T_e^{-1} \sum_{n=1}^{9} (n-1) a_{eg,n} \ln(T_e)^{n-2}\right] \\ g_e &= \sum_{n=1}^{8} n a_{eg,n+1} \ln(T_e)^{n-1} \end{aligned} \tag{4.15}$$

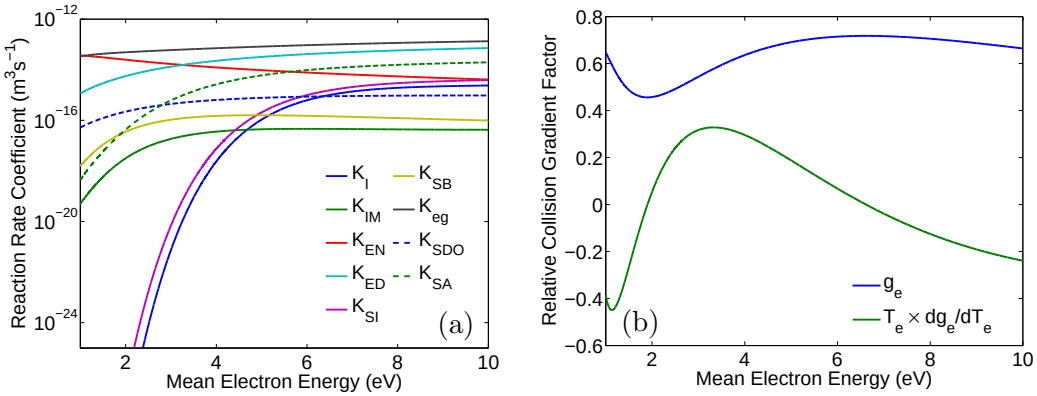

Figure 22: Dependence on electron temperature of (a) reaction rate coefficients and (b) elastic collision gradient factors.

The differentiation can be continued to provide an expression for the relative energy derivative of g_e, which appears in (4.13) as $T_e \frac{\mathrm{d}g_e}{\mathrm{d}T_e}$, as provided in (4.16).

$$\begin{aligned} T_e \frac{\mathrm{d}g_e}{\mathrm{d}T_e} &= T_e \frac{\mathrm{d}}{\mathrm{d}T_e} \left[\sum_{n=1}^{8} n a_{eg,n+1} \ln\left(T_e\right)^{n-1} \right] \\ &= T_e \left[T_e^{-1} \sum_{n=1}^{8} (n-1) n a_{eg,n+1} \ln\left(T_e\right)^{n-2} \right] \\ T_e \frac{\mathrm{d}g_e}{\mathrm{d}T_e} &= \sum_{n=1}^{7} n(n+1) a_{eg,n+2} \ln\left(T_e\right)^{n-1} \end{aligned} \tag{4.16}$$

These two dimensionless factors are given in figure 22(b). Both g_e and $T_e \frac{\mathrm{d}g_e}{\mathrm{d}T_e}$ can be seen to be of order unity. Therefore, as they appear in (4.12) and (4.13) as modifiers to coefficients just over unity, their effect is clearly non-negligible, and terms containing them can be changed in magnitude by tens of percent, depending on the conditions. These factors are often neglected in the development of plasma models, and so comparisons of this work with other models are expected to show differences of a few percent due to this discrepancy.

The last additional parameter to consider is the net power deposition into the electrons, appearing as Σ_e in (4.13). This has to account for both the ohmic power deposition from the RF excitation and the energy losses through collisions.

Beginning with the RF power deposition, it is possible to express a total power deposition for a given plasma, and so too an average volumetric power deposition. However it is known that the power deposition varies in space [27], so a single value for the whole discharge is unrealistic. The current density in the plasma over time is well described by a sinusoidal function $j_0 \sin(\omega t)$, with amplitude j_0. As the total

Table 6: Fitting coefficients $a_{R,n}$ from (4.14) for reactions that are a function of T_e, given to 5 significant figures.

Code	n								
	1	2	3	4	5	6	7	8	9
I	-0.047732	0.93623	-7.2361	27.384	-49.657	30.313	4.9540	36.203	-95.053
IM	-0.0060283	0.11377	-0.82932	2.851	-4.2799	1.1865	0.76977	5.7634	-44.443
EN	0.00056304	-0.011162	0.087716	-0.34414	0.68838	-0.57155	-0.25464	-0.27301	-30.937
ED	-0.00057099	0.012191	-0.10469	0.45519	-1.0201	1.0269	-0.54625	2.4233	-34.404
SI	-0.035885	0.69742	-5.3128	19.589	-33.475	15.708	6.6035	36.267	-89.567
SB	-0.0014788	0.025949	-0.16598	0.40976	0.08844	-1.8681	0.73798	4.7871	-40.999
SDO	-0.00093892	0.018877	-0.1502	0.58968	-1.1291	0.80334	-0.32208	2.1916	-37.504
SA	-0.005622	0.11432	-0.92646	3.7534	-7.6609	6.5417	-1.5338	6.3768	-42.284
eg	0.00046639	-0.0091317	0.06973	-0.25547	0.42606	-0.17783	-0.19301	0.64854	-31.011

current density in the plasma must be conserved, j_0 is constant in both space and time. In reality the current would be comprised of the currents of the various charged species, as well as a displacement current. However in the plasma bulk, and particularly in the parameter range covered by the model, the current is almost exclusively electron current, and so the other terms are neglected. By using the classical power deposition formula, and averaging over time, an expression is found for the time averaged volumetric power deposition as a function of j_0 and the plasma DC conductivity, $\sigma_{DC}(x) = e^2 n_e(x)/(m_e \nu_{eg}(x))$, as given in (4.17) [19, 20].

$$S_e(x) = \bar{S}_{ohm}(x) = \frac{j_0^2}{2\sigma_{DC}(x)} \tag{4.17}$$

As the current density amplitude is constant in space and time, j_0 can be specified as a control parameter for the model to describe the total power being deposited into the electrons, with a self consistent spatial variation arising from the dependence of σ_{DC} on the electron density and electron-neutral elastic collision rate.

To find a value for the normalised power deposition, $\Sigma_{e,P}$, the following steps are taken.

$$\begin{aligned} \Sigma_{e,P}(x) &= \frac{S_e(x)}{n_f^2 K_0 k_B T_{e0}} \\ &= \frac{1}{2} \frac{j_0^2 m_e}{e^2 n_f^2 k_B T_{e0}} \frac{n_g K_{eg}(x)}{n_e(x) K_0} \end{aligned} \tag{4.18}$$

$$\Sigma_{e,P}(x) = J_0^2 \frac{N_g \epsilon_{eg}(x)}{N_e(x)} \tag{4.19}$$

$$J_0^2 = \frac{j_0^2 m_e}{2e^2 n_f^2 k_B T_{e0}} \tag{4.20}$$

In (4.20), J_0^2 is no longer a true representation of current density, as normalisation factors have been moved between quantities in the intermediate steps. It can be interpreted as the ratio between a measure of the electron streaming kinetic energy $j_0^2 m_e/(2e^2 n_f^2)$ and the central electron thermal energy $k_B T_{e0}$. This would mean that (4.19) translates to a conversion from one to the other, at a rate determined by the elastic collision term, as could be expected from an ohmic heating mechanism.

The volumetric rate of energy loss through inelastic collisions, $\Sigma_{e,I}$, is also included in Σ_e, and so needs to be found. The volumetric rate of energy loss through a given reaction is simply the volumetric reaction rate multiplied by the energy lost taken from table 5. The total loss rate $\Sigma_{e,I}$ is then the summation of all of these individual rates, as given in (4.21), where $\mathcal{E}_R$ is the energy loss of reaction R from table 5. The net

volumetric rate of change in electron energy from external sources follows trivially as $\Sigma_e = \Sigma_{e,P} - \Sigma_{e,I}$.

$$\Sigma_{e,I} = \sum_{R_e} \frac{\mathcal{E}_R}{k_B T_{e0}} \epsilon_R N_{R,1} N_e \tag{4.21}$$

The numerical methods to be used are unchanged from the isothermal model; the only difference from the perspective of the integration routine is the addition of two variables in the scheme. As neither γ_e nor γ_e' have a direct association with the edge boundary conditions, the numerical routines used are not affected by their inclusion, and all of the information supplied in Section 3.3 also applies here. Implementation of the new equation set is then trivial compared with that for the isothermal model, as it simply requires the modification of existing code to include the new variables.

4.3 Results

As before, investigation of the model will begin with the analysis of the output of a single set of initial conditions, chosen to be similar to a real oxygen CCP [125, 139]. As some systems are characterised by absolute power, and some by current, (4.19) is used to convert between central values of $\Sigma_{e,P}$ and J_0^2.

4.3.1 Typical Conditions

Figure 23(a) shows the charged species densities for a typical discharge, where particularly apparent is the transition between the bulk region and the presheath. This can also be seen in the fluxes, given in figure 23(b), which additionally give a clear visual indication of the current and particle flux conservations that result from the equation set. The steady increase of T_e through the discharge is shown in figure 23(c), as is the spatially resolved ionisation rate. These three plots together show how the system behaviour is affected by the sharp dependence of, in particular, K_I on T_e in this energy range. As T_e increases, reaction rate coefficients alter rapidly due to their individual nonlinear trends, and species behaviour can change quickly in space. This is the cause of the sudden transition into a presheath. Close to the edge, the dropping electron density almost causes a turnover in the ionisation rate, despite the continued increase in T_e. In a physical system, T_e would reach a peak just inside the sheath, then tend toward zero as one approaches the wall. However the lack of sheath in this model means that if one were to continue the integration beyond the Bohm criterion, T_e would keep increasing, as the relationship of deposited power with N_e^{-1} means both

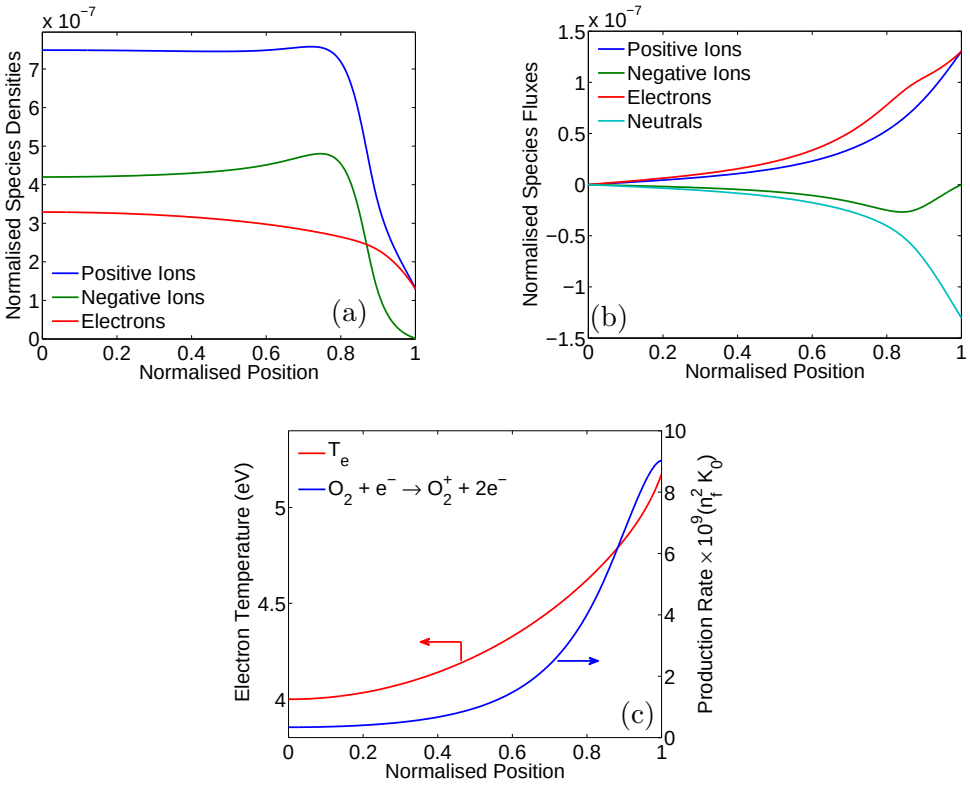

Figure 23: Example spatial profiles from the non-isothermal model for $T_e = 4\,\text{eV}$, $N_{e0} = 3.3 \times 10^{-7}$, and $J_0^2 = 3.06 \times 10^{-15}$. Given are (a) charged species densities, (b) species fluxes, and (c) the electron temperature with the primary production rate for positive ions.

become singular as $N_e \to 0$.

It is known that there is a link between the volumetric power being deposited into a plasma, and the resulting electron density [19, 20]. Equations in simple global models can determine the plasma density through a relationship between the volumetric power density and the system geometry. However, the assumptions used to obtain this relationship are not valid in this context, and so the corresponding link in the normalised system described by the model developed here is not as trivial to uncover. As the geometry of the model is not fully realised before the numerical integration is complete, it is not possible to obtain a similar simple relationship, but it is still possible to investigate the links between the two.

The unit system described in (4.18) can be split into an energy ($k_B T_{e0}$) density (n_f) per unit time ($n_f K_0$), as to be expected from a volumetric power deposition. If two discharges have differing geometries, for example two non-infinite planar discharges with different electrode areas, but the same plasma parameters (n_{e0}, T_{e0} etc.) then one would expect that the volumetric power density would remain the same. In the region of low density in the isothermal model, the electron density can increase without other

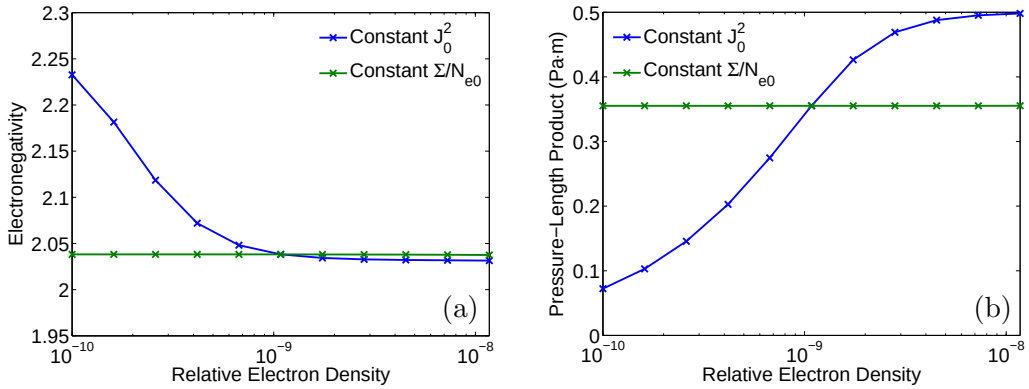

Figure 24: Effect of a constant current density compared with a constant energy deposition rate per electron. Plots show (a) electronegativity and (b) pressure-length product as a function of electron density for each of the two cases.

plasma parameters changing, as shown in figure 17. In this sort of situation, one would expect the volumetric power deposition rate to increase with the electron density, as all energy losses from the system would also grow. It is not unreasonable then to expect that the energy deposition rate *per electron* would be similar across a range of densities.

If one estimates the normalised energy deposition rate per electron for the example case [125, 139] one finds an answer close to unity, implying that in the normalised system of units $\Sigma_{e,P} \approx N_{e0}$, which would mean that each electron receives one unit of energy $(k_B T_e)$ per unit of time $(n_f K_0)$. To investigate this, a number of model runs were performed at low plasma density $(1 \times 10^{-10}$ to $3 \times 10^{-9})$and a constant electron temperature of 4.5 eV. The input current density was either calculated using $\Sigma_{e,P} = N_{e0}$ and (4.19), or kept constant at 3.07×10^{-20}, which is the value found through $\Sigma_{e,P} = N_{e0}$ at the central data point.

As shown in figure 24, there are changes in plasma parameters for a constant current density, but only imperceptible differences if the energy per electron is kept the same. This indicates that if one wishes to perform an investigation in the parameter space $\left(T_{e0}, N_{e0}, J_0^2\right)$, then in order to isolate the effect of changing the current density, one must ensure that the power per electron remains constant by using (4.19). A base case current density J_{base}^2 can be found by setting $\Sigma_{e,P} = N_{e0}$, which results in (4.22), giving the base current density as a function of relative electron density and central electron temperature (via ϵ_{eg}).

$$J_{base}^2 = \frac{N_{e0}^2}{\epsilon_{eg,0} N_{g0}} \tag{4.22}$$

4.3.2 Multiple Inputs

In the previous chapter, it was identified that there are certain distinct regions of behaviour in the parameter space of electron temperature and density. It is hypothesised that these regions will still exist, as their underlying causes are still present. To ascertain this, the model was run with various combinations of high or low T_{e0} and N_{e0}, with $J_0^2 = J_{base}^2$. To investigate the effect of altering the current density, each of these runs was then repeated with J_{base}^2 multiplied by either 0.5 or 5. The results of these runs are shown in figures 25 to 27.

Upon inspection of these figures, it is reassuring to see that the differentiation between the 'structured' and 'unstructured' discharges is still present. There is a clear difference in the density profiles presented in figure 25 between those with a high or low T_{e0}. However, like that shown in figure 23(a), the 'unstructured' plasmas with a low T_{e0} now exhibit a clear peak in the ion densities at the edge of a bulk region. These density peaks have been seen in experiment [127], and were shown to be more pronounced at higher pressures, and therefore lower electron temperatures. As discussed above, this is due to the nonlinear behaviour of reaction rate coefficients with electron temperature.

As well as the same change in behaviour between high and low values of T_{e0} that is exhibited in the isothermal model, there is also still the same lack of effect from changing N_{e0}. The electron density in figure 25(h) is three orders of magnitude higher than that in figure 25(e), but the results appear identical unless one looks at the axes. The effect of changing the current density again has a marked difference between systems with a high or low electron temperature. At a high T_{e0}, the effect of altering J_0^2 on the behaviour of the densities is insignificant. At the low electron temperature, the effect of increasing the system current density is to increase the degree of nonlinearity, increasing the height of the density peak and making the transition between bulk and presheath more severe. However the visible changes are mostly limited to the downstream region of the plasma; the electronegativity is only strongly affected by very high values of current density, as shown in figure 24(a).

The effects of parameter changes on the species fluxes are even less remarkable than those on the densities. Aside from the same transition from unstructured to structured that was seen in the isothermal model, the only noticeable difference between the plots shown in figure 26 is a slight increase in the magnitude of fluxes at the system edge at higher current densities.

Turning to the plots of electron temperature and ionisation rate shown in figure 27,

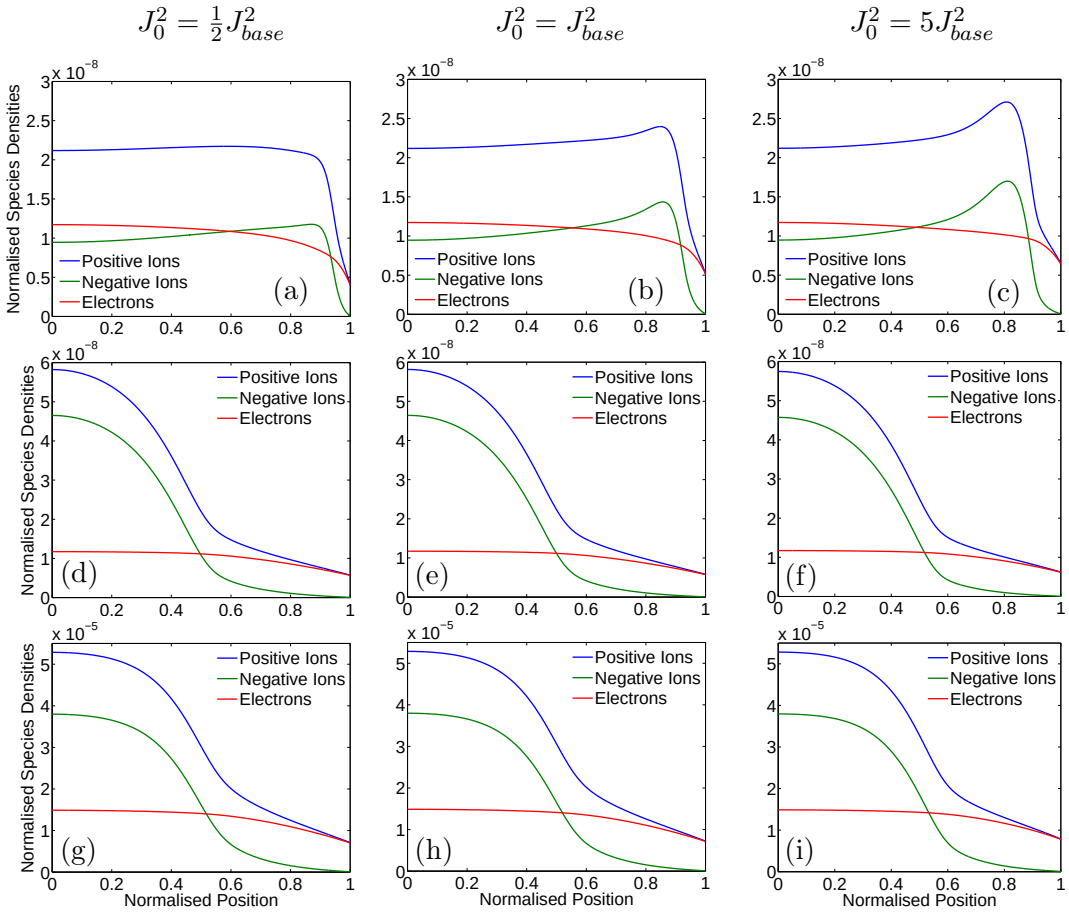

Figure 25: Density profiles that result from the non-isothermal model with various combinations of central electron temperature, electron density, and current density. $T_{e0} = 3.5\,\text{eV}$ for (a) – (c) and $5\,\text{eV}$ for (d) – (i). $N_{e0} = 1.17 \times 10^{-8}$ for (a) – (f) and 1.49×10^{-5} for (g) – (i). Current density is the same for each column of graphs, and is given above the first row.

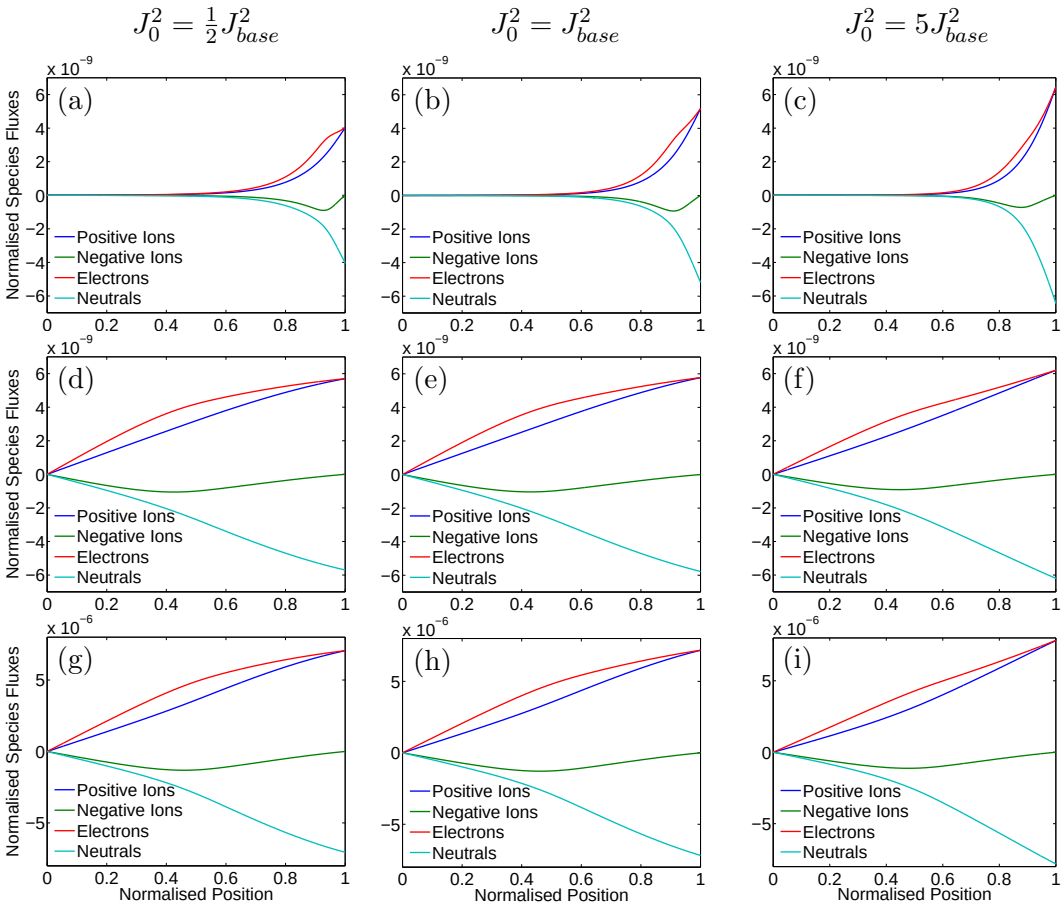

Figure 26: Spatial profiles of species fluxes given by the non-isothermal model for the same conditions as given in figure 25.

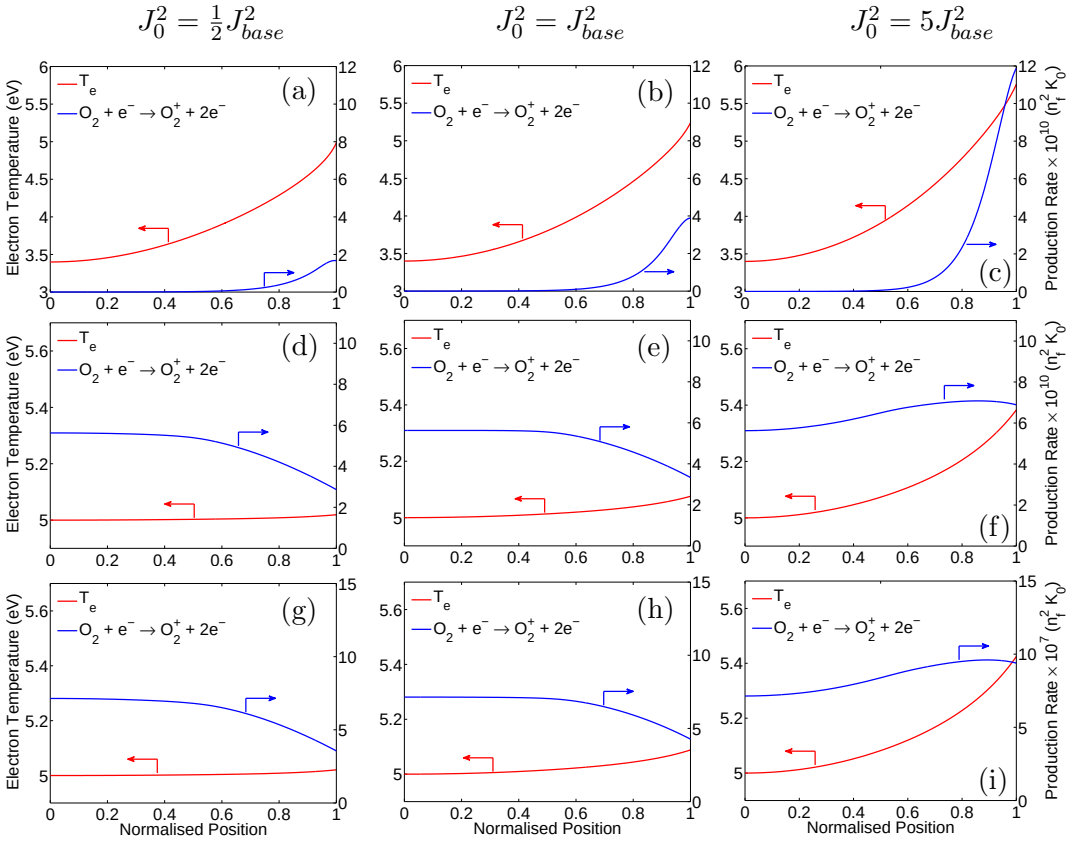

Figure 27: Behaviour of electron temperature and demonstration of non-trivial reaction rate profiles generated by the non-isothermal model, for the same conditions as given in figure 25.

one can find a reason for the lack of interesting behaviour that results from a change to the current density at high T_{e0}. In figures 27(d) to (i) the electron temperature varies only slightly across the whole plasma, by a maximum of around 0.4 eV at the higher current densities. This is contrasted with the behaviour at a low T_{e0}, where T_e increases by a few eV across the discharge. Due to this large change in electron temperature, the reaction rate coefficients change dramatically, as discussed above.

The behaviours of the reaction rates are also changed the most by increasing the current density, where the slight increase in T_e compounds with the higher plasma density towards the edge resulting in, for example, a dramatically increased ionisation rate, as shown in figures 27(a) to (c). Looking at the behaviours at high T_{e0}, the high electron temperature at the centre of the discharge means that not only is the ionisation reaction rate coefficient already high, but the dependence of it on T_e is reduced, as can be deduced from figure 22(a). As a result of this, the modest increase in electron temperature across the discharge is unable to compete with the corresponding drop in electron density, and so, at $J_0^2 = J_{base}^2$ and below, the ionisation rate actually drops between the centre and edge of the system. Increasing the current density does combat this effect to some degree, and there is a net increase in ionisation rate, but the difference is too small to make noticeable changes to the plasma behaviour. It is interesting to observe that despite the radically different initial conditions of the systems demonstrated, the edge value of T_e is comparable among all of them, between 5 eV and 5.5 eV.

One property that is affected by the current density is the system pressure-length product, as demonstrated in figure 24(b). It was found that increasing the current density above J_{base}^2 causes the value for $p \cdot L$ to decrease, more so for low values of T_{e0} but still observable for high electron temperatures. This can be simply explained by the increase in resulting energy deposition rate causing the electron temperature gradient to increase, which causes all of the changes to the reaction rate coefficients and other subsequent effects to occur sooner in the spatial coordinate. This results in the integration terminating sooner in space, and so a narrower discharge is reported.

From an overall perspective, the effect of a high central electron temperature is to reduce the steepness of gradients and generally create calmer spatial profiles. Decreasing T_{e0} or increasing the current density, causes properties to change more suddenly in space. These sudden changes, evident particularly in the density peaks in figures 25(a) to (c), increase the sensitivity of the model to the initial conditions, and cause the re-

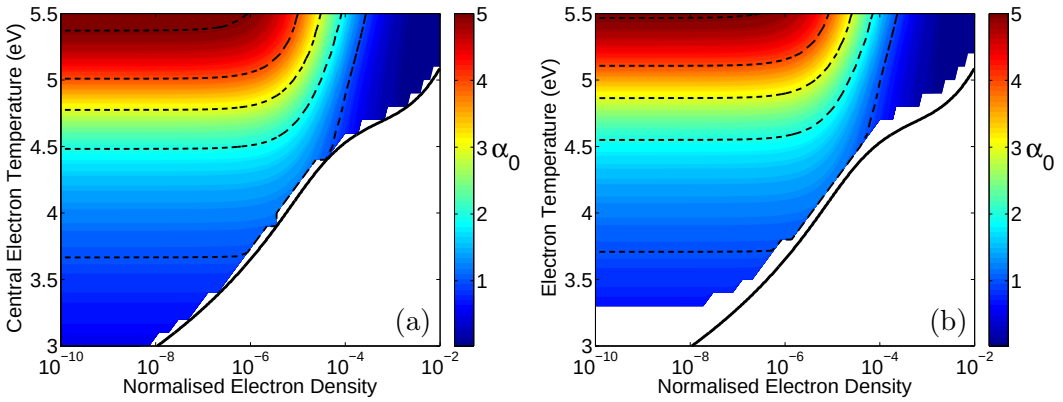

Figure 28: Behaviour of electronegativity as a function of electron density and temperature for (a) the non-isothermal model and (b) the isothermal model, including the limit of theoretical validity discussed Chapter 3. Dashed contours are shown at integer values of α_0 for clarity.

quirement of perturbations. However, the gradients, and therefore the sensitivity, are reduced when compared to the isothermal model. Comparing the gradients of fluxes in figure 14(a) to those in figures 26(a) to (c) it is clear that the spatial profiles in the non-isothermal model are less prone to sudden changes in direction, due to the high values of T_e toward the edge of the system. This should improve the numerical issues that the isothermal model struggled with at lower electron temperatures. This question, and others, can be answered by executing a parameter sweep comparable to that performed for the isothermal model.

4.3.3 Parameter Sweep

Whilst computing the parameter sweep, it was noted that the new model generally produces results faster than the isothermal model. Across the same parameter range as given in figure 17, the average computation time was 22.4 seconds, compared with 60.4 seconds for the isothermal model. There was also significantly less variation in computation time, which indicates that there were less model runs requiring perturbations. This can be seen to be true in figure 28, which shows equivalent parameter sweeps from both the new and isothermal models. In the non-isothermal model, the model is able to provide data for central electron temperatures lower than that accessible by the isothermal model, and this only with a small number of perturbations.

Aside from this obvious difference, there are a couple of other disparities between the two models picked out by figure 28. The first, also related to numerical effects, is that results are able to generated much closer to the theoretical limit of validity. Some of the reportedly valid points in parameter space even lie on the ‘wrong’ side of the

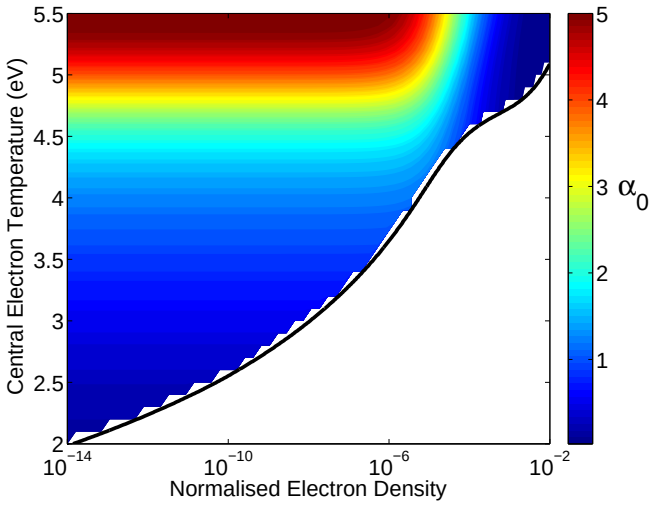

Figure 29: Behaviour of central electronegativity as a function of electron density and temperature, demonstrated over a larger range of parameter space than was possible with the isothermal model.

theoretical limit, though this is most likely a discretisation error creating disparities between the theoretical and integral solutions, as discussed in Section 3.4.3. This new ability of the non-isothermal model is due, again, to the increased stability of the integration caused by the high edge values of T_e. As mentioned in the previous section, the electron temperature reaches a similar edge value regardless of the central values T_e or N_e. This is true across the whole of the parameter space given in figure 28(a), with the edge temperature always falling between 4.93 eV and 5.23 eV, and so the stability of each model is similar.

The other difference between the two models' results is that, for the same central electron temperature, the electronegativity is consistently slightly higher in the non-isothermal model. This small difference is clearer to see if one looks at where the contour lines, plotted at integer intervals, intersect the axes. This can be understood in terms of how the electron temperature affects the negative ion flux across the discharge, and the interplay between the central electronegativity and the edge negative ion flux. Looking at the results for the isothermal model, it can be deduced that for a higher electron temperature, the resulting value of $\Gamma_{n,L}$ is higher, and so the electronegativity is increased to return it toward zero (see figure 9 for the inverse relationship between α_0 and $\Gamma_{n,L}$). In the non-isothermal model, the electron temperature increases across the discharge, and so the mean value for T_e is higher than that in the isothermal model. This creates a similar situation to that caused by raising T_e in the isothermal model, and results in an increased central electronegativity through the same relationship

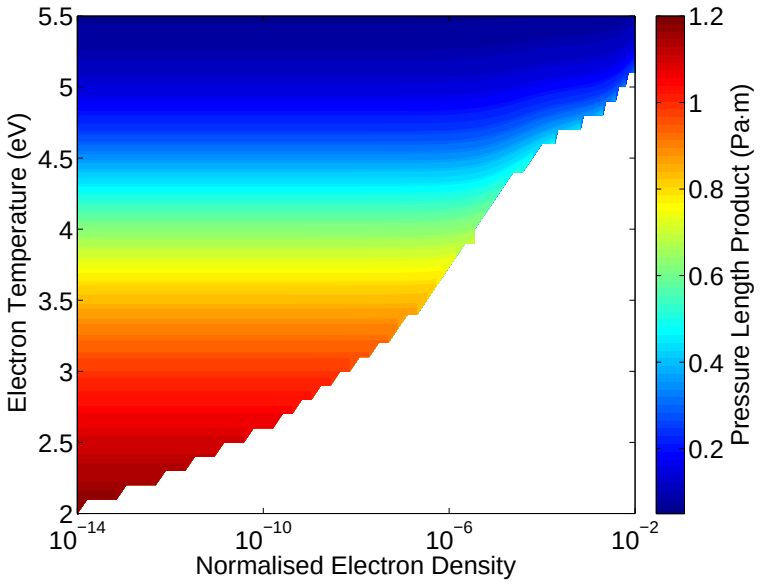

Figure 30: Behaviour of pressure-length product as a function of electron density and temperature given to the non-isothermal model.

between α_0 and $\Gamma_{n,L}$.

As discussed above, the non-isothermal model is able to provide results for lower electron temperatures than the isothermal model. It is thus possible to extend the parameter sweep, which is shown in figure 29. In this new area of parameter space, the plasma density is so low as to render any changes to N_{e0} inconsequential. The trends identified previously simply continue, though the theoretical validity limit becomes increasingly more restrictive as the electron temperature drops.

Turning to the system pressure, the behaviour is found to be altered with the addition of non-isothermal electrons. The trends exhibited in figure 30 are the same as those for the isothermal model in figure 19, however at the lower electron temperatures, the pressure-length product obtained is significantly lower. For 3.5 eV, and low electron density, the isothermal model gave a pressure-length product of around 10 Pa m, whereas in figure 30 it is just below 1 Pa m.

This difference can be attributed to the same effect as is seen when increasing the current density. Namely, the increased electron temperature in the non-isothermal model causes behaviours to occur sooner in the integration, and thus a narrower discharge is obtained.

Despite these differences, the general trends in data are still similar, and so too conform with the community knowledge about pressure-length product and T_e, and power density and n_e, discussed in the previous chapter. With regards to the relation between power density and electron density, in a physical system this is interpreted that

if one changes only the volumetric power deposited in the plasma, then to a first order approximation only the plasma density will change, and not the electron temperature or other properties. As both the electron density and the current density (linked to power deposition via (4.19)) are able to be specified in this model, it is difficult to ascertain whether this relationship applies or not. However, at low densities in figures 29 and 30, a variation in the normalised electron density does not affect anything other than the current density due to the use of J_{base}^2. This effect can also be seen in figure 24, where maintaining $J_0^2 = J_{base}^2$ for different values of N_{e0} changes the power deposition, but in such a way as to keep other behaviours the same. Therefore the relationship of an approximately linear dependence of plasma density on volumetric power deposition [19] can be inferred.

4.3.4 Comparisons

The data in figure 20(b) taken from the full fluid model described in Appendix A are again used to compare the results of this semi-analytical model with a more detailed model. This is done to see how the neglection of time dependencies, sheath effects, and wall properties affect the model. It is known that wall interactions play a significant role in oxygen plasmas [140], particularly for the dynamics of $O_2\left(^1\Delta_g\right)$, which takes part in a number of the dominant reactions [115]. It is an important reaction partner for the O^- negative ion, and an additional ionisation pathway for the creation of O_2^+. Therefore of particular interest is how the empirical inclusion of $O_2\left(^1\Delta_g\right)$ in the semi-analytic model compares to the self consistent inclusion in the full fluid model. The time averaged values of central electron temperature (found using (4.23)), relative electron density, and normalised current density were calculated for results from the full fluid model and input to the semi-analytical model. These results were then denormalised, and plotted together in figure 31.

$$\langle T_e \rangle = \frac{\int T_e n_e dt}{\int n_e dt} \tag{4.23}$$

Unlike the conclusion of the previous chapter, there is excellent quantitative and qualitative agreement between the bulk density and temperature profiles of the two models, however the differences in behaviour, due to discrepancies such as the lack of sheath, are clear. The full fluid model can support a deviation from quasineutrality through the solution of Poisson's equation, whereas in the semi-analytical model, the charged particle densities collapse rather than create a net space charge. The full

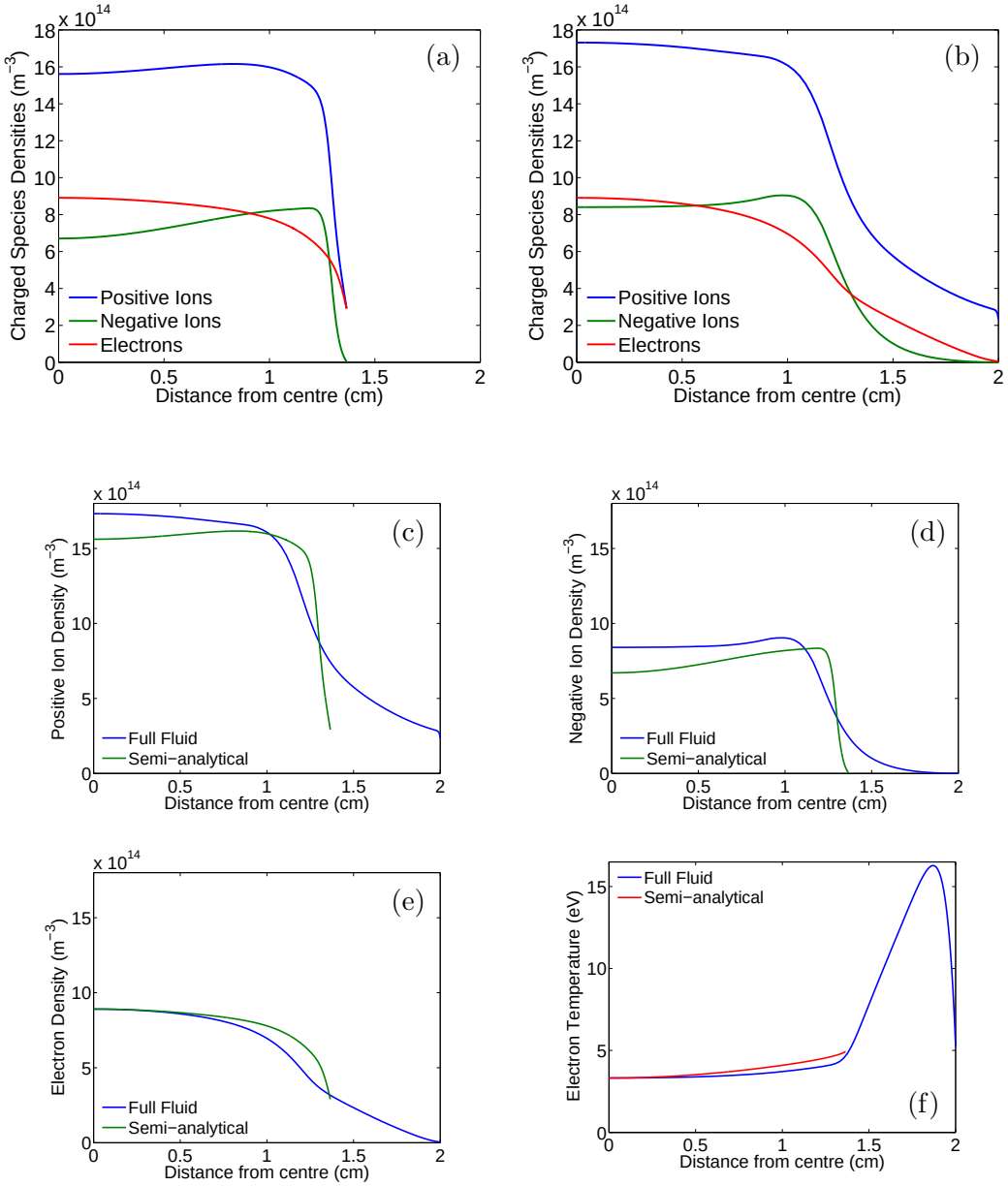

Figure 31: Comparison between density profiles of (a) the semi-analytical and (b) full fluid models for a plasma generated in pure oxygen at 60 Pa, with a central electron temperature of 3.319 eV, between two planar electrodes 4 cm apart. In the full fluid model, these electrodes are supplied from a 300 V_{pp}, 13.56 MHz RF source, and the current density can be calculated as $J_0 = 13.08\,\mathrm{A\,m^{-2}}$. Individual density profiles of (c) positive ions, (d) negative ions, and (e) electrons are overlaid to clarify the similarities between the two models. A comparison of the electron temperature profiles for each model is also given (f).

fluid model transitions smoothly into a sheath, and indeed it is difficult to determine where the bulk ends and sheath begins without a rigorous definition [141], whereas the transition between bulk and sheath is significantly sharper in the semi-analytic model.

Further differences can be seen in the position of the transition, as well as in the exact value of the electronegativity. These can both be explained by differences in not only the spatial profiles but also the time dependencies of power deposition and mean electron energies. Significant temporal modulation of electron temperatures can be seen under certain conditions, due to both ohmic and non-ohmic heating mechanisms [142–144]. This behaviour is not captured in the semi-analytical model, but is in the full fluid model, as can be seen in figure 50 in Appendix A. As some reaction rate coefficients have highly non-linear dependencies on the electron temperature, this modulation in time can have effects on the time averaged behaviour of reaction pathways. As the electronegativity is largely controlled by the balance between creation and destruction mechanisms of negative ions, the inclusion or neglection of these temporal effects will lead to differences in the reported results.

The consideration, or not, of the effect of the spatial gradient of the electron temperature on elastic collisions will also be a source of difference between the two models, as mentioned in Section 4.2. The inclusion of the g_e factor in the semi-analytical model has the effect of altering the downstream behaviour of the density, flux, and temperature profiles, mostly through the terms found in the electron energy transport equation (4.13).

Additionally, as a side effect of the enforcement of quasineutrality, the integration terminates with a smaller spatial extent than the full fluid model. This is fully expected as no sheath can exist in a quasineutral system. One can estimate the true pressure-length product if one has knowledge of the approximate fractional sheath size of the physical system being modelled.

4.4 Conclusions

With regards to the result presented in figure 31, it is clear that although the qualitative and quantitative agreement between the semi-analytical and full fluid models is very good, there are still notable differences. While the spatially dependent power deposition profile included in the semi-analytic model allows, for example, the capture of non-monotonic density profiles, the precise spatial positioning of features differs between the two models. This is due to the neglection of space charges in the semi-analytical

model, and thus the agreement between the two models decreases as one progresses toward the sheath, due to the breakdown of quasineutrality. As convenient as it is to imagine a distinct boundary between the sheath and the plasma bulk, this is not the case in a physical system, and so a gradual degradation in performance is to be expected as the space charge density builds.

Despite these differences, the closeness of the bulk width between the two models is encouraging, as the source of the spatial dimension is different in each model. In the full fluid model, which does not apply any normalisations, the system size is prescribed, and the plasma properties are solved for through the use of a boundary value type solution. In the semi-analytical model the opposite is true, and the system size is one of the outputs.

This order of cause and effect between plasma properties and the physical dimensions of the system may seem incongruous to one who is more familiar with the physical reality of obtaining a discharge within a vessel of a given size. However it is a necessary and important part of the model that has been created, and attempting to constrain the physical dimensions would cause a return to the boundary value type problem, and associated high computation cost that this model is specifically designed to avoid. This order of relations also means that the model is ideal for use in reactor design, as it is typically specific plasma parameters that are desired, and the system geometry that is unknown.

The neglection of the sheath affects the system not only through a change in edge characteristics, but also by preventing the flow of information from any wall interactions back into the bulk, making it impossible to self consistently portray the behaviour of species dominated by wall effects, such as $O_2\left(^1\Delta_g\right)$ [140]. Despite this, figure 31 shows that the bulk is largely unaffected, particularly the value of the electronegativity which is mostly dependent on the reaction set used by the model. The assumption of quasineutrality also forbids the creation of stratified pre-sheath structures (double layers), known to appear under certain conditions [5, 145, 146]. Despite these issues, the assumption of quasineutrality, and thus the removal of Poisson's equation from the system, prevents the creation of a stiff set of differential equations, and thus improves both the model simplicity and computation time dramatically. The improvement in computational performance achieved by discarding Poisson's equation is so great that it is deemed a necessary sacrifice to improve the usefulness of the model.

Some of the inaccuracies introduced by the assumption of quasineutrality may be

able to be alleviated by coupling the model with an analytical or semi-analytical description of an RF sheath. Such models already exist [147–149], and such a coupling has been previously performed [150]. Care would be needed to ensure that the boundary conditions of each model were consistent, but a successful combination of the two models could improve the results obtained, not in the least due to the improvement in the estimation of the spatial extent of the system. It may also allow some form of feedback to occur between the bulk plasma and the wall, introducing the possibility for improved descriptions of species dominated by wall effects.

A further known loss of information comes from the time averaging of equations. It is known that electronegative plasmas exhibit temporal instabilities under certain conditions [6, 125, 151, 152]. The combined loss of stratified pre-sheaths and temporal instabilities may help to explain some of the region where no solutions are possible. As shown in [6, 125, 139] the appearance of instabilities occurs as one increases the plasma power toward the transition to γ-mode, which itself cannot be captured due to the lack of wall interactions. References [139] and [152] also report that instabilities are more frequent at higher pressures. These observations agree with the theoretical prediction of the validity boundary shown in the parameter sweep. This implies that the restrictions on the central ion fluxes that determine the theoretical limit can be worked around if one allows the system to contain oscillations or regions of non-monotonic electric potential. Either of these effects could introduce otherwise disallowed changes to the downstream ion fluxes, relaxing the constraints at the centre. This would explain why a time averaged, quasineutral system is unable to resolve the areas of parameter space that are missing in results such as figure 29.

Overall, the results presented in this chapter indicate that the model created would be well suited for use in helping to understand the properties of electronegative discharges. Due to the ability to specify plasma parameters directly, it is more appropriate for investigations of general properties of planar discharges, or designing a device around a particular plasma, than for modelling a specific device. However, due to the rapid time to solution, it is practicable to perform broad yet detailed investigations of parameter space, from which the behaviour of a given geometry could be extracted.

Some questions still remain, however, that will be addressed in the next chapters. It is not currently clear how the semi-analytical model would compare to a global model; one that is spatially averaged and uses empirical relations to estimate the effect of spatial variation. This sort of model boasts widespread use, but is known to be

less than perfect for systems that do not fit within the limited range of the relations used [145].

It has been shown [14–18] that at high plasma densities, the properties of the neutrals are changed by the presence of the plasma. Therefore one could expect there is a feedback onto the plasma itself due to the subsequent alteration of the interactions between the plasma and neutral species. Including neutral dynamics into the semi-analytical model would allow the investigation of this effect in great detail, and could potentially lead to further understanding of the complexities of electronegative plasmas.

Chapter 5

Global Model

Global models are widely used throughout the plasma physics community, due to their ease of use and rapid generation of results. They can also be comparatively simple to develop and implement. In this chapter, a global model is created that can be used in later comparisons with the semi-analytical model, in order to investigate the differences in performance and accuracy. Trends are compared between the global and semi-analytical models, and the benefits and pitfalls of global models are discussed. Exclusively in this chapter, temperatures appear in equations measured in both Kelvin and eV. They are distinguished by a superscript K or e respectively.

5.1 Global Model Creation

The global model is at its heart still a fluid model, in that it stems from the moments of the Boltzmann equation. However as the name suggests, it involves the removal of all spatial derivatives, and considers only what happens in the bulk and at the sheath boundary. Assumptions are made as to the transport of species from the bulk to the sheath. The inclusion of quasineutrality, as well as the treatment only up to the bulk-sheath boundary, requires that the sheaths are taken to be small and collisionless. Considerations are made for conservation of mass and energy, but as there are no spatial dimensions, the first Boltzmann moment detailing momentum conservation is discarded. The model in this chapter has been developed based on the work of Monahan and Turner [145], which in turn builds on the work of Kim et al. [5, 10] and Monahan [153]. Changes have been made to allow for a different reaction set and reactor parameters.

5.1.1 Derivation

Starting then from the zeroth moment of the Boltzmann equation (2.26), one must balance the creation (and destruction) of species in the bulk with their loss to the walls. This, followed by a division by the plasma volume, gives (5.1).

$$\begin{aligned} V\frac{\partial n_\alpha}{\partial t} &= V\sum_{R_\alpha} G_{R_\alpha} n_{R_1} n_{R_2} K_R - A\left(n_\alpha \boldsymbol{u}_\alpha\right)_L \\ \frac{\partial n_\alpha}{\partial t} &= \sum_{R_\alpha} G_{R_\alpha} n_{R_1} n_{R_2} K_R - \frac{A}{V}\left(n_\alpha \boldsymbol{u}_\alpha\right)_L \end{aligned} \tag{5.1}$$

As mentioned above, the first moment of the Boltzmann equation is not considered here. Thus the next consideration is the balance of energy, where only the most energetic species, the electrons, are considered. In a similar manner to the zeroth moment, the collection of volume processes that involve changes in energy are balanced with the transport of energy to the walls. Starting from (2.36), one discards the spatial derivatives and terms involving flow, and expands the collision term to include total absorbed power (P_{abs}), total power loss through both elastic (P_{el}) and inelastic (P_{inel}) collisions, and the power lost per ion-electron pair to the wall.

$$\frac{3}{2}Vk_B n_e \frac{\partial T_e^K}{\partial t} = V\frac{\delta\left(n\left\langle K\right\rangle\right)}{\delta t} - \frac{3}{2}Vk_B T_e^K \frac{\delta n_e}{\delta t} \tag{5.2}$$

$$\frac{3}{2}Vk_B n_e \frac{\partial T_e^K}{\partial t} = P_{\text{abs}} - P_{\text{el}} - P_{\text{inel}} - A\varepsilon_s\left(n_e \boldsymbol{u}_e\right)_L - \frac{3}{2}Vk_B T_e^K \frac{\delta n_e}{\delta t} \tag{5.3}$$

$$\frac{3}{2}k_B n_e \frac{\partial T_e^K}{\partial t} = S_{\text{abs}} - S_{\text{el}} - S_{\text{inel}} - \frac{A}{V}\varepsilon_s\left(n_e \boldsymbol{u}_e\right)_L - \frac{3}{2}k_B T_e^K \frac{\delta n_e}{\delta t} \tag{5.4}$$

$$\frac{3}{2}\frac{\partial T_e^e}{\partial t} = \frac{S_{\text{abs}}}{en_e} - \frac{S_{\text{colls}}}{en_e} - \frac{A}{V}\frac{\varepsilon_s}{e}\frac{\left(n_e \boldsymbol{u}_e\right)_L}{n_e} \tag{5.5}$$

$$\begin{aligned} S_{\text{colls}} = {} & 3\frac{m_e}{m_i}K_{eg} n_e n_g k_B\left(T_e^K - T_g^K\right) + \sum_{R=1}^{R_e} \mathcal{E}_R K_R n_{R,1} n_e \\ & + \frac{3}{2}k_B T_e^K \sum_{R_\alpha} G_{R_\alpha} n_{R_1} n_{R_2} K_R \end{aligned} \tag{5.6}$$

For clarity, the energy terms associated with collisions have been collected in the volumetric term S_{colls}, and for computational ease, T_e^e is expressed in eV, as denoted by the superscript. The collisional energy losses given in (5.6) are, in order, thermal energy transfer to neutral species through elastic collisions, losses from inelastic collisions where ε_R is the electron energy loss of reaction R, and thermal changes through the addition and removal of electrons due to chemical reactions. In (5.5) the rate of change of T_e^e is the difference between the volumetric power absorption, S_{abs}, and the losses

due to collisions and species lost to the wall. Wall losses are represented by the last term in (5.5), where ε_s is the energy per ion-electron pair that is lost to the wall via the sheath. The magnitude used for this energy loss term is that of Monahan and Turner [145], given in (5.7), where $\bar{V_s}$ is the mean sheath voltage.

$$\varepsilon_s = \left[\frac{\Gamma(\xi_3)\Gamma(\xi_6)}{\Gamma(\xi_5)\Gamma(\xi_4)} + \frac{\Gamma(\xi_3)^2}{\Gamma(\xi_5)\Gamma(\xi_1)}\right]\frac{3}{2}k_B T_e^K + e\bar{V_s} \tag{5.7}$$

In (5.7), $\Gamma(\xi_p)$ is the gamma function of $\xi_p = p/2x$. In this case, x is a value that describes the deviation of the EEDF from a Maxwellian, through the formula given in (5.8) [145, 154].

$$f(\mathcal{E}) = \frac{x}{\left(\frac{3}{2}k_B T_e^K\right)^{3/2}}\frac{\Gamma(\xi_5)^{3/2}}{\Gamma(\xi_3)^{5/2}}\mathcal{E}^{1/2}\exp\left(-\frac{1}{\left(\frac{3}{2}k_B T_e^K\right)^x}\left[\frac{\Gamma(\xi_5)}{\Gamma(\xi_3)}\right]^x \mathcal{E}\right) \tag{5.8}$$

As the model is to describe an RF CCP, the mean sheath voltage, $\bar{V_s}$, is determined from equations derived by Liebermann and Lichtenberg [19] that relate the mean sheath voltage, plasma current density, and volumetric power deposition. By time averaging the expression that determines sheath voltage from the sheath widths in a symmetric CCP, and substituting in a relation for the sheath width and current density, one arrives at (5.9), which gives the sheath voltage in terms of the current density amplitude j_0, electron density, and driving frequency ω.

$$\bar{V_s} = \frac{3}{4}\frac{j_0^2}{e\epsilon_0 n_e \omega^2} \tag{5.9}$$

Using the relation that determines the ohmic power deposition from the current density and plasma conductivity, (5.10), one can then combine (5.9) and (5.10) to arrive at (5.11), an expression for the mean sheath voltage in terms of the ohmic power deposition.

$$S_{\text{ohm}} = \frac{1}{2}j_0^2\frac{m_e\nu_{eg}}{e^2 n_e} \tag{5.10}$$

$$\bar{V_s} = \frac{3}{2}S_{\text{ohm}}\frac{e}{m_e\nu_{eg}\epsilon_0\omega^2} \tag{5.11}$$

In order to determine the wall flux of a particular species, one needs to turn to empirical relations, as without spatial resolution there is no self consistent way of determining all of the species densities at the sheath edge. Similarly to the semi-analytical model, an assumption is made that the negative ion density is zero at the sheath edge, so that $(n_n \boldsymbol{u}_n)_L = 0$. This also has the effect that the positive ion and

electron densities and wall fluxes are equal. If one assumes that the ions leave the system with the Bohm velocity, then only the ion density is needed to specify the edge ion flux.

The sheath edge ion density is often given as a fraction of the central density, such that $n_{i,s} = h_l n_{i,0}$, where the factor of h_l is given by empirical relations or limited approximations. The determination of this factor was first discussed by Godyak and Maksimov [155] for a simple two component plasma. The relations for electronegative plasmas are understandably more complicated than those for the electropositive case. Much research has been conducted on the topic, and Monahan [153] has established an anzatz through the combination of three limited approximations that appears to give good results when compared to a PIC model. The factor used in this work, and the components, are given in (5.12), where the assumption of $T_i = T_n = 300\,\mathrm{K}$ has been made, l_p is the plasma length, and λ_i is the ion mean free path.

$$h_l^2 = h_a^2 + h_b^2 + h_c^2 \tag{5.12a}$$

$$h_a \approx \frac{0.86}{[3 + l_p/\lambda_i]^{1/2}} \frac{1}{1+\alpha_0} \tag{5.12b}$$

$$h_b \approx \left[\left(1 + \frac{1}{\sqrt{2\pi}} \frac{l_p}{\lambda_i} \right) \left(\frac{T_e^K}{T_i^K} \right)^{1/2} \right]^{-1} \frac{\alpha_0}{1+\alpha_0} \tag{5.12c}$$

$$h_c \approx \left[\left(1 + \frac{n_{i,*}^{1/2} n_{i,0}}{n_{n,0}^{3/2}} \right) \left(\frac{T_e^K}{T_i^K} \right)^{1/2} \right]^{-1} \tag{5.12d}$$

$$n_{i,*} = \frac{15}{56} \left(\frac{8 k_B T_i^K}{\pi m_i} \right)^{1/2} \frac{1}{K_{MN} \lambda_i} \tag{5.12e}$$

As the negative ion wall flux is zero, that of both positive ions and electrons can be expressed as a single value, given in (5.13), where n_i is the ion density as calculated by the model.

$$\left(n_{i,e} \boldsymbol{u}_{i,e} \right)_L = h_l n_i u_B \tag{5.13}$$

The final unknown to be found in (5.5) is the plasma surface area to volume ratio. This can be found through simple geometrical considerations, assuming that the system is the same as in the semi-analytical model. For a plasma contained between two square, planar electrodes of side a separated by a distance of b, the volume and surface area are given by the simple relations $V = a^2 b$ and $A = 2a^2 + 4ab$.

$$\frac{A}{V} = \frac{2a^2 + 4ab}{a^2 b}$$

$$
\begin{aligned}
&= \frac{2}{b} + \frac{4}{a} \\
\therefore \lim_{a\to\infty} \left[\frac{A}{V}\right] &= \frac{2}{b} \\
\frac{A}{V} &= \frac{2}{l_p}
\end{aligned} \tag{5.14}
$$

The full set of equations can then be found through the combination of (5.1), (5.5) to (5.7) and (5.11) to (5.14). An important simplification can be made to reduce the number of equations by considering the quasineutrality equation $n_i = n_n + n_e$. As the ion densities can be found from just the electron density and electronegativity, $\alpha = n_n/n_e$, the two ion density equations from (5.1) can be replaced by a single equation for the electronegativity. From the differentiation of $\alpha = n_n/n_e$, one can derive an equation for the rate of change of the electronegativity, given in (5.15).

$$
\begin{aligned}
\frac{\partial \alpha}{\partial t} &= n_e^{-1}\frac{\partial n_n}{\partial t} - \alpha\frac{\partial n_e}{\partial t} \\
\frac{\partial \alpha}{\partial t} &= n_e^{-1}\sum_{R_n} G_{R_n} n_{R_1} n_{R_2} K_R - \alpha \sum_{R_e} G_{R_e} n_{R_1} n_{R_2} K_R + \alpha \frac{A}{V} \left(n_e \boldsymbol{u}_e\right)_L
\end{aligned} \tag{5.15}
$$

Thus the system is described by three differential equations for electronegativity, electron density, and mean electron energy, given in (5.16).

$$
\frac{\partial \alpha}{\partial t} = n_e^{-1}\sum_{R_n} G_{R_n} n_{R_1} n_{R_2} K_R - \alpha \sum_{R_e} G_{R_e} n_{R_1} n_{R_2} K_R + \alpha \frac{A}{V} \left(n_e \boldsymbol{u}_e\right)_L \tag{5.16a}
$$

$$
\frac{\partial n_e}{\partial t} = \sum_{R_e} G_{R_e} n_{R_1} n_{R_2} K_R - \frac{A}{V} \left(n_e \boldsymbol{u}_e\right)_L \tag{5.16b}
$$

$$
\frac{3}{2}\frac{\partial T_e^e}{\partial t} = \frac{S_{\text{abs}}}{e n_e} - \frac{S_{\text{colls}}}{e n_e} - \frac{A}{V}\frac{\varepsilon_s}{e}\frac{\left(n_e \boldsymbol{u}_e\right)_L}{n_e} \tag{5.16c}
$$

These equations can be solved simultaneously with the only inputs, other than estimates of the initial conditions, being the absorbed power density S_{abs}, the plasma length l_p, the neutral gas density n_g, and the reaction rate coefficients, which are the same as those used in Chapter 4. For ease of understanding, the neutral gas density is taken from a supplied pressure-length product.

5.1.2 Solution

The equations for the global model appear simpler than those for the semi-analytical model, but are unfortunately still too complex for an exact analytical solution. The nonlinear combinations of quantities, for example in the expression for collisional energy

losses (5.6), means that it is impossible to separate the variables sufficiently to approach a solution analytically. Thus numerical solutions are required.

In contrast to the semi-analytical model, the evolution of the global model equations over their independent variable is not the end goal. It is the equilibrium point that is of interest, in order to compare with the time averaged solution of the semi-analytical model. This means that a numerical integration scheme is not the only option, but a numerical minimisation could be used to find the point in parameter space where all three time derivatives approach zero. This works well for certain discharge parameters, and is quicker computationally than performing a numerical integration, but fails to provide a solution in some cases. Unfortunately, problems with pre-built numerical minimisation routines are occasionally difficult to diagnose, as the algorithms used are often complex, and the underlying code prioritises efficiency over readability. Thus in these situations it is quicker and easier to gain insight through the use of a simple numerical integration scheme. This was performed using the `ode45` routine in Matlab, which uses a pair of explicit Runge-Kutta formulae for efficient and reasonably accurate solutions (see Section 2.5 for more details). For simplicity across a wide range of discharge parameters, it was decided to use numerical integration for solution of the global model for all situations. The small computation time increase for certain parameters was considered to be a reasonable trade off for the additional insight gained through the exposure of the temporal evolution of parameters.

As is often the case with numerical solutions, it is not possible to reach a true exact equilibrium of the global model through numerical integration. Small scale oscillations are always present, even in systems that in theory should reach an absolute stability, caused by numerical noise from a variety of sources. These can include, but are not limited to, rounding errors due to finite numerical precision, integration overshoot past the point of equilibrium, or nonlinear coupling between the equations. Despite these issues, the model is able to approach an equilibrium with accuracy on the order of 10^{-10} or less.

5.2 Results and Comparisons

In the same manner as for the semi-analytical model, a single run of the global model is investigated first. Values for the pressure-length product and the power deposition are chosen to be within the range that is investigated by the semi-analytical model, and the plasma length is chosen as 4 cm, the same as in the full fluid model. The

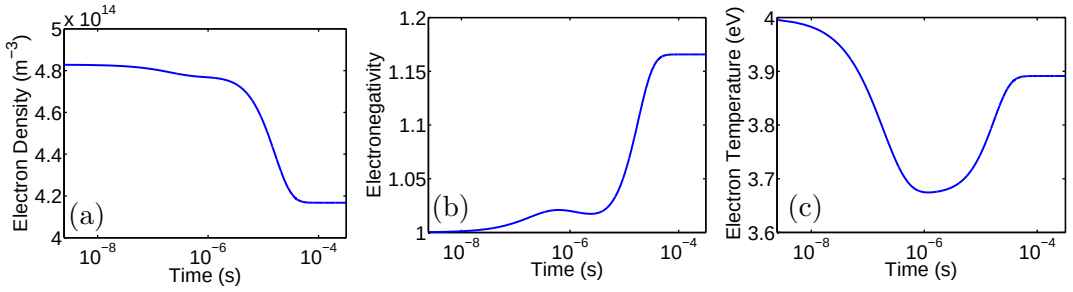

Figure 32: Time dependent outputs for the global model with a pressure-length product of 1 Pa m, plasma length of 4 cm, and power absorption of 1 kW m^{-3}.

input conditions are chosen based roughly on the results of the semi-analytical model, however the point of equilibrium reached by the global model is the same for any reasonable initial conditions.

The time evolution profiles of the three dependent variables are given in figure 32. The logarithmic time axis is to demonstrate that the system undergoes a rapid change in all three parameters, before settling onto a trajectory that takes it to an equilibrium point. Once on this trajectory, the system is comparatively slow (in the independent variable) to converge. Investigation of phase space (n_e, α_0, T_e) shows that for a sensible range of initial conditions ($2\,\text{eV} < Te < 8\,\text{eV}$, $0.1 < \alpha_0 < 5$, $10^{-8} < N_{e0} < 10^{-4}$) the system behaves in the same manner. This indicates that for this set of parameters, there is a stable node in phase space, that is attracting for the range of initial conditions explored. There are small scale oscillations around the equilibrium point, on the order of the accuracy of the integration (10^{-10}). A linearisation about the supposed equilibrium point shows that it is not a true stable node, and that the derivatives of all three parameters are not concurrently zero, so there will always be a small degree of uncertainty. This may also explain why the numerical minimisation routines struggled under certain conditions.

As mentioned, one of the most appealing features of global models, and one of the main drivers behind their widespread use, is the time taken to get results. The data in figure 32 took approximately 0.84 seconds to generate, and this is true for a large range of input conditions. Due to this, it is relatively trivial to generate detailed parameter sweeps. The results of such a sweep are presented in figures 33 and 34, for a range of conditions comparable with those observed in the semi-analytical model, but maintaining the plasma length at 4 cm.

Unfortunately, the global model has approximately opposite inputs and outputs when compared to the semi-analytical model. This makes it difficult to compare the

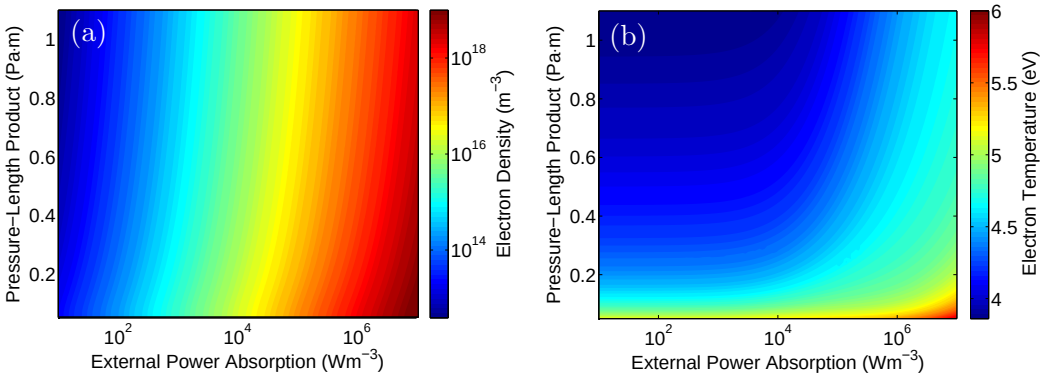

Figure 33: Behaviour of the global model (a) electron density and (b) electron temperature as a function of pressure-length product and absorbed power.

two, particularly as each has three input parameters. Keeping one of the global model inputs constant is not the same as keeping any of the semi-analytical model inputs constant, and so direct numerical comparison of such results is not possible, and contrasting trends requires caution.

Figure 33(a) shows how the absolute electron density varies over the parameter range explored. It is clear that n_e has a much stronger dependence on the absorbed power, which agrees with the previously discussed community expectations. The dependence is almost linear, with $n_e \propto S_{e0}^{0.965}$. The behaviour of the electron temperature, shown in figure 33(b) is less straightforward, and exhibits different trends at low and high powers. This change has a parallel in the semi-analytical model, where at a low relative electron density in figure 30 there is a relationship only between the pressure-length product and electron temperature. In both models, this changes at higher powers, and higher electron densities, where plasma self-interaction starts to affect the behaviours.

Although direct numerical comparisons cannot strictly be made, it is interesting to note that the electron temperature in the low power region does not drop far below 4 eV for the range of pressure-length product shown. In comparison with the semi-analytical model, this is closer numerically to the behaviour of the isothermal version, as would be expected.

The trends that can be found in these two plots are the same as for the semi-analytical model; there is an inverse relationship between T_e and pL at low powers. In the high power regime of the semi-analytical model the pressure-length product increases for increasing density (and power) as the electron temperature is kept constant. If one traces a contour of constant T_e in the right hand section of figure 33(b) then both the electron density and pressure-length product are seen to increase as the power

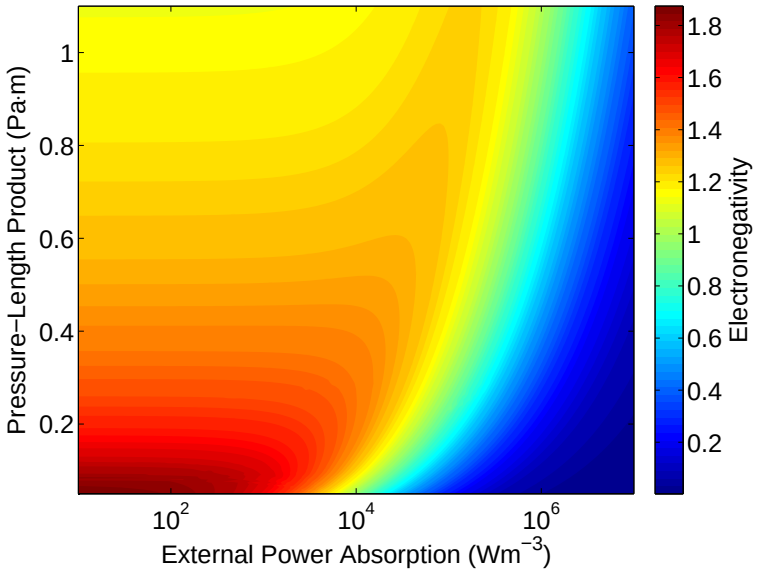

Figure 34: Behaviour of the global model electronegativity as a function of pressure-length product and absorbed power.

rises, which are the same trends as seen in the semi-analytical model.

One property that is an output of both models is the electronegativity. The behaviour of α_0 is shown for the global model in figure 34, over the same range as the previous results. Once again, there is a clear transition between the low and high density modes, however this time the agreement between the two models is more difficult to illustrate. In the low density regime, the relationships are the same, with a dependence almost exclusively on pressure-length product, or electron temperature in figure 29. In the high power region of both models there is a transition of the electronegativity dependence to mostly on the electron density and input power. Figure 29 shows that for the semi-analytical model the dependence of the electron temperature has the same direction in both the low and high density regimes. In the global model the gradient of the electronegativity with respect to pressure-length product, for a constant input power, changes sign across the transition. This appears to be a contradiction between the models, but as mentioned one must take care to ensure that one is comparing the same things, as the inputs and outputs of each model are different. It was shown in figure 33(a) that the absolute electron density remains roughly constant as the pressure-length product changes, which would lead one to expect that the horizontal axes in figures 29 and 34 are approximately equivalent. However, it is the *relative* electron density that is used in the semi-analytical model. While the absolute electron density is shown to have only a slight dependence on the pressure-length product in the global model, this is not the case for the relative electron density, as $N_e \propto n_e/pL$.

Thus the relative electron density has an inverse relationship with the vertical axis in figure 34, which is stronger than the trend of α_0 at a constant input power in the high density regime. This means that, in the global model, for a constant relative electron density, the gradient of the electronegativity with respect to pressure-length product does not change sign across the mode transition, and so agreement is found with the semi-analytical model.

5.3 Conclusions

The contents of this chapter demonstrate that it is comparatively easy to build a simple global model, even for an electronegative plasma. Once it is built, the numerical solution is uncomplicated and requires a relatively small amount of computation time. The global model developed here is reasonably simple, but it is possible to include additional physics or chemistry to create a highly detailed model that describes a very complex plasma [12, 156]. For these, and other, global models, seemingly sensible results can be generated for a wide range of input conditions. The combination of speed, flexibility, and detail, as well as the ease of development and use, means that global models have a large user base in the plasma physics community, and are often a first point of call to understand a new phenomenon.

However, this flexibility is not always a good thing. Global models will often successfully provide results using inputs that are well outside the range in which their assumptions hold. One must be careful not to draw conclusions from data that is not necessarily valid. Although this statement is of course true for any model or even experiment, it is occasionally more difficult to be certain for global models. There is usually no sudden change in results between a valid region and an invalid one, and one must be aware of the assumptions used in the model's development to know which region is being investigated.

With regards to the global model developed here, the results presented are within the valid region of all of the approximations, with perhaps the exception of isothermal electrons. It is not clear where in parameter space, if ever, this assumption is valid, as there will always be spatial gradients in any plasma. Despite this, the trends in the results agree with the semi-analytical model, which does contain spatial information. As is to be expected, the behaviour of the electron temperature, in particular, is closer to the isothermal version of the semi-analytical model, for which doubt has been cast on the results. As discussed, differences in the input and output parameters mean that

a direct numerical comparison or wide ranging data is not possible. Contrasting in this way is only possible for specific cases, and this will be performed in Chapter 7 alongside a full fluid model.

The results and conclusions drawn in this chapter show that global models are a highly valuable tool for the plasma physics community, and they allow the rapid investigation of occasionally complex environments. However, their results must be analysed carefully, as the assumptions used in their development are relatively severe, and the applicability of global models is limited by their lack of spatial self consistency.

Chapter 6

Neutral Dynamics

In the previous chapters, it was shown that the type of semi-analytical model that has been developed is able to provide useful data for a plasma in a pure oxygen background. However, the question has been raised as to the effects of including the neutral background as a self consistent species. This chapter deals with the derivations and implementations necessary to make this happen, and shows what effect it has on results from the model.

6.1 Equation Development

The addition of a self-consistent neutral species, or rather, the removal of the assumption of a constant neutral background, can be easily implemented by including an additional instance of (4.12) for the neutral species. However, the neutrals are also strongly affected by heating; energy from the plasma is transferred to them increasing the neutral temperature. This causes a rarefaction of the gas through the ideal gas law [16], and possibly dissociation of molecular species. Further decreases in the neutral density are proposed to arise from the effect of the pressure balance between the neutrals and the plasma species, particularly the high temperature electrons [17], as well as the 'pumping' of neutrals through a process of ionisation, transport to the wall, and subsequent neutralisation [157].

With this in mind, it is also necessary to include an energy transport equation for the neutral species. This will be the same as (4.8), but the heat flux is determined by the Fourier law (2.43), as the neutrals are assumed to interact mostly with themselves. As the temperature gradient is expected to be comparatively low [158] the terms involving g_α can be removed from both the momentum and energy balance equations.

The only new derivation steps that are required are to find $\boldsymbol{\nabla} \cdot \boldsymbol{q}_g$, the subsequent normalisation, and the resulting final expression for the energy balance that comes from substituting it into (4.8). As part of the derivation, normalised versions of the two constants in the Fourier law of thermal conductivity must be used, which are given below.

$$h_a = \frac{k_B^2}{m_i K_0}\Lambda_a \qquad\qquad h_b = \frac{k_B^2 T_{e0}}{m_i K_0}\Lambda_b$$

From (2.43):

$$\begin{aligned}
\boldsymbol{q}_g &= -\left(h_a T_g + h_b\right)\boldsymbol{\nabla} T_g \\
\boldsymbol{\nabla}\cdot\boldsymbol{q}_g &= -\nabla\left[\left(h_a T_g + h_b\right)\boldsymbol{\nabla} T_g\right] \\
\boldsymbol{\nabla}\cdot\boldsymbol{q}_g &= -h_a(\boldsymbol{\nabla} T_g)^2 - \left(h_a T_g + h_b\right)\nabla^2 T_g \qquad (6.1)
\end{aligned}$$

$$\begin{aligned}
\frac{n_f K_0}{u_B} n_f u_B k_B T_{e0} Q_g' &= -\frac{k_B^2}{m_i K_0}\frac{n_f^2 K_0^2}{u_B^2} T_{e0}^2 \Lambda_a \left(\frac{T_g'}{T_{e0}}\right)^2 \qquad (6.2)\\
&\quad - \frac{k_B^2 T_{e0}}{m_i K_0}\frac{n_f^2 K_0^2}{u_B^2}\left(\Lambda_a \frac{T_g}{T_{e0}} + \Lambda_b\right)\frac{T_g''}{T_{e0}} \\
Q_g' &= -\Lambda_a \left(\frac{T_g'}{T_{e0}}\right)^2 - \left(\Lambda_a \frac{T_g}{T_{e0}} + \Lambda_b\right)\frac{T_g''}{T_{e0}} \\
Q_g' &= -\Lambda_a \frac{\gamma_g'^2}{\gamma_g^4} - \left(\Lambda_a \gamma_g^{-1} + \Lambda_b\right)\left(2\frac{\gamma_g'^2}{\gamma_g^3} - \frac{\gamma_g''}{\gamma_g^2}\right) \\
Q_g' &= -\left(3\Lambda_a + 2\Lambda_b\gamma_g\right)\frac{\gamma_g'^2}{\gamma_g^4} + \left(\Lambda_a\gamma_g^{-1} + \Lambda_b\right)\frac{\gamma_g''}{\gamma_g^2} \qquad (6.3)
\end{aligned}$$

The normalised expression (6.3) can be inserted directly into (4.8) to provide an equation for the neutral energy balance, as shown below.

$$\begin{aligned}
\gamma_g'' = \Bigg(&\left(3\Lambda_a + 2\Lambda_b\gamma_g\right)\frac{\gamma_g'^2}{\gamma_g^2} + \tfrac{3}{2}\Gamma_g\gamma_g' + \gamma_g\Gamma_g\frac{N_g'}{N_g} + \left(\frac{M_g\gamma_g\Gamma_g^2}{2N_g^2} - \frac{5}{2}\right)\gamma_g\Gamma_g' \\
&+ \sum_\beta \Bigg\{ \frac{M_g M_\beta}{\left(M_g + M_\beta\right)^2}\gamma_g\epsilon_{g\beta}\Bigg[M_\beta\gamma_g\frac{\left(N_\beta\Gamma_g - N_g\Gamma_\beta\right)^2}{N_g N_\beta} \qquad (6.4)\\
&\qquad -3N_g N_\beta\left(1 - \frac{\gamma_g}{\gamma_\beta}\right)\Bigg]\Bigg\}\Bigg) \times \left(\Lambda_a\gamma_g^{-1} + \Lambda_b\right)^{-1}
\end{aligned}$$

The expression given in (6.4), while still unwieldy, is not as complex as the equivalent expression for electrons, and whilst two new parameters are introduced, they are constants so do not require more than a single value for any given input conditions. As

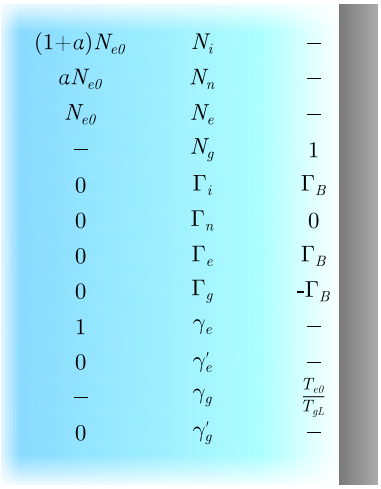

Figure 35: Boundary conditions for the semi-analytical model including non-isothermal neutrals. Central plasma conditions are on the left, edge values are on the right.

before, this equation must be transformed into one that takes the logarithmic densities as arguments, for the numerical benefits that this gives. This is given in (6.5).

$$\begin{aligned}\gamma''_g = \Bigg(& \left(3\Lambda_a + 2\Lambda_b\gamma_g\right)\frac{\gamma'^2_g}{\gamma^2_g} + \tfrac{3}{2}\Gamma_g\gamma'_g + \gamma_g\Gamma_g L'_g \\ & + \left(\tfrac{1}{2}M_g\gamma_g\Gamma^2_g\mathrm{e}^{-2L_g} - \frac{5}{2}\right)\gamma_g\Gamma'_g \\ & + \sum_\beta \Bigg\{ \frac{M_g M_\beta}{\left(M_g + M_\beta\right)^2}\gamma_g\epsilon_{e\beta}\Bigg[M_\beta\gamma_g\frac{\left(\mathrm{e}^{L_\beta}\Gamma_g - \mathrm{e}^{L_g}\Gamma_\beta\right)^2}{\exp\left(L_g + L_\beta\right)} \\ & \qquad - 3\exp\left(L_g + L_\beta\right)\left(1 - \frac{\gamma_g}{\gamma_\beta}\right)\Bigg]\Bigg\}\Bigg) \times \left(\Lambda_a\gamma_g^{-1} + \Lambda_b\right)^{-1}\end{aligned} \tag{6.5}$$

6.2 Model Development and Implementation

With new variables come new boundary conditions. The assumption is made that the neutral species are in contact and thermal equilibrium with a wall held at 300 K, and that the density at the edge also returns to the gas fill density n_f [104]. Although this is not fully consistent with the charged species boundary being the sheath edge, it can be interpreted as assuming that the sheath has negligible impact on the neutral properties, either because it is thin, or because the charged species densities are too low within to have any effect. Unfortunately this means that the boundary conditions for both the neutral density N_g and the neutral temperature coefficient γ_g are specified at the edge of the discharge, and unconstrained at the centre, as shown in figure 35.

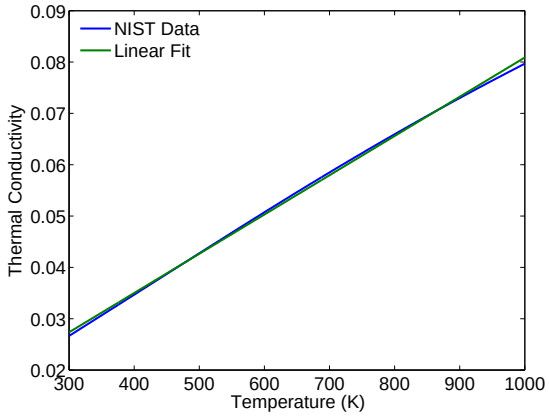

Figure 36: Thermal conductivity of pure oxygen at a constant pressure of 10 Pa. Results for pressures from 0.1 Pa to 1×10^5 Pa are imperceptibly different.

This means that a numerical scheme must be developed to make initial guesses on the central neutral properties, and then adjust them until the edge boundary conditions are met in a minimisation or root finding type problem. This scheme will be detailed later.

As far as additional parameters are concerned, the only additions compared with the non-isothermal model of Chapter 4 are the thermal conductivity constants. The values for these are obtained using data provided by the National Institute of Standards and Technology, accessible in an online database [159]. This data and the linear fit used to obtain the coefficients are both given in figure 36. From the linear fit, the coefficients are $h_a = 7.6478 \times 10^{-5}\,\mathrm{W\,m^{-1}\,K^{-2}}$ and $h_b = 4.4068 \times 10^{-3}\,\mathrm{W\,m^{-1}\,K^{-1}}$. For the other necessary parameters, such as reaction rate coefficients or inelastic energy losses, these are unchanged from those detailed in Chapter 4.

As mentioned above, there is a requirement for a new numerical scheme due to the boundary conditions of the neutral properties. Similarly to the negative ion flux, the neutral density and temperature are specified at the edge of the integration, but unlike Γ_n, they are free parameters at the centre. As $\Gamma_{n,L}$ is largely independent of both $N_{g,0}$ and $T_{g,0}$, with the exception of the weak effect of elastic collisions, the neutral parameters can be found separately to α_0. However as the density and temperature are closely coupled, it is logical to solve for them simultaneously. Unfortunately the shared parameter space of $N_{g,L}$ and $T_{g,L}$ is non-trivial for the inputs $N_{g,0}$ and $T_{g,0}$, and contains discontinuities and inaccessible regions. In order to work around this, iterative values of N_{g0} and T_{g0} are chosen based on the record of past attempts. Starting from an initial point of $N_{g0} = 1$ and $T_{g0} = 300\,\mathrm{K}$, the next two attempts are found through a simple independent linear extrapolation, using $N_{g0}^{n+1} = 1 + N_{g0}^{n} - N_{gL}^{n}$ and

$T_{g0}^{n+1} = 300 + T_{g0}^{n} - T_{gL}^{n}$, where the superscripts are iteration indices.

If this has not found a solution after three attempts, then a 2D co-dependent linear regression is applied. This assumes that the edge values for the neutral density and temperature are linear functions of both central values, as given in (6.6) and (6.7).

$$N_{gL} = a_n N_{g0} + b_n T_{g0} + c_n \tag{6.6}$$

$$T_{gL} = a_t N_{g0} + b_t T_{g0} + c_t \tag{6.7}$$

So that the fit can be easily applied to multiple points, each of these expressions can be given in matrix form as $\boldsymbol{Y}_s = \boldsymbol{X}\boldsymbol{A}_s$, where the subscript can be either n or t, and the matrices are given below for a fit being applied to p trial points.

$$\boldsymbol{Y}_n = \begin{bmatrix} N_{gL,1} \\ N_{gL,2} \\ \vdots \\ N_{gL,p} \end{bmatrix} \quad \boldsymbol{Y}_t = \begin{bmatrix} T_{gL,1} \\ T_{gL,2} \\ \vdots \\ T_{gL,p} \end{bmatrix} \quad \boldsymbol{X} = \begin{bmatrix} N_{g0,1} & T_{g0,1} & 1 \\ N_{g0,2} & T_{g0,2} & 1 \\ \vdots & \vdots & \vdots \\ N_{g0,p} & T_{g0,p} & 1 \end{bmatrix} \quad \boldsymbol{A}_n = \begin{bmatrix} a_n \\ b_n \\ c_n \end{bmatrix} \quad \boldsymbol{A}_t = \begin{bmatrix} a_t \\ b_t \\ c_t \end{bmatrix}$$

The fit can be applied independently to each equation using standard linear regression techniques [160] to give the fit parameters $\boldsymbol{A}_n$ and $\boldsymbol{A}_t$. The regression formula used is $\boldsymbol{A}_s = (\boldsymbol{X}^\intercal \boldsymbol{X})^{-1} \boldsymbol{X}^\intercal \boldsymbol{Y}_s$, where $\boldsymbol{X}^\intercal$ denotes the matrix transpose of $\boldsymbol{X}$. Once these are found, then (6.6) and (6.7) are rearranged to the form in (6.8) and (6.9) to avoid issues with rank deficient matrices in the next fit.

$$N_{gL} - c_n = a_n N_{g0} + b_n T_{g0} \tag{6.8}$$

$$T_{gL} - c_t = a_t N_{g0} + b_t T_{g0} \tag{6.9}$$

To estimate the values of N_{g0} and T_{g0} that give the correct edge boundary conditions, these two equations can now be treated simultaneously. They can be expressed this time as a single matrix equation, $\boldsymbol{C}\boldsymbol{G} = \boldsymbol{E}$, with the matrices again given below.

$$\boldsymbol{C} = \begin{bmatrix} a_n & b_n \\ a_t & b_t \end{bmatrix} \qquad \boldsymbol{G} = \begin{bmatrix} N_{g0} \\ T_{g0} \end{bmatrix} \qquad \boldsymbol{E} = \begin{bmatrix} 1 - c_n \\ 300 - c_t \end{bmatrix}$$

From these, matrix inversion of $\boldsymbol{C}$ is used to find the next estimate of the central neutral properties. As the equations (6.8) and (6.9) are treated simultaneously, the resulting combined estimate for N_{g0} and T_{g0} is that which should give the best values

for both of the respective edge values, given the information and assumptions used in the two stage regression.

This linear regression technique is applied to the previous three iterations until the correct central values are attained, or until four points are found that bound the region in which the correct solution should lie in parameter space. The regression is then applied to the four bounding points that have the minimum total error on the neutral edge properties, defined as $(N_{gL} - 1)^2 + (T_{g0}/300 - 1)^2$.

If no bounding area is found within a number of iterations, then a Monte Carlo technique is used to find more suitable points in the parameter space. This selects a random point that is biased toward points with a small error, but away from large clusters of points, to ensure that a discontinuity is not being focussed on.

These new numerical techniques are implemented in a layer around the previous methods of electronegativity minimisation, including the perturbations, as finding the correct neutral properties requires that the other boundary conditions are also met.

6.3 Results

Investigation of the effects of including self-consistent neutrals begins with a single model run taken at a high electron temperature and density. High values are chosen as it has been shown that, as is to be expected, the impact of the plasma on the neutral species is higher at high plasma densities and temperatures [103].

6.3.1 Example Profiles

Results for a plasma with a central temperature of 4.8 eV and a relative electron density of around 10^{-4} are shown in figure 37.

The profiles of charged species properties are much the same as for the non-isothermal model of Chapter 4. Numerical analysis indicates that it is just within the criteria for a structured plasma, as would be expected for a system with a high electron temperature. The species fluxes do not display any unusual behaviour, and the electron temperature profile is as one would expect from the non-isothermal model. Despite the plasma properties exhibiting roughly the same behaviour as the non-isothermal model, it is clear from figure 37(d) that the neutral species are affected by the presence of the plasma. The density is reduced in the centre by around 10 %, and the temperature has increased by 28 K, also around 10 %.

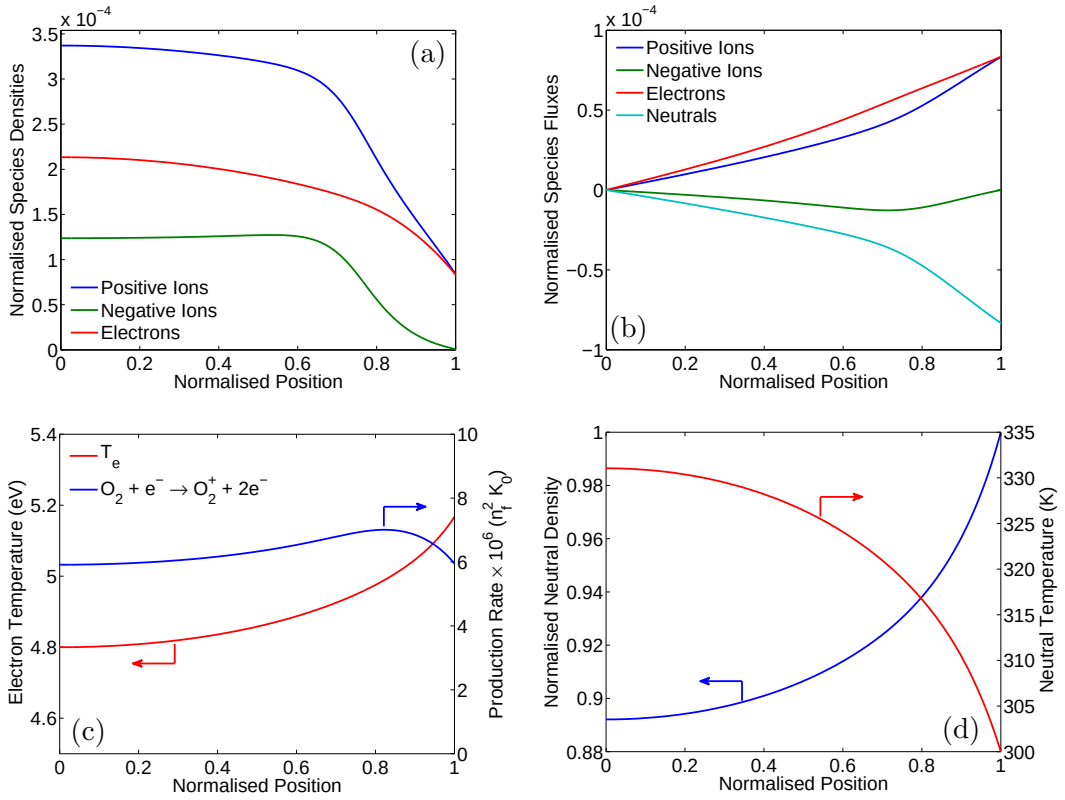

Figure 37: Spatial profiles for the properties of a high density plasma including neutral dynamics, with $T_{e0} = 4.8\,\text{eV}$, $N_{e0} = 2.13 \times 10^{-4}$, and $J_0^2 = J_{base}^2$. Shown are (a) charged species densities, (b) all species fluxes, (c) electron temperature, and (d) neutral properties.

Unlike the charged species, the gradients of the neutral species are generally shallow, and slow to change. Due to the relatively high density of the neutral species, the addition or removal of individual particles through chemical reactions does not have as great an effect as on the charged species. This is the case for both the neutral density (4.7) and temperature (6.4) gradients, both of which contain terms for the change in their respective quantities due to changes in the number of particles through chemical reactions. The coupling between the plasma and the neutrals is therefore mostly through elastic collisions, the effects of which do not change as rapidly in space.

The details of the various effects on the neutral density and temperature were analysed, and it was found that interactions with the fast and heavy positive ions, and the high energy electrons, dominate over the other terms in (4.12) and (6.5). These findings are given in figure 38, which each show only the most dominant terms.

As shown, the density is mostly controlled by the temperature variation, although there is some influence from the positive ions toward the edge of the system, as they gain velocity. Although the streaming velocity of the electrons is comparable to that

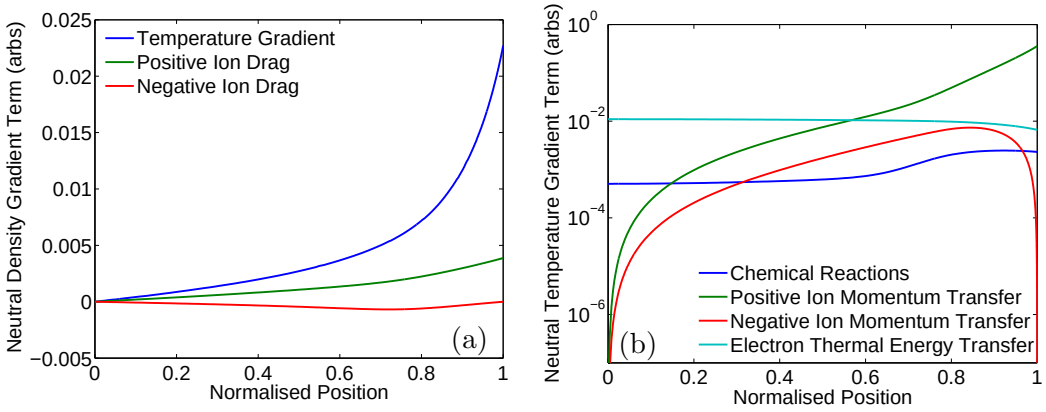

Figure 38: Spatial profiles of the dominant causes of neutral (a) density and (b) temperature changes for the system given in figure 37.

of the positive ions, with a mass five orders of magnitude lower their direct influence on the density through friction is insignificant. For the neutral temperature, it is once again the energetic ions that have the greatest impact at the edge, but in the centre the energetic electrons cause the most heating. Surprisingly, there is a noticeable energy gain from the chemical reactions that take place, though the effect is small compared with the other energy sources. If one calculates what the net effect of the heating is on the neutral density, one finds that it is responsible for about 85 % of the depletion of neutrals in the centre of the discharge. This shows that, for a plasma with these parameters, the heating effect is the most important if one wishes to understand why the neutral density at the centre is reduced.

In order to investigate how the discussed effects change for different input conditions, another run of the model was performed with a low electron temperature and density. The corresponding results for this are given in figures 39 and 40. The behaviours of the charged species are the same as for the non-isothermal model without neutrals, presented in Chapter 4, and shown is an unstructured plasma with the density peaks at the edge of the bulk. The fluxes and electron temperature have changed in the same manner as for the non-isothermal model without neutral dynamics.

However, to the casual observer, figures 37(d) and 39(d) are identical. Only the axes belie the differences that do exist, as both vertical axes have had to be modified to measure the difference from the wall value for their respective variable. This is because the changes in both the neutral temperature and density are on the order of one part in 10^6 across the discharge. In figure 40, the balance between the various terms has shifted slightly, as is to be expected with different charged species profiles, however there are no significant changes in what the dominant effects actually are. This shows

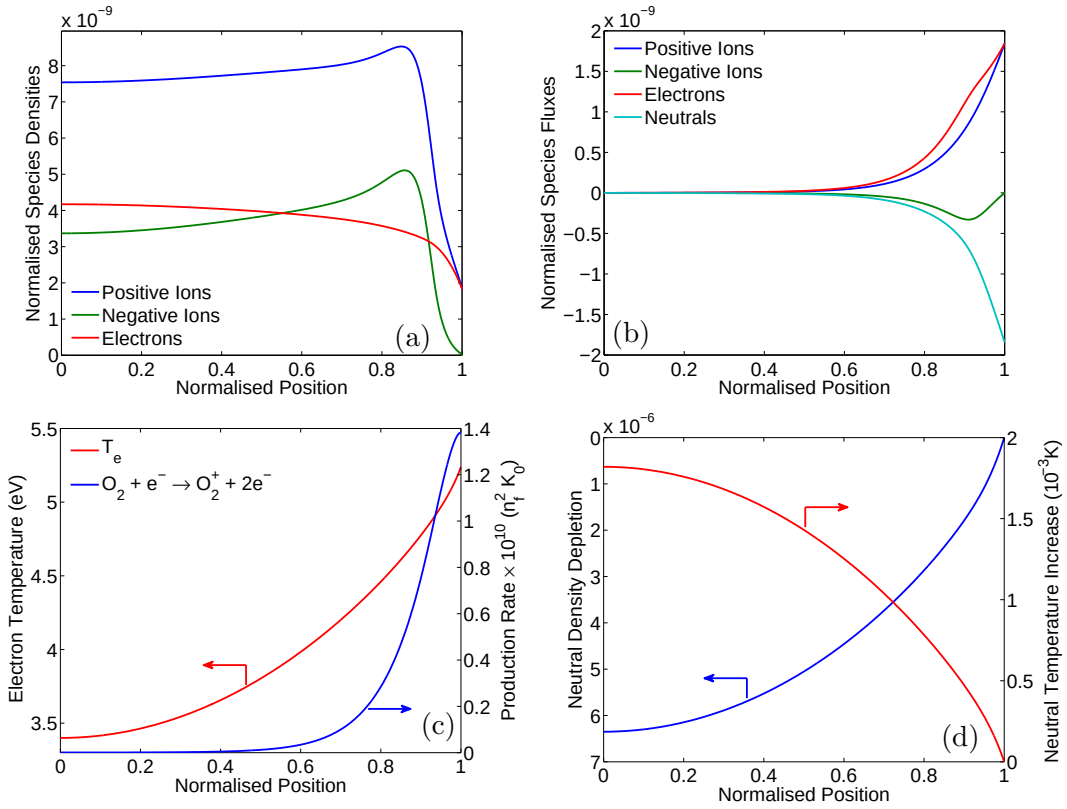

Figure 39: Spatial profiles for the properties of a low density plasma with neutral dynamics, with $T_{e0} = 3.4\,\text{eV}$, $N_{e0} = 4.17\times10^{-9}$, and $J_0^2 = J_{base}^2$. Shown are (a) charged species densities, (b) all species fluxes, (c) electron temperature, and (d) neutral properties.

that the interaction of the charged species with the neutrals is controlled by the same mechanisms regardless of the plasma properties, but that the magnitude of the total effect is changed.

Due to the increased numerical complexity, and particularly the computationally challenge of the neutral boundary condition parameter space, the model now takes significantly longer to run. Systems with a low plasma density, and so a minor impact on the neutral properties, behave much the same as before. However should the model need to implement the more complicated numerical schemes described in the previous section, the computation times increase. The low density example in figures 39 and 40 took just under 40 seconds to complete, but the first example with a significant neutral depletion took roughly 100 seconds to reach a solution. This has implications for the parameter sweeps, as they will now take longer. Fortunately, 100 seconds is still many times shorter than a full fluid model.

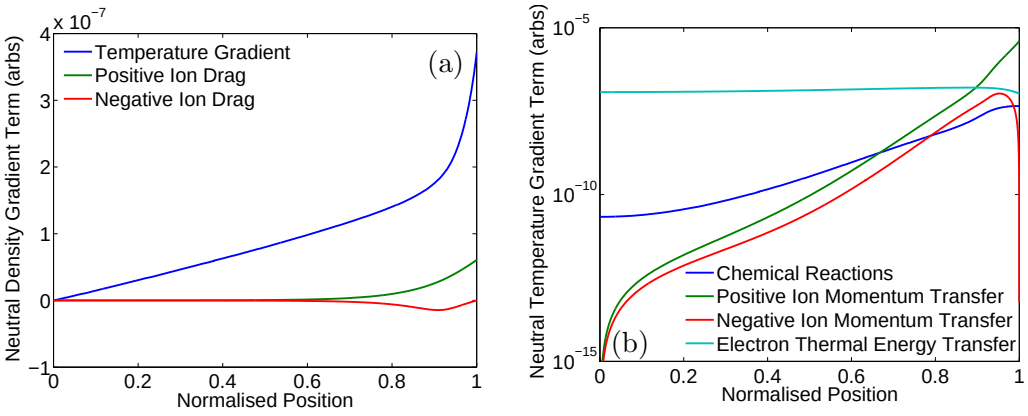

Figure 40: Spatial profiles of the dominant causes of neutral (a) density and (b) temperature changes for the system given in figure 39.

6.3.2 Parameter Sweep

The parameter sweep created using the neutral dynamics model was considerably more computationally expensive than that for the model presented in Chapter 4. Without neutral dynamics, the average execution time for a set of initial conditions that produces a solution was 27.2 seconds. When the neutrals are included, this increases to 40.0 seconds. The majority of the area explored has a similar run time between both models, but as shown in the results, this is because the neutral properties are not heavily affected unless the plasma is hot and with a high charged species density, such as that in figure 37.

In order to visualise the effect that the plasma has on the neutrals, plots have been created from a parameter sweep over the same range as for the previous models, and are given in figure 41.

In figure 41(a), the degree of neutral gas depletion is shown, calculated as the relative difference between the edge and centre values of neutral density $1 - N_{g0}$. Figure 41(b) shows the central neutral temperatures for the same points in parameter space. Both plots appear similar on their relative scales, further evidencing the strong correlation between the two values. Also apparent is the aforementioned requirement for the plasma to be comparatively dense and energetic in order to markedly affect the neutral properties.

Despite the agreement with the prediction that gas depletion is only seen in dense plasmas, in figure 41, both the degree of neutral gas depletion and the neutral temperature are seen to decrease for higher electron temperatures. This can be linked to figure 30, where it is shown that the system pressure-length product strongly decreases with increasing T_{e0}. Therefore, although the causes for depletion are stronger

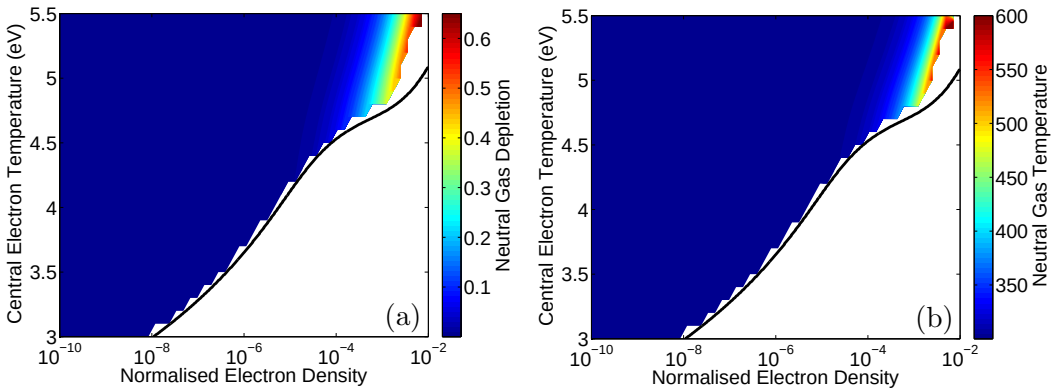

Figure 41: Behaviour of the central neutral (a) density and (b) temperature values as a function of central electron temperature and density for the semi-analytical model with neutral dynamics.

at a higher electron temperature, they are also more limited in space and thus have a smaller net effect on the neutral properties. Also apparent in these results is the difficulty in obtaining solutions when the neutral properties are heavily affected. In contrast to the non-isothermal model without neutral dynamics, at high electron densities and temperatures the model is unable to provide reliable data close to the theoretical validity boundary. Other than this, the results presented in figure 41 are not surprising, and fit in with the previous results and the expectations of the system.

As the interesting data in figure 41 is confined to a small region, a more detailed investigation was performed of the top right section of the parameter space explored. The results of this are given in figure 42, and show two important features. Firstly, there is no deviation from the trends discussed above, nor are there any discernible small scale changes. The second feature is the difficulty evident in obtaining solutions for a high degree of neutral gas depletion. There is no distinct boundary beyond which solutions are impossible. Instead as the degree of depletion increases, there is a gradual breakdown, where holes in the results begin to appear with no obvious pattern. This is further indication that the issue is numerical, rather than analytical, and could potentially be solved through a different numerical scheme.

As the neutral density is reduced for a high plasma density, it is expected that this will have some feedback onto the plasma, due to the important interactions with the neutral species. In order to determine this, the difference was calculated between the resulting plasma parameters for the model with and without the neutral dynamics included, as $\Delta\alpha_0 = \alpha_{0,\text{neuts}} - \alpha_{0,\text{noneuts}}$ and $\Delta pL = (pL)_{\text{neuts}} - (pL)_{\text{noneuts}}$. These measures can be seen plotted in figure 43.

It figure 43(a) it can be seen that, even at low gas depletion levels, there is an impact

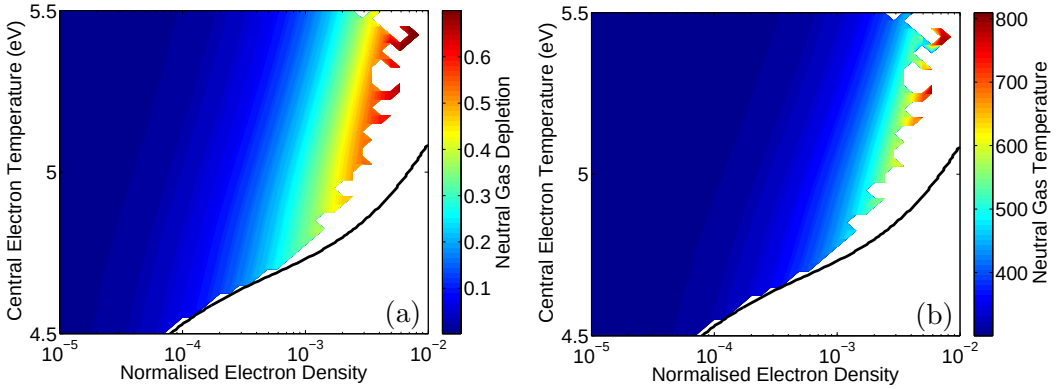

Figure 42: Behaviour of the central neutral (a) density and (b) temperature values over a more detailed region of the parameter space explored in figure 41.

on the plasma. The reduction in neutral density causes a drop in the electronegativity and an increase in the system pressure-length product. Both of these trends can be understood through the alteration of the balance of the reaction set. In the same way that a high electron density alters the system behaviour by causing plasma self interaction processes to increase in importance, a reduction in neutral density will decrease the rates of plasma-neutral interactions. Although the cause is different, the effect of shifting the balance of dominance more toward plasma self interaction is the same. Therefore one would expect that the trends between increasing N_{e0} and decreasing N_{g0} are the same, and indeed this is the case. Looking back at figures 29 and 30 it is shown there that both the electronegativity reduction and pressure-length increase with increasing N_{e0}, and that the effect on α_0 is greatest, with the change in pressure-length product being restricted closer to the limit of validity. With changes of over 60 % in the electronegativity, and up to 80 % in the pressure-length product, the impact of neutral dynamics on the plasma can be very large, when compared to the model excluding neutrals.

6.4 Conclusions

It has been shown that it is possible to include neutral dynamics in a semi-analytical model of an electronegative plasma, but not without adding to the already high degree of complexity. The increase to twelve simultaneous nonlinear differential equations leads to very strong coupling between species, and the requirement for performing root finding in such a system causes computational difficulties, which have not been entirely overcome.

Despite these difficulties, results have been obtained and they show how impor-

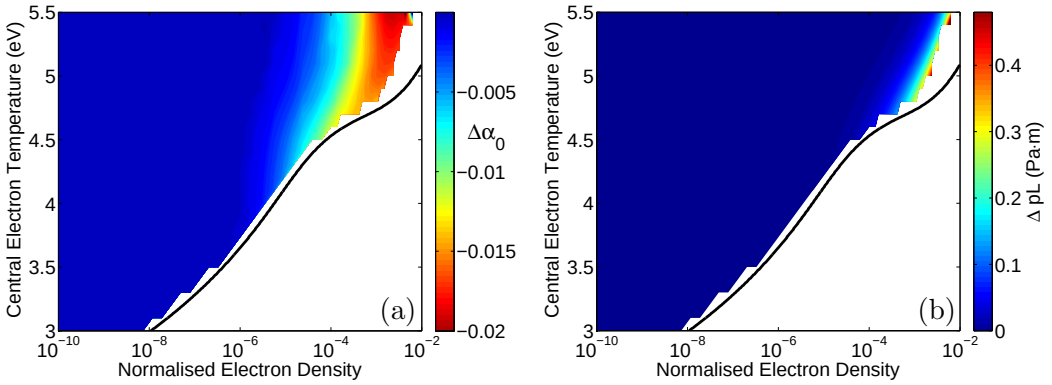

Figure 43: Calculated differences between (a) the electronegativity and (b) the pressure length product between results from the semi-analytical model with and without neutral dynamics.

tant the impact of neutral dynamics are on systems with a relatively high degree of ionisation. Significant impacts on the plasma and neutral species are seen at relative densities of 10^{-4} and above, but minor effects are seen for plasma densities at one part in 10^6. Plasmas with such fractional densities are common [45, 161, 162], particularly in industrial applications where the neutral species can be important for the process, and so a non-uniform density profile would be detrimental. It is therefore important to understand the reasoning behind the neutral gas depletion, and what effects it has on both the neutral and plasma species.

The common reported effects considered important for neutral gas depletion are gas heating [17], ion drag [163], electron pressure effects [14, 164], and ion pumping [157]. In this model it is shown that the gas heating and ion drag effects are certainly important, however the ion pumping is not able to be investigated, due to the lack of a wall and subsequent feedback.

For the electron pressure effect, a simple analytical approach [158] indicates that the total pressure, that is the sum of all species partial pressures, is an invariant. One could expect that this would result in a reduction of neutral pressure, and so a depletion effect, in high density discharges where the electron partial pressure is comparable to the gas fill pressure. If a similar analysis is performed on either (4.3) or (4.7), then it is found that terms remain involving the electric field and the chemical reactions, indicating that although the frictional forces are zero sum, there are other effects that mean that in a more detailed fluid model, a pressure analysis is not as simple as investigating an invariant.

It is also worth considering that the difference between discussing partial pressures and talking about the impact of hot electrons on cold neutrals is also the distinction

between fluid and particle effects. When investigating a fluid model, the separation between the two concepts is blurred due to the very nature of the fluid equations. Any effect attributed to partial pressures, must in reality be caused by elastic collisions between particles. The interaction of electrons with the neutrals through elastic collisions is accounted for in this model, by the transfer of both thermal energy and momentum, and yet there is no explicit 'pressure' interaction. It can be argued that the supposed electron pressure effect is simply a combination of gas heating and friction that arises from the difference between the macro- and microscopic viewpoints. Therefore including electron pressure as a possible cause of neutral gas depletion alongside heating and friction is superfluous.

Chapter 7

Cross-Model Comparison

One of the key motivations for this work is to provide an alternative type of model that can complement both global and full fluid models. It should allow researchers to investigate phenomenon that are not captured by global models, but are impractical to study using full fluid models. It is clear from the work and results detailed in the previous chapters that the new semi-analytical model provides more information than global models, in the form of spatial profiles of particle densities, fluxes, and temperatures. It is also able to spatially resolve reaction rates, and the importance of non-uniform electron temperatures and power deposition has been demonstrated.

However it is not currently clear if the results from the semi-analytical model accurately portray the system being modelled, namely a parallel plate oxygen RF CCP. In order to determine this, one would ideally compare the results with accurate and precise measurements of such a system. Unfortunately there are a relatively large number of parameters required to provide a full comparison with the semi-analytical model, and no published experiment has been found that provides a comprehensive enough suite of measurements of the correct type of discharge.

In order to work around this, comparisons will be made with the full fluid model detailed in Appendix A. This 1D, time resolved model has been compared with experiment and a PIC simulation via real and simulated measurements of phase resolved optical emission spectroscopy (PROES) [13, 35, 165, 166], and makes for a credible source of spatial profiles of an oxygen plasma.

The full fluid model naturally differs from the semi-analytical model in a number of ways. In order to remove a significant difference, comparisons will be drawn with the model of Chapter 4, as the effect of neutral dynamics is not included in the full fluid model. There are also differences in the derivation and implementation of the

underlying equations that could lead to discrepancies.

Although both models are based on the moments of the Boltzmann equation as found in Section 2.4.3, they differ in a number of ways in the subsequent formulation of the transport equations that are actually used. Both the full fluid and semi-analytical models describe heavy particles as fluids, and electrons semi-kinetically through the use of reaction rate coefficients obtained from BOLSIG+, as described in Section 2.3.3, however the two models differ markedly in their description of elastic collisions between species. The full fluid model uses the drift diffusion approximation, described in Section 2.6.2, and so a number of terms are discarded or collected to allow elastic collision effects to be summarised by two parameters. In contrast, the semi-analytical model performs a collection of terms only after all of the effects of elastic collisions have been considered, as detailed in Section 2.4.4. This results in more complex equations, but a more comprehensive description of how elastic collisions affect the system. In particular, the treatment of energy transport using diffusion coefficients causes the neglection of a number of terms that appear in (2.42), such as the consideration of how the creation and destruction of particles affects the kinetic and thermal energy of a species. The drift diffusion treatment also precludes the consideration of how the energy dependence of the elastic collision rate creates effects due to steep temperature gradients, the importance of which is discussed in Section 4.2.

In addition to the treatment of elastic collisions, there are major differences in the treatment of terms related to the inclusion and effects of electric fields. The most severe of these differences is arguably the presence of Poisson's equation in the full fluid model, compared with the assumption of quasineutrality in the semi-analytical model. This difference has implications mainly for the behaviour of each model at the edges of the system. As discussed in Section 4.3.4, differences arise between the two models due to the ability, or not, to resolve the sheath. The removal of the sheath means that the solutions of the semi-analytical model are known to be unphysical at the edge of the system, and attempts to continue the solution into the region where a sheath would exist result in singularities in a number of properties.

As the full fluid model is able to resolve the full electric field in time as well as space, it is able to include an explicit ohmic heating term as the product of the electron flux and the electric field. In contrast, the semi-analytical model must approximate the ohmic heating through the assumption of a sinusoidal current density of a given amplitude, as discussed in Section 4.2.

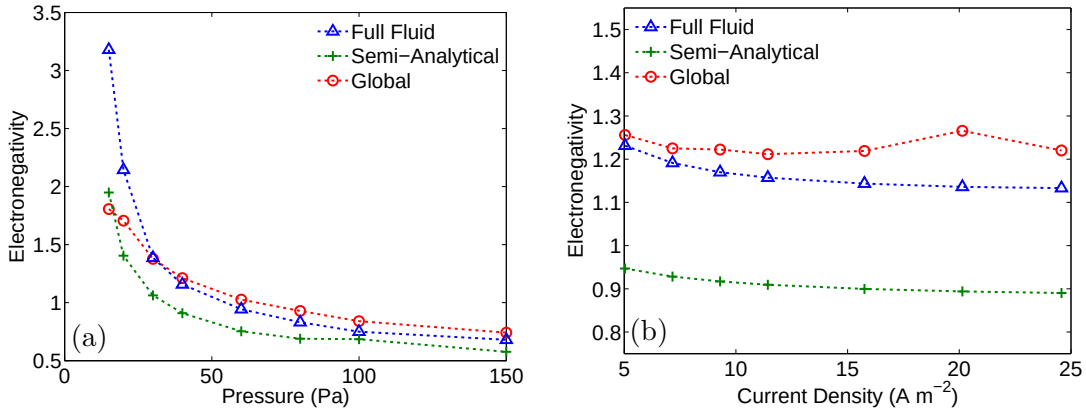

Figure 44: Behaviour of reported electronegativity for the full fluid, semi-analytical, and global models as a function of (a) pressure or (b) current density.

7.1 Comparison of Results

The full fluid model is computationally expensive to run, and so a limited parameter sweep was generated, with a variation in either system pressure or driving voltage for a pure oxygen symmetric RF CCP in a 4 cm gap. For each of these data points, the central electron density and temperature, and the current density, were extracted, and the semi-analytical model from Chapter 4 was run with these inputs. The global model was placed within a minimisation routine to find the background gas density and plasma length that gave the best combination of central electron density and temperature, when compared to the full fluid model. A number of the resulting graphs are plotted over the next few pages, in figures 44 to 46.

The central electronegativity for each model is shown as a function of pressure, at a constant driving voltage of 300 V_{pp}, in figure 44(a) and a function of current density, at a constant pressure of 40 Pa, in figure 44(b). Looking first at the pressure response, it is clear that all three models follow the same trend of electronegativity being approximately inversely proportional to the pressure. There are differences however between them, notably that the semi-analytical model consistently underestimates the electronegativity. Conversely, the global model results are mostly higher than that of the full fluid model, but there is a deviation from this at lower pressures.

In figure 44(b) all three models report a roughly constant value for α_0, as is to be expected as this system is in the low density regime. The semi-analytical model has a nearly identical trend to the full fluid model, but the absolute number is around 25% lower, as expected from the 40 Pa result in figure 44(a). For the global model, again the absolute number for the electronegativity is closer to that of the full fluid model, but

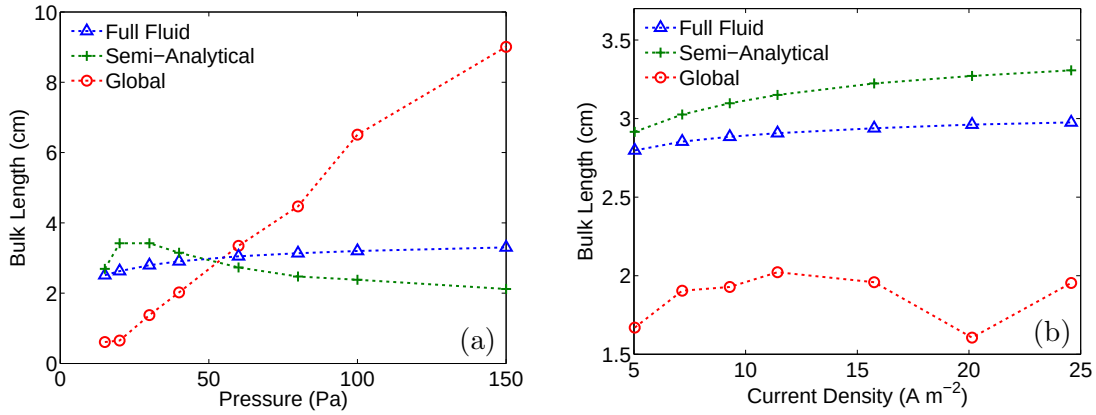

Figure 45: Behaviour of the reported plasma bulk length for the full fluid, semi-analytical, and global models as a function of (a) pressure or (b) current density.

the trend is not. At the higher current densities the result becomes less predictable, and the trend changes from point to point.

Looking at both parts of figure 44 together, there is an overall message that the global model is potentially more accurate in the value of the electronegativity in this parameter range, but that the semi-analytical model is more consistent. In particular at lower pressures or at higher current densities the global model deviates from the expected trends. The issues at low pressure are a known issue for fluid models, due to the breakdown of collisionality assumptions, and it may be that the global model fails at a higher pressure than the other two, due to the lack of self consistency in the spatial variation.

As all three models share the same reaction set, it is expected that they should all have similar values for the electronegativity. However figure 44 demonstrates that this is not the case. The lack of sheath physics, and potentially also the lack of self consistent $O_2\left(^1\Delta_g\right)$, has an effect on both the semi-analytical and global models. As for the higher accuracy of the global model, it is possible that the empirical relations used, particularly that for the edge to centre density ratio, h_l, are able to compensate for this lack of spatial information, with regards to the reaction balance of species. However this is not the case for all of the plasma properties.

Figure 45 shows how the size of the plasma bulk changes for each model at a specific set of conditions, found from the full fluid model as before. The sheath width in the full fluid model was calculated by finding the point s where a spatial integration of the electron density from the edge to s equated a spatial integration of the net charge density from s to the centre of the discharge [141]. The bulk width can then be

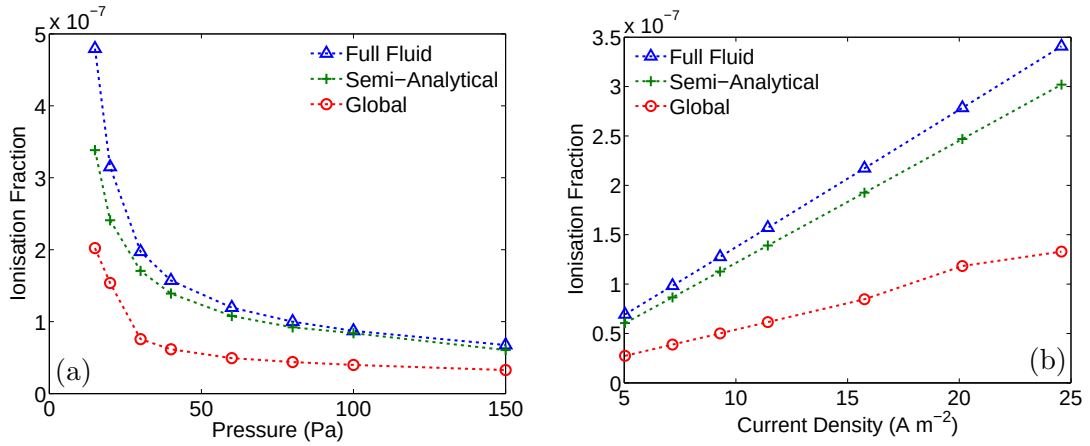

Figure 46: Behaviour of the reported ionisation fraction for the full fluid, semi-analytical, and global models as a function of (a) pressure or (b) current density.

calculated trivially from this. For the global and semi-analytical models, the bulk width is simply the reported pressure-length product divided by the prescribed pressure, as neither model resolves the sheath. As previously, results for this are plotted as a function of either pressure or current density.

In figure 45(a) the behaviour is seen to be different for each model. The full fluid model has a small but steady increase in bulk width as the pressure increases. For the semi-analytical model, the quantitative agreement with the full fluid model is good, but with the exception of data at 15 Pa, the value decreases slightly with pressure. This is not the case for the global model, which has a distinct inability to accurately specify the pressure-length product when programmed to provide a specific absolute electron density and temperature.

These last findings are repeated when the current density is varied, as shown in figure 45(b). Although the trends of each model are now similar, the accuracy and precision of the global model are mediocre. Conversely, the semi-analytical model is able to give good results for this measure. The small discrepancy with pressure variation is likely due to the inverse relationship between pressure and electron temperature. At higher pressures, the low value of T_e across the bulk means that the high energy sheaths may play a more significant role in controlling the plasma behaviour, despite their diminished size.

The final measure to be compared is the ionisation fraction resulting from each model, which is given in figure 46. In the pressure variation, figure 46(a), the trend is the same for all three models. While the semi-analytical and full fluid models agree both qualitatively and quantitatively, the global model consistently reports lower values.

This is repeated in the variation with current density in figure 46(b). The difference between the semi-analytical and full fluid models is around 15%, but the global model reports an ionisation fraction roughly half of the other two. This shows how, without spatially resolved reaction rates, the global model struggles to account for the correct amounts of species creation and destruction, resulting in an underestimation of the ionisation fraction.

7.2 Conclusions

The results presented in this chapter are all within the low density and 'unstructured' regimes. This means that the majority of plasma properties are dependent more on the electron temperature than on the plasma density. Therefore in figures 44 to 46 the plots with pressure on the abscissa can be broadly said to describe the trends and accuracy of each model, while the plots with a variation in current density provide more information about the precision and reproducibility of behaviours.

The same underlying reaction set, and the shared basis on fluid equations, mean that results from each model are expected to be similar, which is broadly true. However the differences in approaches and methodology mean that there will be discrepancies. The assumption, or not, of quasineutrality, and the lack of self consistent excited states in the semi-analytical and global models have caused a loss of information, and create inaccuracies. Even with the spatial resolution of the semi-analytical model, there are spatial effects, such as double layers, that are not captured. Despite these issues, the assumption of quasineutrality, and thus the removal of Poisson's equation from the system, prevents the creation of a stiff set of differential equations, and thus improves both the model simplicity and computation time dramatically.

Discrepancies between the models are also thought to arise due to the very sensitive nature of certain reaction rate coefficients, in particular those for ion creation, as shown in figure 22(a). While the full fluid model uses a lookup table and linear interpolation to find reaction rate coefficients as a function of electron temperature, the semi-analytical and global models use fitted functions to improve computational efficiency. Even though these functions are accurate to within 1%, this may be enough to create sufficient differences that compound over the course of the numerical integration.

This may partially explain another disparity between the models, which is the apparent differences in the relationships between pressure-length product and electron temperature. For the global model, this difference can be explained away by the in-

flation of the necessary temperature caused by the isothermal assumption, but the semi-analytical model also requires a slightly higher electron temperature to match the full fluid model. A modest increase of 2 % to 3 % on the central electron temperature can cause the electronegativity reported by the semi-analytical to match that from the full fluid model almost perfectly. This inconsistency may be in part due to the difference in approaches for obtaining reaction rate coefficients, but is also likely to be affected by the removal of the sheath. It is also likely that the lack of time dependencies has an impact on this. As the reaction rate coefficients are non-linearly dependent on electron energy, even a sinusoidal modulation of T_e over time will change the net rate coefficient for some reactions. Given the over linear relationship of the ionization rate coefficients, many of the mean values would be expected to rise when the temperature oscillates in the region 3 eV to 5 eV.

It is not just the semi-analytical and global models that must be questioned. The full fluid model is still a fluid model, and as such has limitations and inaccuracies. In particular, it uses the drift diffusion approximation, which assumes that fluid transport can be described by thermal diffusion and electric field mobility coefficients. Like the detailed fluid equations used in the semi-analytical model, these assumptions break down at low pressure, when collisionality can no longer be assumed. However, as terms are discarded to form the drift diffusion equations, they may break down at a higher pressure than those used in the semi-analytical model. Thus discrepancies between the two at the lower pressures could arise from either model, or both, as the dropping collisionality affects them in different ways.

Also at the lower pressure scales, the global model is seen to deviate, particularly in the accuracy of the electronegativity. This is thought to be due to the encroachment of the sheath onto the bulk at low pressures, which will reduce the effectiveness of the empirical relations used, such as the derivation of the energy loss due to the sheath, given as ε_s in (5.7). Although the sheath encroachment is also expected to affect the semi-analytical model, this effect does not appear to be as severe.

In the global model, the density of charged species is seen to be an issue, manifesting as discrepancies in the ionisation fraction, and as a need to extend the plasma to obtain the correct electron density. The densities are mostly controlled by the power balance, which is heavily reliant on empirical relations such as the sheath energy losses and the edge to centre density ratio. This shows that the lack of spatial information in the global model causes large errors in the pressure-length product and the ionisation

fraction.

Conversely, the discrepancies between the semi-analytical and full fluid models are within what would be expected due to the lack of consideration of time dependencies and sheaths, and are generally smaller than those between the global and full fluid models. The inclusion of spatial resolution of ionisation profiles in the semi-analytical model allows for much better estimation of plasma densities than the approximations of a zero dimensional model. The limitations of the global model are clear, and can be largely attributed to the empirical relations required for the centre to edge density ratio, which are approximate at best within their limited parameter range, and of unknown behaviour outside it.

Chapter 8

Conclusions and Outlook

The work in this document describes the creation and testing of a novel semi-analytical model for the investigation of electronegative plasmas with neutral dynamics. It was shown that it is possible to develop a model based on the fluid moments of the Boltzmann equations that is able to describe a four component plasma including negative ions and neutral dynamics. It is also possible to solve this as an initial value type problem. This treatment enables the model to provide solutions on a time scale of seconds to handfuls of minutes on a standard 2.5 GHz x86_64 processor, compared with a full fluid model taking around ten hours on a dedicated compute server.

Casting the equations as an initial value problem does not come without difficulty, and the complicated equation set calls for non-standard numerical algorithms. The high degree of non-linearity between the expressions means that links between inputs to and outputs from the numerical integration are not always trivial, and may not even be continuous or differentiable. For systems such as these, MATLAB was found to be a suitable development environment, even though other languages may be faster computationally. The transformation of differential equations into spatial profiles was made much simpler by the suite of included solvers and algorithms, and the live development environment facilitated fast troubleshooting.

Once the algorithms were implemented successfully, the generation and analysis of data followed quickly. A theoretical limit for the parameter range over which the model can provide solutions was described, and verified using a parameter sweep. Despite closely meeting this criterion, the model failed to provide data that compared well to other sources. It was found that using an isothermal approximation for the electrons was inappropriate for this model. The occasionally large spatial variation of the reaction rate coefficients, in particular that of ionisation processes, is important to

resolve in order to accurately describe the plasma behaviour. In order to do so, one requires the spatial profile of the electron temperature.

To include electron temperature variations, an expression for the deposited ohmic power was derived based on the RF current density and the plasma conductivity. This allowed the model to self consistently solve for the gradient of the electron temperature over the integration space. Inclusion of the electron energy transport equation allowed the model to recreate the results of a time resolved, non-quasineutral model with reasonable accuracy, with the obvious exception of the sheath. This improvement also reduced the numerical difficulties faced by the model, and results were obtained to show that the theoretical validity limit provides exactly the boundary of possible solutions.

From the results of the developed model, a number of conclusions can be drawn. The various parameter sweeps show that in this normalised system there are two distinct regions of operation. At a low plasma density, the system behaviour is independent of the plasma density, provided that the central electron temperature and the ohmic power deposited *per electron* remains constant. Above a relative plasma density of roughly 10^{-6}, interactions between charged species start to become important, and a mode transition is seen into one dominated by plasma self-interaction. This includes changes to the behaviours of electronegativity and the relationship between electron temperature and system pressure-length product.

It has been discussed that there are three main potential sources of error, when this model is compared to the full fluid model. The enforcement of quasineutrality means that no charge separation can occur, nor is it possible to have non-monotonic electric potentials. The semi-analytical formulation and casting as an initial value problem means that this model is unable to capture time dependent effects, or phenomena that arise from the interaction of the plasma with the chamber walls. This lack of wall interaction means that the model is unable to self consistently include an important metastable excited state of oxygen, $O_2\left(^1\Delta_g\right)$. This excited state is destroyed primarily through wall interactions, and diffuses freely through the discharge. Another important effect that is not captured due to the lack of wall is the presence of secondary electrons. This precludes the model from being able to capture the 'gamma mode' that is exhibited at elevated powers in real systems.

The restriction of quasineutrality means that instabilities in space, such as double layers, are not present, and the time averaging of equations removes temporal instabilities too, both of which are effects known to be important in electronegative plasmas.

Although the conditions under which instabilities occur depend on the precise system properties, they have been shown to broadly occur at higher pressures and higher powers [132]. These findings correlate with the hypothesis that the limitations prescribed by the central density gradients, which lead to the theoretical validity limit, can be circumvented by irregularities in either time or space. The boundary defined by the derivation of the theoretical limit prevents the model from accessing regions of high electron density with low electron temperature, which would be observed at high pressures and powers in a physical system.

Despite these potential issues, the comparison with a model that is able to capture time dependencies, wall interactions, and space charges, shows that there is still agreement with the results for density profiles in the bulk. The semi-analytical model is able to provide a good estimate of the electronegativity, and other plasma properties, despite the lack of sheath.

So that the usefulness of the semi-analytical model could be gauged against a global model, one of these widely used models was developed. It was shown that while some of their outcomes are useful, they can be unreliable in their results for particular measures. Although they are a quick way to gain insights into certain phenomena, one must take care to understand their limitations and the applicability of the assumptions made in their development. The global model was found to be restricted in accuracy by the lack of spatial information, and the empirical relations used to try and overcome this. In this respect it was concluded that although global models have their use for quick investigations and modelling of chemically complex discharges, the semi-analytical model was a more robust model for the parameter range investigated.

The semi-analytical model was extended to include neutral dynamics, and account for the transport of energy to, from, and within the neutral fluid. It was determined that the additional physics provided by neutral dynamics should be considered if the system is in the region of parameter space where plasma self-interaction becomes important. For a plasma density greater than roughly 1 part per million the neutral density at the centre of the discharge is reduced, through a process known as neutral gas depletion. This effect has been seen and investigated previously, with the possible causes being identified by the community as gas heating, electron pressure effects, frictional forces, and ‘ion pumping’.

In the discussion of neutral dynamics in Chapter 6, it was concluded that gas heating and frictional forces play the dominant and next most important roles, respectively. It

was discussed that electron pressure effects, although intuitively correct, are not well defined in the theoretical framework. The only interactions between the electron and neutral fluids are through elastic and inelastic collisions between particles, of which the elastic collisions are considerably more frequent (see figure 22(a)). Through the separation of motion into random and directed velocities the effect of these collisions can be split into a transfer of either randomly distributed or direct kinetic energies, which correspond to either heating or friction respectively. Thus the concept of pressure plays no part when interactions are considered at a particle level.

The results of this work show that the applicability of the semi-analytical model is similar to that of a full fluid model, and the results for the plasma bulk are quantitatively comparable, but the time cost to the user is hundreds of times smaller. The normalisations applied allow the model to describe a wide variety of systems with a single result, and outcomes are relevant for any discharge that can be approximated as symmetric and infinitely planar. These same normalisations, and the resulting collection of inputs and outputs, define a model that is more suited to the investigation of general properties of planar discharges, or perhaps device design, than the modelling of a specific device. Such an investigation is still possible, however, as the short computation time allows one to perform detailed investigations of large regions of parameter space. This model would be particularly useful in the fast characterisation of systems with a high degree of non-uniformity.

The uncertainties introduced by the removal of time dependencies, space charges, and wall interactions, were shown to be restricted mainly to the sheath region. It is likely that the error introduced by these effects is smaller than the effect of uncertainty in the reaction rate coefficients used. As has been discussed, cross sections and reaction rate coefficients that are found in the literature are often difficult to trace to an original source. Their associated uncertainty can also be problematic to pin down. Despite work to alleviate this [43], it is still an ongoing issue in the plasma physics community, that can create a lack of confidence in the results of modelling.

A number of possibilities exist for the extension and improvement of the work described in this document. It would be highly beneficial to improve the numerical robustness of the algorithms used to determine the correct central neutral properties. It is possible to obtain results through manual control and monitoring, however this is a particularly time consuming process, and an automated solution would be very much preferred.

It would be desirable to extend the system to the modelling of arbitrary gases, with the potential for more than four species. In theory the equations developed are applicable to any number of species and reactions, however the practicalities of the involved numerics would make this a difficult and extensive task. Modelling of a different electronegative gas with a similar reaction set and dominant species, such as chlorine [161], would be an appropriate first step toward this goal.

Finally, it would also be advantageous to investigate a method by which the lack of wall interactions could be circumvented, so that species dominated by surface effects could be modelled self consistently. Unfortunately at this stage an empirical inclusion is the only known solution.

Appendix A

Time Resolved 1D Fluid Model

In Chapters 3, 4, 7 and 8, a detailed fluid model is used as a point of comparison. This model, developed by A. Greb [13, 116, 140, 167] and used with kind permission, is a self-consistent fluid model able to provide one dimensional, time resolved descriptions of symmetric or asymmetric capacitively coupled plasmas.

A.1 Model Description

The model is based on a basic set of equations derived from the first three moments of the Boltzmann equation, (2.26), (2.32) and (2.36), combined with Poisson's equation for the electric potential and field. With the application of the drift diffusion approximation, and the retention of time derivatives, the resulting equations are somewhat different to those used in the semi-analytical model. Given below are the equations used in the full fluid model for mass, flux, and electron energy conservation in (A.1) to (A.3) respectively. These are combined with Poisson's equation for the electric potential (A.4), which is used to find the electric field. In these expressions, symbols are as in the main body of this work, with the addition of the mean electron energy in joules (ε), the electric potential (ϕ), and the electron energy flux ($\boldsymbol{F}_\varepsilon = \frac{5}{3} n_e \boldsymbol{u}_e \varepsilon - \frac{5}{3} n_e D_e \boldsymbol{\nabla} \varepsilon$).

$$\frac{\partial n_\alpha}{\partial t} + \boldsymbol{\nabla} \left(n_\alpha \boldsymbol{u}_\alpha \right) = \sum_{R_\alpha} G_{R_\alpha} n_{R_1} n_{R_2} K_R \tag{A.1}$$

$$\left(n_\alpha \boldsymbol{u}_\alpha \right) = Z_\alpha n_\alpha \mu_\alpha \boldsymbol{E} - D_\alpha \boldsymbol{\nabla} n_\alpha \tag{A.2}$$

$$\begin{aligned} \frac{\partial \left(n_e \varepsilon \right)}{\partial t} + \boldsymbol{\nabla} \boldsymbol{F}_\varepsilon = & - e n_e \boldsymbol{u}_e \boldsymbol{E} \\ & - \sum_{R_e} G_{R_e} n_{R_1} n_e K_R - \sum_\beta 3 \frac{m_e}{m_\beta} \nu_{e\beta} n_e \left(T_e - T_\beta \right) \end{aligned} \tag{A.3}$$

$$\nabla^2\phi = -\frac{e}{\varepsilon_0}\sum_\alpha Z_\alpha n_\alpha \tag{A.4}$$

For closure of Poisson's equation, the electric potential is specified to be zero at the grounded electrode, and the amplitude of a sinusoidally oscillating driving voltage is specified at the driven electrode. For asymmetric systems, this driving voltage can include a non-zero offset, calculated self-consistently from the flux balance.

The boundary conditions for the included species are determined through expressions of the expected flux of particles incident at the chamber walls. For the heavy species, this is a combination of the mean thermal flux, derived from diffusion theory [168], and any direct motion due to an electric field. These are given in the first and second terms respectively of the right hand side of (A.5). In this expression, v_{th} is the mean thermal velocity, given in (A.6), $\hat{\boldsymbol{x}}$ is the unit vector normal to each electrode, and $a = 1$ if $Z_\alpha \boldsymbol{E}\cdot\hat{\boldsymbol{x}} > 0$, or zero otherwise.

$$(n_\alpha \boldsymbol{u}_\alpha)\cdot\hat{\boldsymbol{x}} = \tfrac{1}{4}v_{th,\alpha}n_\alpha + aZ_\alpha n_\alpha \mu_\alpha \boldsymbol{E}\cdot\hat{\boldsymbol{x}} \tag{A.5}$$

$$v_{th,\alpha} = \sqrt{\frac{8k_B T_\alpha}{\pi m_\alpha}} \tag{A.6}$$

For the electrons, secondary electron emission is considered, as discussed below. Thus the boundary conditions for electron flux and energy must take this into account, and do so in (A.7) and (A.8) respectively. In these generalised expressions, η_β is the secondary electron emission coefficient for species β, and ε_η is the initial energy of electrons created through secondary emission, to be defined below.

$$(n_e \boldsymbol{u}_e)\cdot\hat{\boldsymbol{x}} = \tfrac{1}{4}v_{th,e}n_e - \sum_\beta \eta_\beta (n_\beta \boldsymbol{u}_\beta)\cdot\hat{\boldsymbol{x}} \tag{A.7}$$

$$\boldsymbol{F}_\varepsilon\cdot\hat{\boldsymbol{x}} = \frac{5}{3}\left(\tfrac{1}{4}v_{th,e}n_e\varepsilon - \varepsilon_\eta\sum_\beta \eta_\beta (n_\beta \boldsymbol{u}_\beta)\cdot\hat{\boldsymbol{x}}\right) \tag{A.8}$$

For the model as it is applied to a pure oxygen discharge, the full reaction set is reduced based on experimental data [79, 86, 128]. Similar to the work on the semi-analytical model described in this work, the main positive ion is taken to be O_2^+, and the dominant negative ion is O^-. Both of these are shown to account for at least 90% of ions of their respective charge within the parameter regime covered by the full fluid model. Unlike the semi-analytical model, the full treatment allows $O_2\left(^1\Delta_g\right)$ to be included as a separate species. The density of $O_2\left(^1\Delta_g\right)$ is controlled by a similar boundary condition

to the other species, and given in (A.9), where the subscript s denotes quantities relating to $O_2\left(^1\Delta_g\right)$, and s_s is the surface loss probability for $O_2\left(^1\Delta_g\right)$.

$$O_2\left(^1\Delta_g\right) \text{ Wall Flux} = \tfrac{1}{4} s_s n_s v_{th,s} \tag{A.9}$$

The value for the surface loss probability, s_s, is not simple to obtain. It depends not only on the material composition of the chamber walls, which can vary in time, but also on physical properties such as surface roughness and temperature. Literature values for the surface loss probability of $O_2\left(^1\Delta_g\right)$ vary from 1×10^{-5} [118] to 7×10^{-3} [169]. Comparisons with experiments for this model suggest that a value of 1×10^{-5} is appropriate for stainless steel electrodes [116], and so this is the value used in data generated for the comparisons in this work.

The species interactions considered in this model are the same as for the semi-analytical model, given in table 5. There is a slight difference in that the elastic collision rate coefficients are wrapped within the diffusion and mobility coefficients for the relevant species, and the effect on the neutral background gas is not considered. In addition, the effects of strong electric fields on the ion mobilities are considered. The ion temperature is also carefully considered, and while left at 300 K in the bulk, the effect of high electric fields in the sheath is accounted for through an empirical relation inversely proportional to the square root of the electric field strength.

In the same way as for the semi-analytical model, reaction rate coefficients for interactions involving electrons are calculated using the tool BOLSIG+. As discussed in Chapter 7, they are included in the model not as functions, but as look-up tables against electron temperature. This is potentially more accurate than using fitted functions, and other computational overheads in the boundary value solution method employed by the full fluid model are potentially larger than the time required to compute values from the look-up tables.

The reactions are also accounted for as energy loss mechanisms, through inelastic collisions. Ohmic power deposition is included self consistently, as the electric field and electron fluxes are both time and space resolved.

As the whole plasma is resolved, including contact with the wall, it is possible to allow for the emission of secondary electrons (see Section 2.1). For impacting O_2^+ ions, the probabiliy of secondary electron emission was found empirically to be 0.05 for a stainless steel electrode surface. However, this is only an estimate, as like other surface interaction coefficient, the precise values depends on a myriad of surface properties.

The initial energy of emitted electrons was taken to be 0.5 eV [170].

The set of partial differential equations is solved using a finite element method, implemented in COMSOL Multiphysics. The differential equations are applied to a two dimensional mesh in space and time, the spatial extend being the inter-electrode distance, and the time period being a single RF cycle. In this case these are 4 cm and $1/13.56\,\text{MHz} \approx 73.75\,\text{ns}$ respectively. The mesh is linearly distributed in time, with 74 discrete points in time (for roughly 1 ns per point), but the 200 points in the spatial direction are focussed toward the edges. This is because the gradients are steeper in nearly every quantity within the sheath region, and so to improve accuracy without a dramatic increase in computation time, the mesh is concentrated there.

As with all boundary value solvers, the model requires an initial estimate of the system before solution can begin. It was found [167] that uniform profiles of species densities and electron temperature do not cause numerical instabilities. These uniform profiles are used unless there are results available from a solution with similar parameters, in which case these results are taken as initial conditions to reduce the time necessary to reach convergence.

Another consideration required to increase the computational efficiency is that the heavy species operate at a much slower time scale than the electrons. This means that the electrons reach their state of convergence many times faster than the ionic species and neutrals. As the time step within the mesh is required to be short to capture electron behaviour, the means that the simulation is left with 'converged' electrons, but many iterations remaining before the heavy species are solved for. To combat this, a system is implemented whereby effective time averaged reaction rate coefficients are calculated from the converged electron state. These are then used to perform a separate convergence to generate an estimate of the equilibrium state. As the heavy particles fluctuate much less than electrons during a single RF cycle, this equilibrium state is a reasonable approximation for the heavy particle behaviour. The full simulation is then continued from this state. This has been estimated to decrease the computation time required by over an order of magnitude.

A.2 Example Results

The data generated by the full fluid model is resolved in both space and time. Although time averaged values are used to compare against the semi-analytical model, it is still worth looking at the time resolved output to gain insight and understanding as to what

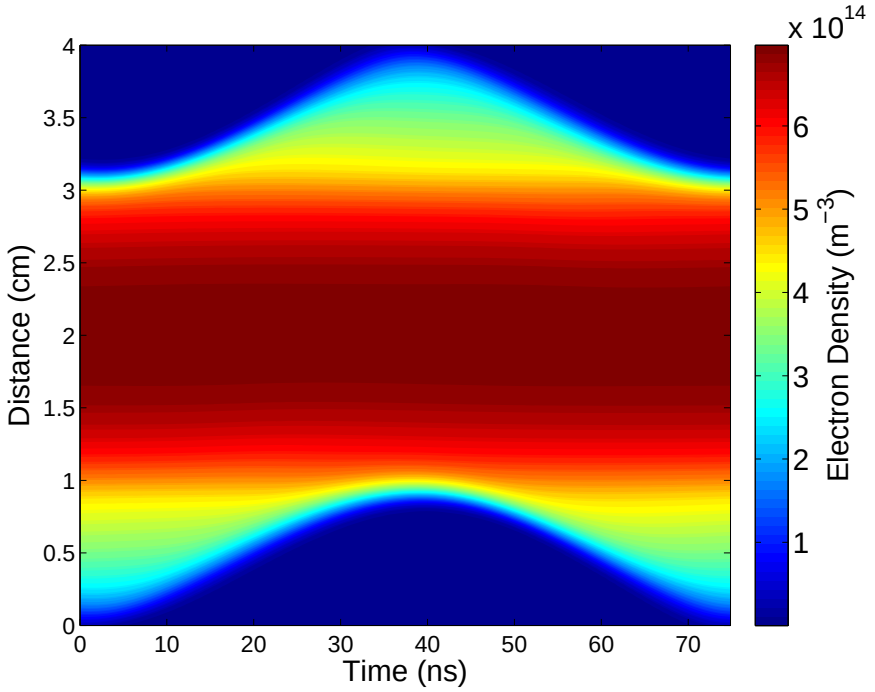

Figure 47: Time and space dependence of the electron density as reported by the full fluid model.

may be missing. To this end, a number of results are presented here for a run used in the comparisons, which has been generated for a symmetric oxygen plasma operated at 40 Pa driven by 300 V_{pp} across two parallel electrodes 4 cm apart.

As an example of the non-trivial behaviour of species, figure 47 shows how the electron density varies as a function of space and time. It shows that, as well as the expected central peak and lowering density toward the edges, the density in the plasma bulk is roughly constant in time, whereas the sheaths are clearly visible and heavily modulated. This is even clearer to see in figure 48, which shows the spatial profiles of the charged species densities at four equally spaced points in the RF cycle.

In figures 48(a) and (c) the electron density can be seen to be highly asymmetric, due to the sheaths being at their maximum and minimum extents at those points. When the two sheaths are roughly equal in size, then the electron density profile is closer to symmetry. This is in contrast to both of the ion densities, which remain symmetric and practically unchanged through the RF cycle.

As discussed in Section 4.2, the ohmic power deposition is intrinsically a time dependent phenomenon, as well as being known to vary in space. In order to qualify this, figure 49 was generated, which shows the volumetric ohmic power deposition across the whole model mesh.

As shown, the power deposition is quite isolated in both space and time. Although

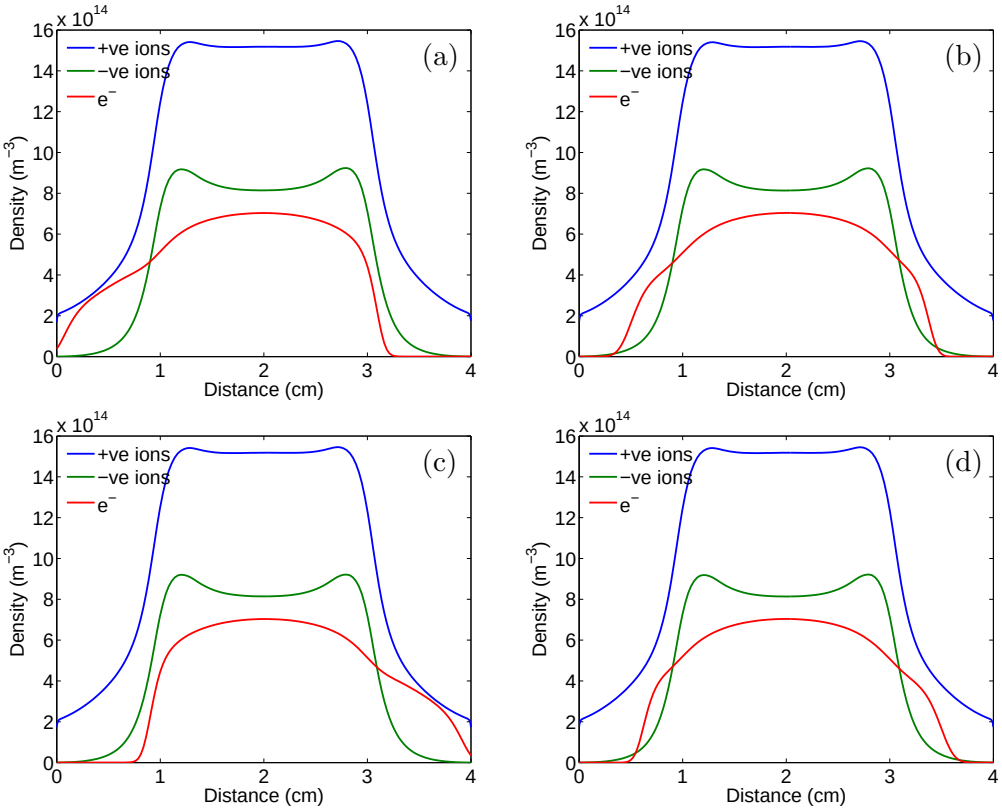

Figure 48: Charged species densities at relative phases in the RF cycle of (a) 0, (b) $\pi/2$, (c) π, and (d) $3\pi/2$.

there is deposition across the plasma bulk, it is highest on the bulk side of the expanding sheath, as the encroaching electric field interacts with the electrons flowing toward the walls. When the sheath collapses, it can be seen to actually remove energy from the electrons, though this effect is small when compared to the total net ohmic power. This localisation in time and space is expected to have an impact on the electron temperature, and indeed this is the case.

Figure 50 shows how the electron temperature is modulated in both space and time. In figure 50(a) the full range of temperature is resolved, and the extreme values inside the sheath are shown. As the electron density within the sheath is negligible (see figure 47), it is the region of high temperature close to the sheath, but still within the bulk, where the highest rate of ionisation occurs. This can be seen more clearly in figure 50(b).

It can also be seen in figure 50(b) that the electron temperature varies by a moderate amount across the whole discharge. Even across the centre of the plasma ($x = 2\,\mathrm{cm}$), there is modulation of $\pm 10\,\%$ in this example. As would be expected from the data given in figure 22(a), this has an impact on the net particle gains and losses.

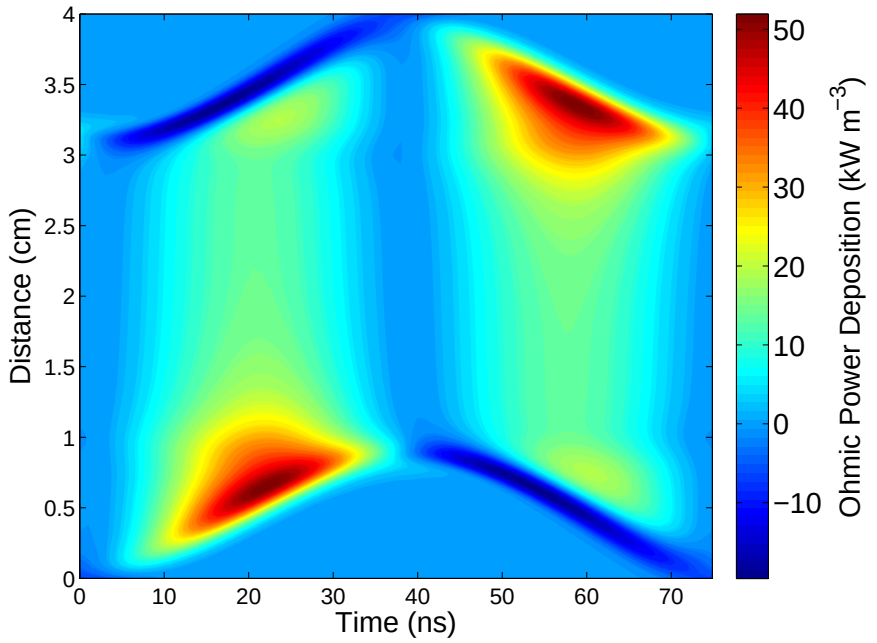

Figure 49: Time and space dependence of the ohmic power deposition as reported by the full fluid model.

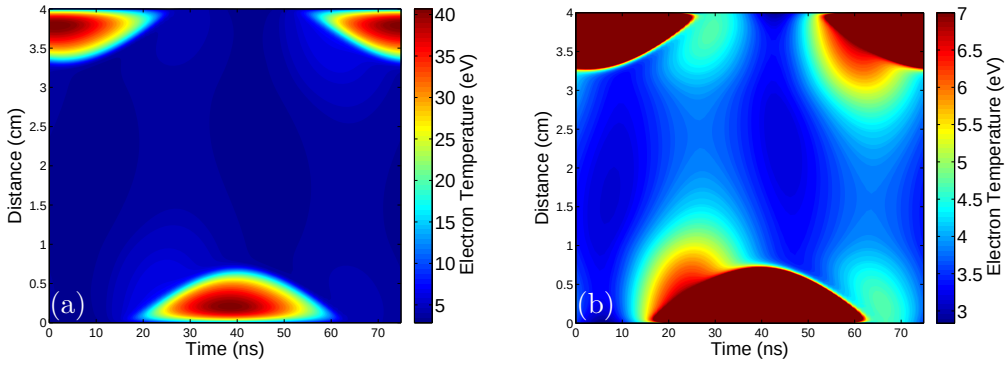

Figure 50: Electron temperature as a function of space and time. Both figures show the same data, but (b) restricts the colour scale to resolve behaviour in the bulk.

Acronyms

BVP	boundary value problem
CCP	capacitively coupled plasma
EEDF	electron energy distribution function
IVP	initial value problem
PECE	Predict-Evaluate-Correct-Evaluate
PIC	particle-in-cell
PROES	phase resolved optical emission spectroscopy
RF	radio frequency
RHS	right hand side
RRC	reaction rate coefficient

Symbols and Constants

Symbol	Name	Description
D_α	Diffusion Coefficient	Coefficient describing the thermal drift motion of species α.
$\boldsymbol{E}$	Electric Field	Electric Field measured in $\mathrm{V\,m^{-1}}$.
ζ	Normalised Electric Field	Normalised electric field, equal to $eu_B\boldsymbol{E}/(n_f K_0 k_B T_{e0})$.
e	Elementary charge	Electrostatic charge of a single proton. $1.602\,177 \times 10^{-19}\,\mathrm{C}$.
ε	Mean Electron Energy	The mean electron energy measured Joules.
ϵ_R	Normalised Reaction Rate Coefficient	Normalised energy dependent rate coefficient for reaction R.
$\epsilon_{\alpha\beta}$	Normalised Elastic Collision Rate Coefficient	Normalised energy dependent rate coefficient for elastic collisions between species α and β.
ε_0	Permittivity of free space	Absolute dielectric permittivity of a classical vacuum. Equal to $8.854\,188 \times 10^{-12}\,\mathrm{F\,m^{-1}}$
$\mathcal{E}_{th,R}$	Reaction Threshold Energy	Threshold energy of reaction R measured in Joules.
$\boldsymbol{F}_\varepsilon$	Electron Energy Flux	A measure of the total energy flux due to electron motion.
Γ_α	Normalised Particle Flux	Normalised flux of particles of type α, equal to $N_\alpha V_\alpha$.
g_α	Elastic Collision Frequency Gradient Coefficient	A temperature dependent coefficient describing the relative change in collision frequency over a temperature gradient of species α.

G_{R_α}	Particle Gain Coefficient	The number of particles of type α gained through reaction R. Particle loss has a negative coefficient.
$\boldsymbol{j}$	Current Density	Current density measured in $\mathrm{A\,m^{-2}}$.
$\boldsymbol{j}_0$	Current Density Amplitude	Amplitude of sinusoidal current density measured in $\mathrm{A\,m^{-2}}$.
J_0^2	Normalised Squared Current Density Amplitude	Normalised representation of the squared current density amplitude, equal to $j_0^2 m_e/(2e^2 n_f^2 k_B T_{e0})$.
K_0	Normalisation Reaction Rate Coefficient	Reaction rate coefficient to which others are normalised.
k_B	Boltzmann constant	Relationship between particle energy and macroscopic temperature for an ideal gas. Equal to $1.380\,649 \times 10^{-23}\,\mathrm{J\,K^{-1}}$
K_R	Reaction Rate Coefficient	Energy dependent rate coefficient for reaction R, measured in $\mathrm{s^{-1}\,m^{-3}}$.
$K_{\alpha\beta}$	Elastic Collision Rate Coefficient	Energy dependent rate coefficient for elastic collisions between species α and β, measured in $\mathrm{s^{-1}\,m^{-3}}$.
L_α	Logarithmic Normalised Particle Density	Logarithm of normalised particle density, equal to $\ln N_\alpha$.
λ_D	Debye length	Length scale for the range of electrostatic effects in a plasma. Equal to $\left(\frac{\varepsilon_0 k_B T_e}{n_e e^2}\right)^{\frac{1}{2}}$
M_α	Normalised Particle Mass	Normalised mass of particles of type α, equal to m_α/m_i.
m_α	Mass	Mass of a single particle of species α, given in kg.
μ_α	Mobility	Coefficient describing the drift motion of a charged species α within an electric field.
N_α	Normalised Particle Density	Normalised density of particles of type α, equal to n_α/n_f.
n_α	Particle Density	Volumetric density of species α, given in $\mathrm{m^{-3}}$.

n_f	Gas Fill Density	The density of feed gas that exists before a plasma is present, given in m^{-3}, and calculated from $p = nk_BT$.
ω	Driving Frequency	The frequency of the driving voltage/current in an RF plasma, in radians per second.
ϕ	Potential	Electrostatic potential in Volts.
$\bar{P}_{ohm}$	Mean Volumetric Ohmic Power Deposition	Volumetric rate of power deposition into the plasma from ohmic sources, measured in $\mathrm{W\,m}^{-3}$.
$\boldsymbol{q}_\alpha$	Heat Flux	Heat flux of species α measured in $\mathrm{W\,m}^{-2}$.
Q_α	Normalised Particle Heat Flux	Normalised heat flux of particles of type α, equal to $\boldsymbol{q}_\alpha/(n_f u_B k_B T_{e0})$.
σ_{DC}	Plasma DC Conductivity	Conductivity of plasma in the low frequency limit, measured in $\Omega^{-1}\,\mathrm{m}^{-1}$.
Σ_α	Normalised Volumetric Power Density	Normalised volumetric rate of power deposition, equal to $P_\alpha/(n_f^2 K_0 k_B T_{e0})$.
T_α	Temperature	Thermodynamic temperature of species α measured in Kelvin (K).
T_α^e	Temperature	Thermodynamic temperature of species α, measured in eV.
u_B	Bohm Velocity	The minimum required flow velocity of positive ions at the bulk to sheath boundary, given in $\mathrm{m\,s}^{-1}$.
V_α	Normalised Particle Velocity	Normalised velocity of particles of type α, equal to $\boldsymbol{u}_\alpha/u_B$.
$\boldsymbol{v}_\alpha$	Particle Velocity	Velocity of a single particle of species α, given in $\mathrm{m\,s}^{-1}$.
$\boldsymbol{u}_\alpha$	Flow Velocity	Collective velocity of species α, given in $\mathrm{m\,s}^{-1}$.
$\boldsymbol{w}_\alpha$	Thermal Velocity	Randomised velocity of a single particle of species α, given in $\mathrm{m\,s}^{-1}$, related to the pressure of species α.
v_{th}	Mean Thermal Velocity	Mean thermal velocity of species α, equal to $(8k_BT_s/\pi m_s)^{0.5}$.

ν_R	Reaction Rate	Energy dependent rate for reaction R, measured in s^{-1}.
$\nu_{\alpha\beta}$	Elastic Collision Rate	Energy dependent rate of elastic collisions between species α and β, measured in s^{-1}.
$\hat{\boldsymbol{x}}$	Surface Normal	The unit vector perpendicular to the surface at which it is defined, equal to ± 1 in a one dimensional system.
Z_α	Particle Charge	Electric charge on particles of typ α, in numbers of elementary charges.

References

[1] S. H. Lee, F. Iza, and J. K. Lee. Particle-in-cell Monte Carlo and fluid simulations of argon-oxygen plasma: Comparisons with experiments and validations. *Physics of Plasmas*, 13(5):057102, 2006.

[2] J. Waskoenig, K. Niemi, N. Knake, L. M. Graham, S. Reuter, V. Schulz-von der Gathen, and T. Gans. Atomic oxygen formation in a radio-frequency driven micro-atmospheric pressure plasma jet. *Plasma Sources Science and Technology*, 19(4):045018, 2010.

[3] E. Kawamura, A. J. Lichtenberg, and M. A. Lieberman. Electronegative plasma equilibria with spatially varying ionization. *Journal of Physics D: Applied Physics*, 45(49):495201, 2012.

[4] N. Nakano and T. Makabe. Influence of driving frequency on narrow-gap reactive-ion etching in SF_6. *Journal of Physics D: Applied Physics*, 28(1):31–39, 1995.

[5] S. Kim, M. A. Lieberman, A. J. Lichtenberg, and J. T. Gudmundsson. Improved volume-averaged model for steady and pulsed-power electronegative discharges. *Journal of Vacuum Science & Technology A*, 24(6):2025, 2006.

[6] P. Chabert, A. J. Lichtenberg, M. A. Lieberman, and A. M. Marakhtanov. Instabilities in low-pressure electronegative inductive discharges. *Plasma Sources Science and Technology*, 10(3):478–489, 2001.

[7] J. T. Gudmundsson. Recombination and detachment in oxygen discharges: the role of metastable oxygen molecules. *Journal of Physics D: Applied Physics*, 37 (15):2073–2081, 2004.

[8] C. Lee and M. A. Lieberman. Global model of Ar, O_2, Cl_2, and Ar/O_2 high-density plasma discharges. *Journal of Vacuum Science & Technology A*, 13(2): 368, 1995.

[9] T. Murakami, K. Niemi, T. Gans, D. O'Connell, and W. G. Graham. Chemical kinetics and reactive species in atmospheric pressure helium-oxygen plasmas with humid-air impurities. *Plasma Sources Science and Technology*, 22(1):015003, 2013.

[10] S. Kim. *An Improved Global Model for Electronegative Discharge and Ignition Conditions for Peripheral Plasma Connected to a Capacitive Discharge*. PhD thesis, EECS Department, University of California, Berkeley, 2006.

[11] T. Murakami, K. Niemi, T. Gans, D. O'Connell, and W. G. Graham. Interacting kinetics of neutral and ionic species in an atmospheric-pressure helium–oxygen plasma with humid air impurities. *Plasma Sources Science and Technology*, 22 (4):045010, 2013.

[12] T. Murakami, K. Niemi, T. Gans, D. O'Connell, and W. G. Graham. Afterglow chemistry of atmospheric-pressure helium–oxygen plasmas with humid air impurity. *Plasma Sources Science and Technology*, 23(2):025005, 2014.

[13] A. Greb, K. Niemi, D. O'Connell, G. J. Ennis, N. MacGearailt, and T. Gans. Improved fluid simulations of radio-frequency plasmas using energy dependent ion mobilities. *Physics of Plasmas*, 20(5):053502, 2013.

[14] L. Liard, A. Aanesland, and P. Chabert. Dynamics of neutral gas depletion investigated by time- and space-resolved measurements of xenon atom ground state density. *Journal of Physics D: Applied Physics*, 45(23):235201, 2012.

[15] A. Fruchtman. Nonmonotonic plasma density profile due to neutral-gas depletion. *Physics of Plasmas*, 17(2):023502, 2010.

[16] D. O'Connell, T. Gans, D. L. Crintea, U. Czarnetzki, and N. Sadeghi. Neutral gas depletion mechanisms in dense low-temperature argon plasmas. *Journal of Physics D: Applied Physics*, 41(3):035208, 2008.

[17] M. Shimada, G. R. Tynan, and R. Cattolica. Neutral gas density depletion due to neutral gas heating and pressure balance in an inductively coupled plasma. *Plasma Sources Science and Technology*, 16(1):193–199, 2007.

[18] M. D. Kilgore, H. M. Wu, and D. B. Graves. Neutral transport in high plasma-density reactors. *Journal of Vacuum Science & Technology B*, 12(1):494, 1994.

[19] M. A. Lieberman and A. J. Lichtenberg. *Principles of Plasma Discharges and Materials Processing*. Wiley, 1994.

[20] P. Chabert and N. St. J. Braithwaite. *Physics of Radio-Frequency Plasmas*. Cambridge University Press, 2011.

[21] T. J. M. Boyd and J. J. Sanderson. *The Physics of Plasmas*. Cambridge University Press, 2003.

[22] R. O. Dendy. *Plasma Dynamics*. Clarendon Press, 1990.

[23] J. A. Bittencourt. *Fundamentals of Plasma Physics*. Pergamon Press, 1986.

[24] T. Lafleur and P. Chabert. Is collisionless heating in capacitively coupled plasmas really collisionless? *Plasma Sources Science and Technology*, 24(4):044002, 2015.

[25] S. Sharma, S. K. Mishra, P. K. Kaw, A. Das, N. Sirse, and M. M. Turner. Collisionless sheath heating in current-driven capacitively coupled plasma discharges via higher order sinusoidal signals. *Plasma Sources Science and Technology*, 24 (2):025037, 2015.

[26] T. Lafleur, P. Chabert, M. M. Turner, and J.-P. Booth. Equivalence of the hard-wall and kinetic-fluid models of collisionless electron heating in capacitively coupled discharges. *Plasma Sources Science and Technology*, 23(1):015016, 2014.

[27] E. Kawamura, M. A. Lieberman, and A. J. Lichtenberg. Electron heating in low pressure capacitive discharges revisited. *Physics of Plasmas*, 21(12):123505, 2014.

[28] K.-U. Riemann. The validity of Bohm's sheath criterion in rf discharges. *Physics of Fluids B*, 4(9):2693–2695, 1992.

[29] N. St. J. Braithwaite and J. E. Allen. Boundaries and probes in electronegative plasmas. *Journal of Physics D: Applied Physics*, 21(12):1733–1737, 1988.

[30] F. Paschen. Ueber die zum funkenübergang in luft, wasserstoff und kohlensäure bei verschiedenen drucken erforderliche potentialdifferenz. *Annalen der Physik*, 273(5):69–96, 1889. [in German].

[31] J. Park, I. Henins, H. W. Herrmann, and G. S. Selwyn. Gas breakdown in an atmospheric pressure radio-frequency capacitive plasma source. *Journal of Applied Physics*, 89(1):15, 2001.

[32] L. Ledernez, F. Olcaytug, and G. Urban. Paschen curve and film growth in low pressure capacitively coupled magnetron plasma polymerization. *Contributions to Plasma Physics*, 52(4):283–288, 2012.

[33] Z. Lj. Petrović, N. Škoro, D. Marić, C. M. O. Mahony, P. D. Maguire, M. Radmilović-Radnović, and G. Malović. Breakdown, scaling and volt–ampere characteristics of low current micro-discharges. *Journal of Physics D: Applied Physics*, 41(19):194002, 2008.

[34] J. T. Gudmundsson, E. Kawamura, and M. A. Lieberman. A benchmark study of a capacitively coupled oxygen discharge of the oopd1 particle-in-cell Monte Carlo code. *Plasma Sources Science and Technology*, 22(3):035011, 2013.

[35] K. Matyash, R. Schneider, F. Taccogna, A. Hatayama, S. Longo, M. Capitelli, D. Tskhakaya, and F. X. Bronold. Particle in cell simulation of low temperature laboratory plasmas. *Contributions to Plasma Physics*, 47(8-9):595–634, 2007.

[36] K. Bera, S. Rauf, and K. Collins. PIC-MCC/Fluid hybrid model for low pressure capacitively coupled O_2 plasma. *AIP Conference Proceedings*, 1333(1):1027–1032, 2011.

[37] I. G. Kouznetsov, A. J. Lichtenberg, and M. A. Lieberman. Modelling electronegative discharges at low pressure. *Plasma Sources Science and Technology*, 5(4): 662, 1996.

[38] M. M. Turner, A. Derzsi, Z. Donkó, D. Eremin, S. J. Kelly, T. Lafleur, and T. Mussenbrock. Simulation benchmarks for low-pressure plasmas: Capacitive discharges. *Physics of Plasmas*, 20(1):013507, 2013.

[39] J. S. Townsend and V. A. Bailey. The motion of electrons in argon and in hydrogen. *Philosophical Magazine*, S.6, 46:1033–1052, 1922.

[40] D.-L. Zeng, X. Gao, X.-Y. Han, and J.-M. Li. Precision calculation of low-energy electron-impact excitation cross sections of helium among the ground and excited states. *Physical Review A*, 91(2):022707, 2015.

[41] D. C. Griffin, D. M. Mitnik, J. Colgan, and M. S. Pindzola. Electron-impact excitation of lithium. *Physical Review A*, 64(3):032718, 2001.

[42] W. Van Gaens and A. Bogaerts. Reaction pathways of biomedically active species in an ar plasma jet. *Plasma Sources Science and Technology*, 23(3):035015, 2014.

[43] M. M. Turner. Uncertainty and error in complex plasma chemistry models. *Plasma Sources Science and Technology*, 24(3):035027, 2015.

[44] C. Riccardi, R. Barni, and M. Fontanesi. Experimental study and simulations of electronegative discharges at low pressure. *Journal of Applied Physics*, 90(8): 3735, 2001.

[45] D. C. Seo, T. H. Chung, H. J. Yoon, and G. H. Kim. Electrostatic probe diagnostics of a planar-type radio-frequency inductively coupled oxygen plasma. *Journal of Applied Physics*, 89(8):4218, 2001.

[46] T. Holstein. Energy distribution of electrons in high frequency gas discharges. *Physical Review*, 70(5-6):367–384, 1946.

[47] G. J. M. Hagelaar and L. C. Pitchford. Solving the Boltzmann equation to obtain electron transport coefficients and rate coefficients for fluid models. *Plasma Sources Science and Technology*, 14(4):722–733, 2005.

[48] J. T. Gudmundsson. Global model of plasma chemistry in a low-pressure O_2/F_2 discharge. *Journal of Physics D: Applied Physics*, 35(4):328–341, 2002.

[49] C. S. Corr, S. Gomez, and W. G. Graham. Discharge kinetics of inductively coupled oxygen plasmas: experiment and model. *Plasma Sources Science and Technology*, 21(5):055024, 2012.

[50] T. Kimura, A. J. Lichtenberg, and M. A. Lieberman. Modelling finite cylinder electronegative discharges. *Plasma Sources Science and Technology*, 10(3):430, 2001.

[51] R. N. Franklin. The role of O_2 ($a^1\Delta_g$) metastables and associative detachment in discharges in oxygen. *Journal of Physics D: Applied Physics*, 34(12):1834–1839, 2001.

[52] V. E. Golant, A. P. Zhilinsky, and I. E. Sakharov. *Fundamentals of Plasma Physics*. Wiley, 1980.

[53] J. D. Lambert. *Computational Methods in Ordinary Differential Equations*. Wiley, 1973.

[54] E. Hairer, S. P. Nørsett, and G. Wanner. *Solving Ordinary Differential Equations I: Nonstiff Problems*. Springer Science & Business Media, 2000.

[55] R. Ashino, M. Nagase, and R. Vaillancourt. Behind and beyond the matlab ODE suite. *Computers & Mathematics with Applications*, 40(4-5):491–512, 2000.

[56] W. H. Schottky. Diffusionstheorie der positiven Säule. *Physikalische Zeitschrift*, 25:635–640, 1924. [in German].

[57] P. M. Morse. A theory of the electric discharge through gases. *Physical Review*, 31(6):1003–1017, 1928.

[58] L. Tonks and I. Langmuir. A general theory of the plasma of an arc. *Physical Review*, 34(6):876–922, 1929.

[59] R. Holm. Bemerkungen zur Theorie der positiven Säule in zweiatomigen Gasen. *Zeitschrift für Physik*, 75(3):171–190, 1932. [in German].

[60] R. Seeliger. Die diffusionstheorie der positiven säule in elektronegativen gasen. *Annalen der Physik*, 441(1):93–96, 1950. [in German].

[61] J. Wilhelm. Zur Anwendung der Schottkyschen Diffusionstheorie auf Entladungen mit mehreren ionenarten und angeregten Neutralteilchen. *Zeitschrift für Physik*, 154(3):361–375, 1959. [in German].

[62] J. B. Thompson. Negative ions in the positive column of the oxygen discharge. *Proceedings of the Physical Society*, 73(5):818–821, 1959.

[63] S. A. Self. Static theory of a discharge column at intermediate pressures. *Physics of Fluids*, 9(12):2486, 1966.

[64] J. R. Forrest and R. N. Franklin. The theory of the positive column including space-charge effects. *Journal of Physics D: Applied Physics*, 1(10):1357, 1968.

[65] D. B. Ilić. Theory of a steady-state nonisothermal positive column in a magnetic field. *Journal of Applied Physics*, 44(9):3993, 1973.

[66] P. D. Edgley and A. von Engel. Theory of positive columns in electronegative gases. *Proceedings of the Royal Society A: Mathematical, Physical and Engineering Sciences*, 370(1742):375–387, 1980.

[67] R. N. Franklin and J. Snell. Modelling discharges in electronegative gases. *Journal of Physics D: Applied Physics*, 32(17):2190–2203, 1999.

[68] A. J. Lichtenberg, M. A. Lieberman, I. G. Kouznetsov, and T. H. Chung. Transitions and scaling laws for electronegative discharge models. *Plasma Sources Science and Technology*, 9(1):45–56, 2000.

[69] R. N. Franklin. A comprehensive treatment of the positive column of discharges in electronegative gases. *Proceedings of the Royal Society A: Mathematical, Physical and Engineering Sciences*, 457(2006):307–330, 2001.

[70] G. G. Arutunyan, G. A. Galechyan, and L. B. Tavakalyan. On electron concentration distribution along the radius of the positive column of a glow discharge in electronegative gases. *Beiträge aus der Plasmaphysik*, 23(3):271–277, 1983. [in Russian].

[71] D. B. Ogle and G. A. Woolsey. Diffuse and constricted glow discharges in SF_6. *Journal of Physics D: Applied Physics*, 20(4):453—461, 1987.

[72] C. M. Ferreira, G. Gousset, and M. Touzeau. Quasi-neutral theory of positive columns in electronegative gases. *Journal of Physics D: Applied Physics*, 21(9): 1403–1413, 1988.

[73] P. G. Daniels and R. N. Franklin. The positive column in electronegative gases-a boundary layer approach. *Journal of Physics D: Applied Physics*, 22(6):780–85, 1989.

[74] P. G. Daniels, R. N. Franklin, and J. Snell. The contracted positive column in electronegative gases. *Journal of Physics D: Applied Physics*, 23(7):823–831, 1990.

[75] R. N. Franklin and J. Snell. The free fall column with negative ions. *Journal of Physics D: Applied Physics*, 25(3):453–457, 1992.

[76] R. N. Franklin, P. G. Daniels, and J. Snell. Characteristics of electric discharges in the halogens: the recombination-dominated positive column. *Journal of Physics D: Applied Physics*, 26(10):1638–1649, 1993.

[77] G. Gousset, M. Touzeau, M. Vialle, and C. M. Ferreira. Kinetic model of a DC oxygen glow discharge. *Plasma Chemistry and Plasma Processing*, 9(2):189–206, 1989.

[78] V. N. Volynets, A. V. Lukyanova, A. T. Rakhimov, D. I. Slovetsky, and N. V. Suetin. Experimental and theoretical study of the cf 4 DC glow discharge positive column. *Journal of Physics D: Applied Physics*, 26(4):647–656, 1993.

[79] D. Vender, W. W. Stoffels, E. Stoffels, G. M. W. Kroesen, and F. J. de Hoog. Charged-species profiles in electronegative radio-frequency plasmas. *Physical Review E*, 51(3):2436–2444, 1995.

[80] F. Grangeon, C. Monard, J.-L. Dorier, A. A. Howling, C. Hollenstein, D. Romanini, and N. Sadeghi. Applications of the cavity ring-down technique to a large-area RF-plasma reactor. *Plasma Sources Science and Technology*, 8:448–456, 1999.

[81] H. M. Katsch, A. Tewes, E. Quandt, A. Goehlich, T. Kawetzki, and H. F. Döbele. Detection of atomic oxygen: Improvement of actinometry and comparison with laser spectroscopy. *Journal of Applied Physics*, 88(11):6232, 2000.

[82] V. Vahedi and M. Surendra. A Monte Carlo collision model for the particle-in-cell method: applications to argon and oxygen discharges. *Computer Physics Communications*, 87(12):179–198, 1995. Particle Simulation Methods.

[83] H.-M. Wu, D. B. Graves, and M. Kilgore. Two-dimensional simulation of compact ECR plasma sources. *Plasma Sources Science and Technology*, 6(2):231–239, 1997.

[84] V. Midha and D. J. Economou. Dynamics of ion-ion plasmas under radio frequency bias. *Journal of Applied Physics*, 90(3):1102, 2001.

[85] C. Lee, D. B. Graves, M. A. Lieberman, and D. W. Hess. Global model of plasma chemistry in a high density oxygen discharge. *Journal of The Electrochemical Society*, 141(6):1546, 1994.

[86] E. Stoffels, W. W. Stoffels, D. Vender, M. Kando, G. M. W. Kroesen, and F. J. de Hoog. Negative ions in a radio-frequency oxygen plasma. *Physical Review E*, 51(3):2425–2435, 1995.

[87] A. J. Lichtenberg, V. Vahedi, M. A. Lieberman, and T. Rognlien. Modeling electronegative plasma discharges. *Journal of Applied Physics*, 75(5):2339, 1994.

[88] H. B. Valentini and F. Herrmann. Boundary value problems for multi-component plasmas and a generalized bohm criterion. *Journal of Physics D: Applied Physics*, 29(5):1175–1180, 1996.

[89] A. J. Lichtenberg, I. G. Kouznetsov, Y. T. Lee, M. A. Lieberman, I. D. Kaganovich, and L. D. Tsendin. Modelling plasma discharges at high electronegativity. *Plasma Sources Science and Technology*, 6(3):437–449, 1997.

[90] R. N. Franklin and J. Snell. The low-pressure positive column in electronegative gases including space charge-matching plasma and sheath. *Journal of Physics D: Applied Physics*, 31(19):2532–2542, 1998.

[91] R. N. Franklin. Electronegative plasmas - why are they so different? *Plasma Sources Science and Technology*, 11(3A):A31–A37, 2002.

[92] M. Lampe, W. M. Manheimer, R. F. Fernsler, S. P. Slinker, and G. Joyce. The physical and mathematical basis of stratification in electronegative plasmas. *Plasma Sources Science and Technology*, 13(1):15–26, 2004.

[93] R. Moulick and K. S. Goswami. Formation of collisional sheath in electronegative plasma with two species of positive ions. *Physics of Plasmas*, 22(3):033510, 2015.

[94] P. Chabert. An expression for the h l factor in low-pressure electronegative plasma discharges. *Plasma Sources Science and Technology*, 25(2):025010, 2016.

[95] Q. Wang, D. J. Economou, and V. M. Donnelly. Simulation of a direct current microplasma discharge in helium at atmospheric pressure. *Journal of Applied Physics*, 100(2):023301, 2006.

[96] D. P. Lymberopoulos and D. J. Economou. Fluid simulations of glow discharges: Effect of metastable atoms in argon. *Journal of Applied Physics*, 73(8):3668, 1993.

[97] R. S. Cunningham and C. J. Geankoplis. Diffusion in three-component gas mixtures in the transition region between Knudsen and molecular diffusion. *Industrial & Engineering Chemistry Fundamentals*, 7(3):429–432, 1968.

[98] H.-B. Valentini. Removal of singularities in the hydrodynamic description of plasmas including space-charge effects, several species of ions and non-vanishing ion temperature. *Journal of Physics D: Applied Physics*, 21(2):311–321, 1988.

[99] L. L. Alves. Fluid modelling of the positive column of direct-current glow discharges. *Plasma Sources Science and Technology*, 16(3):557–569, 2007.

[100] A. Kono, M. Endo, K. Ohata, S. Kishimoto, and T. Goto. Charged particle densities and kinetics in a radio-frequency SF_6 plasma. *Journal of Applied Physics*, 76(11):7221–7230, 1994.

[101] G. L. Rogoff. Ambipolar diffusion coefficients for discharges in attaching gases. *Journal of Physics D: Applied Physics*, 18(8):1533, 1985.

[102] T. Kimura, K. Kaga, and K. Ohe. Gap length dependence of electron energy distribution in low-pressure Ar capacitively coupled RF discharges. *Japanese Journal of Applied Physics*, 39(3R):1351, 2000.

[103] L. Liard. *Transport non linéaire dans un réacteur hélicon.* PhD thesis, Ecole Polytechnique, 2009.

[104] J.-L. Raimbault, L. Liard, J.-M. Rax, P. Chabert, A. Fruchtman, and G. Makrinich. Steady-state isothermal bounded plasma with neutral dynamics. *Physics of Plasmas*, 14(1):013503, 2007.

[105] M. J. Kushner. Plasma modelling techniques. In *Summer School on Fundamentals of Low Pressure and High Pessure Plasmas, 21st International Symposium on Plasma Chemistry, Cairns, Australia*, 2013.

[106] C. Courteille, A. M. Bruneteau, and M. Bacal. Investigation of a large volume negative hydrogen ion source. *Review of Scientific Instruments*, 66(3):2533, 1995.

[107] P. Bruggeman, F. Iza, D. Lauwers, and Y. A. Gonzalvo. Mass spectrometry study of positive and negative ions in a capacitively coupled atmospheric pressure RF excited glow discharge in He–water mixtures. *Journal of Physics D: Applied Physics*, 43(1):012003, 2009.

[108] P. Chabert and T. E. Sheridan. Kinetic model for a low-pressure discharge with negative ions. *Journal of Physics D: Applied Physics*, 33(15):1854–1860, 2000.

[109] R. N. Franklin. The plasma-wall boundary region in negative-ion-dominated plasmas at low pressures. *Plasma Sources Science and Technology*, 9(2):191–198, 2000.

[110] M. A. Lieberman, A. J. Lichtenberg, and A. M. Marakhtanov. Instabilities in low-pressure inductive discharges with attaching gases. *Applied Physics Letters*, 75(23):3617, 1999.

[111] S. Takayanagi, T. Yanagitani, and M. Matsukawa. Unusual growth of polycrystalline oxide film induced by negative ion bombardment in the capacitively coupled plasma deposition. *Applied Physics Letters*, 101(23):232902, 2012.

[112] A. A. Bol'shakov, B. A. Cruden, R. Mogul, M. V. V. S. Rao, S. P. Shama, B. N. Khare, and M. Meyyappan. Radio-frequency oxygen plasma as a sterilization source. *AIAA Journal*, 42(4):823–832, 2004.

[113] D. A. Carl, D. W. Hess, M. A. Lieberman, T. D. Nguyen, and R. Gronsky. Effects of dc bias on the kinetics and electrical properties of silicon dioxide grown in an electron cyclotron resonance plasma. *Journal of Applied Physics*, 70(6):3301, 1991.

[114] A. Vesel and M. Mozetic. Surface modification and ageing of PMMA polymer by oxygen plasma treatment. *Vacuum*, 86(6):634–637, 2012.

[115] J. T. Gudmundsson and M. A. Lieberman. On the role of metastables in capacitively coupled oxygen discharges. *Plasma Sources Science and Technology*, 24 (3):035016, 2015.

[116] A. Greb, K. Niemi, D. O'Connell, and T. Gans. The influence of surface properties on the plasma dynamics in radio-frequency driven oxygen plasmas: Measurements and simulations. *Applied Physics Letters*, 103(24):244101, 2013.

[117] D. S. Stafford and M. J. Kushner. $O_2(^1\Delta)$ production in He/O_2 mixtures in flowing low pressure plasmas. *Journal of Applied Physics*, 96(5):2451, 2004.

[118] B. F. Gordiets, C. M. Ferreira, V. L. Guerra, J. M. A. H. Loureiro, J. Nahorny, D. Pagnon, M. Touzeau, and M. Vialle. Kinetic model of a low-pressure N_2-O_2 flowing glow discharge. *IEEE Transactions on Plasma Sciences*, 23(4):750–768, 1995.

[119] S. A. Lawton and A. V. Phelps. Excitation of the $b^1\Sigma_g^+$ state of O_2 by low energy electrons. *The Journal of Chemical Physics*, 69(3):1055–1068, 1978.

[120] F. X. Bronold, K. Matyash, D. Tskhakaya, R. Schneider, and H. Fehske. Radio-frequency discharges in oxygen: I. Particle-based modelling. *Journal of Physics D: Applied Physics*, 40(21):6583–6592, 2007.

[121] P. D. Burrow. Dissociative attachment from the O_2 ($a^1\Delta_g$) state. *Journal of Chemical Physics*, 59(9):4922, 1973.

[122] Z. L. Petrović, Z. M. Raspopović, V. D. Stojanović, J. V. Jovanović, G. Malović, T. Makabe, and J. de Urquijo. Data and modeling of negative ion transport in gases of interest for production of integrated circuits and nanotechnologies. *Applied Surface Science*, 253(16):6619–6640, 2007.

[123] MATLAB 7.14 (R2012a). The MathWorks, Inc., Natick, Massachusetts, United States, 2012.

[124] L. F. Shampine and M. K. Gordon. *Computer Solution of Ordinary Differential Equations: the Initial Value Problem*. W H Freeman, San Francisco, 1975.

[125] J. Meichsner, K. Dittmann, and C. Küllig. Electron and negative ion analysis in oxygen capacitively coupled radio frequency plasma. *Contributions to Plasma Physics*, 52(7):561–570, 2012.

[126] H. Amemiya, N. Yasuda, and M. Endou. Negative ion-containing plasma in parallel-plate radio-frequency discharge in oxygen. *Plasma Chemistry and Plasma Processing*, 14(3):209–227, 1994.

[127] S. V. Berezhnoj, C. B. Shin, U. Buddemeier, and I. Kaganovich. Charged species profiles in oxygen plasma. *Applied Physics Letters*, 77(6):800, 2000.

[128] C. Küllig, K. Dittmann, and J. Meichsner. A novel approach for negative ion analysis using 160 GHz microwave interferometry and laser photodetachment in oxygen cc-rf plasmas. *Plasma Sources Science and Technology*, 19(6):065011, 2010.

[129] J. T. Gudmundsson and B. Ventéjou. The pressure dependence of the discharge properties in a capacitively coupled oxygen discharge. *Journal of Applied Physics*, 118(15):153302, 2015.

[130] V. A. Lisovskiy and V. D. Yegorenkov. Double layer onset inside the near-electrode sheath of a RF capacitive discharge in oxygen. *Vacuum*, 80(5):458–467, 2006.

[131] C. Küllig, T. Wegner, and J. Meichsner. Spatially resolved langmuir probe diagnostics in a capacitively coupled radio frequency argon and oxygen plasma. *Plasma Sources Science and Technology*, 24(1):015027, 2015.

[132] K. Dittmann, C. Küllig, and J. Meichsner. Electron and negative ion dynamics in electronegative CC-RF plasmas. *Plasma Physics and Controlled Fusion*, 54 (12):124038, 2012.

[133] S. D. Baalrud, B. Scheiner, B. Yee, M. Hopkins, and E. Barnat. Extensions and applications of the Bohm criterion. *Plasma Physics and Controlled Fusion*, 57 (4):044003, 2015.

[134] M. M. Hatami. Nonextensive statistics and the sheath criterion in collisional plasmas. *Physics of Plasmas*, 22(1):013508, 2015.

[135] L. Kos, D. D. Tskhakaya, Sr., and N. Jelić. Unified Bohm criterion. *Physics of Plasmas*, 22(9):093503, 2015.

[136] R. Morales Crespo and R. N. Franklin. Examining the range of validity of the Bohm criterion. *Journal of Plasma Physics*, 80(03):495–511, 2014.

[137] H.-B. Valentini and D. Kaiser. The limits of the Bohm criterion in collisional plasmas. *Physics of Plasmas*, 22(5):053512, 2015.

[138] H. Amemiya. Sheath formation criterion and ion flux for a non-maxwellian plasma containing negative ions. *Journal of the Physical Society of Japan*, 67 (6):1955–1962, 1998.

[139] C. Küllig, Th. Wegner, and J. Meichsner. Instabilities in a capacitively coupled oxygen plasma. *Physics of Plasmas*, 22(4):043515, 2015.

[140] A. Greb, A. R. Gibson, K. Niemi, D. O'Connell, and T. Gans. Influence of surface conditions on plasma dynamics and electron heating in a radio-frequency driven capacitively coupled oxygen plasma. *Plasma Sources Science and Technology*, 24 (4):044003, 2015.

[141] A. Salabaş and R. P. Brinkmann. Non-neutral/quasi-neutral plasma edge definition for discharge models: A numerical example for dual frequency hydrogen capacitively coupled plasmas. *Japanese Journal of Applied Physics*, 45(6A):5203–5206, 2006.

[142] B. Bruneau, T. Gans, D. O'Connell, A. Greb, E. V. Johnson, and J.-P. Booth. Strong ionization asymmetry in a geometrically symmetric radio frequency capacitively coupled plasma induced by sawtooth voltage waveforms. *Physical Review Letters*, 114(12):125002, 2015.

[143] T. Lafleur, P. Chabert, and J.-P. Booth. Electron heating in capacitively coupled plasmas revisited. *Plasma Sources Science and Technology*, 23(3):035010, 2014.

[144] A. R. Gibson, A. Greb, W. G. Graham, and T. Gans. Tailoring the nonlinear frequency coupling between odd harmonics for the optimisation of charged particle dynamics in capacitively coupled oxygen plasmas. *Applied Physics Letters*, 106(5):054102, 2015.

[145] D. D. Monahan and M. M. Turner. Global models of electronegative discharges: critical evaluation and practical recommendations. *Plasma Sources Science and Technology*, 17(4):045003, 2008.

[146] T. E. Sheridan. Double layers in a modestly collisional electronegative discharge. *Journal of Physics D: Applied Physics*, 32(15):1761–1767, 1999.

[147] M. A. Lieberman. Analytical solution for capacitive RF sheath. *IEEE Transactions on Plasma Sciences*, 16(6):638–644, 1988.

[148] V. A. Godyak and N. Sternberg. Dynamic model of the electrode sheaths in symmetrically driven rf discharges. *Physical Review A*, 42(4):2299–2312, 1990.

[149] U. Czarnetzki. Analytical model for the radio-frequency sheath. *Physical Review E*, 88(6):063101, 2013.

[150] T. Nitschke and D. Graves. Matching an RF sheath model to a bulk plasma model. *IEEE Transactions on Plasma Science*, 23(4):717–727, 1995.

[151] A. M. Marakhtanov, M. Tuszewski, M. A. Lieberman, A. J. Lichtenberg, and P. Chabert. Stable and unstable behavior of inductively coupled electronegative discharges. *Journal of Vacuum Science & Technology A*, 21(6):1849, 2003.

[152] C. Küllig, K. Dittmann, T. Wegner, I. Sheykin, K. Matyash, D. Loffhagen, R. Schneider, and J. Meichsner. Dynamics and electronegativity of oxygen RF plasmas. *Contributions to Plasma Physics*, 52(10):836–846, 2012.

[153] D. Monahan. *Modelling the Electronegative Discharge*. PhD thesis, Dublin City University, 2007.

[154] J. T. Gudmundsson. On the effect of the electron energy distribution on the plasma parameters of an argon discharge: a global (volume-averaged) model study. *Plasma Sources Science and Technology*, 10(1):76–81, 2001.

[155] V. A. Godyak and V. N. Maksimov. The spatial distribution of a bounded plasma. *Moskovskii Universitet Vestnik Seriia Fizika Astronomiia*, 18:51–56, 1977.

[156] J. J. Munro and J. Tennyson. Global plasma simulations using dynamically generated chemical models. *Journal of Vacuum Science & Technology A*, 26(4): 865–869, 2008.

[157] G. R. Tynan. Neutral depletion and transport mechanisms in large-area high density plasma sources. *Journal of Applied Physics*, 86(10):5356, 1999.

[158] L. Liard, J.-L. Raimbault, J.-M. Rax, and P. Chabert. Plasma transport under neutral gas depletion conditions. *Journal of Physics D: Applied Physics*, 40(17): 5192–5195, 2007.

[159] E. W. Lemmon, M. O. McLinden, and D. G. Friend. *NIST Chemistry WebBook, NIST Standard Reference Database Number 69*. National Institute of Standards and Technology, 2015.

[160] R. J. Barlow. *Statistics: A Guide to the Use of Statistical Methods in the Physical Sciences*. John Wiley & Sons, 1989.

[161] L. Stafford, J. Margot, F. Vidal, M. Chaker, K. Giroux, J.-S. Poirier, A. Quintal-Léonard, and J. Saussac. Kinetics driving high-density chlorine plasmas. *Journal of Applied Physics*, 98(6):063301, 2005.

[162] S. Yun, K. Taylor, and G. R. Tynan. Measurement of radial neutral pressure and plasma density profiles in various plasma conditions in large-area high-density plasma sources. *Physics of Plasmas*, 7(8):3448, 2000.

[163] A. Aanesland, L. Liard, G. Leray, J. Jolly, and P. Chabert. Direct measurements of neutral density depletion by two-photon absorption laser-induced fluorescence spectroscopy. *Applied Physics Letters*, 91(12):121502, 2007.

[164] A. Fruchtman, G. Makrinich, P. Chabert, and J.-M. Rax. Enhanced plasma transport due to neutral depletion. *Physical Review Letters*, 95(11):115002, 2005.

[165] S. Nemschokmichal, K. Dittmann, and J. Meichsner. Spatial and phase-resolved optical emission patterns in capacitively coupled radio-frequency plasmas. *IEEE Transactions on Plasma Science*, 36(4):1360–1361, 2008.

[166] K. Dittmann, K. Matyash, S. Nemschokmichal, J. Meichsner, and R. Schneider. Excitation mechanisms and sheath dynamics in capacitively coupled radio-frequency oxygen plasmas. *Contributions to Plasma Physics*, 50(10):942–953, 2010.

[167] A. Greb. *Dynamics of the Plasma-Surface Interface in Capacitively Coupled Radio-Frequency Oxygen Plasmas: Coupling Numerical Simulations with Optical Diagnostics*. PhD thesis, University of York, 2013.

[168] P. J. Chantry. A simple formula for diffusion calculations involving wall reflection and low density. *Journal of Applied Physics*, 62(4):1141, 1987.

[169] R. L. Sharpless and T. G. Slanger. Surface chemistry of metastable oxygen. II. Destruction of $O_2(a\,^1\Delta_g)$. *Journal of Chemical Physics*, 91(12):7947, 1989.

[170] X. Yuan and L. L. Raja. Computational study of capacitively coupled high-pressure glow discharges in helium. *IEEE Transactions on Plasma Science*, 31 (4):495–503, 2003.